Direct and Indirect Effects of Alpha-Particle Irradiations of Human Prostate Tumor Cells

by

Rong Wang

B.S., Physics Engineering
B.S., Economics
Tsinghua University, Beijing, China 1999

SUBMITTED TO THE DEPARTMENT OF NUCLEAR SCIENCE & ENGINEERING AND THE HARVARD/MIT DIVISION OF HEALTH SCIENCES & TECHNOLOGY, RADIOLOGICAL SCIENCES JOINT PROGRAM ON AUGUST 24, 2005 IN PARTIAL FULFILLMENT OF THE REQUIREMENTS FOR THE DEGREE OF

DOCTOR OF PHILOSOPHY IN RADIOLOGICAL SCIENCES
AT THE
MASSACHUSETTS INSTITUTE OF TECHNOLOGY

SEPTEMBER 2005

Signature of Author: _____
Department of Nuclear Science and Engineering and the
Harvard/MIT Division of Health Sciences and Technology, Radiological Sciences Joint Program
August 22, 2005

Certified by: _____
Jeffrey A. Coderre
Associate Professor of Nuclear Science and Engineering
Thesis Supervisor

Certified by: _____
Jacquelyn C. Yanch
Professor of Nuclear Science and Engineering
Thesis Reader

Accepted by: _____
Jeffrey A. Coderre
Associate Professor of Nuclear Science and Engineering
Chair, Committee for Graduate Students

Direct and Indirect Effects of Alpha-Particle Irradiations of Human Prostate Tumor Cells

by

Rong Wang

Submitted to the Department of Nuclear Science and Engineering
and
the Harvard/MIT Division of Health Sciences and Technology, Radiological Sciences Joint Program
on August 22, 2005 in Partial Fulfillment of the
Requirements for the Degree of Doctor of Philosophy in
Radiological Sciences

ABSTRACT

The objective of this project is to establish a model system to study the direct effect, the bystander effect and the combinational effect of alpha-particle irradiations of human prostate tumor cells, toward the goal of improving the effectiveness of alpha-particle involved radiation therapies such as radioimmunotherapy and BNCT.

This project consists of an engineering part and a biological part. In the engineering part, an apparatus for alpha-particle irradiation of cells was designed and constructed. Dosimetry of this irradiator was conducted. The average dose rate to the cell monolayer in the specially designed Mylar dish was calculated to be 1.2 Gy/min. In the biological part, three *in vitro* studies were carried out with the DU-145 human prostate tumor cells using the established alpha-particle irradiator. Firstly, the direct effects of the alpha-particle irradiation of DU-145 cells were studied using the clonogenic assay, the comet assay and the micronucleus assay. A novel co-culture system was then designed to study the bystander effect transmitted through the cell culture medium. The micronucleus assay was used as endpoint for the bystander studies. A bystander effect was observed. Mechanism studies suggested that the nitric oxide was not involved in the process and indicated a short effective lifetime (< 1min) of the bystander signal. In the combinational studies, the effects of two anticancer drugs (Taxol and Oxaliplatin) together with direct alpha-particle irradiation were studied and no synergistic effect was observed for both drugs. Finally, the combined effect of the bystander effect and drug Taxol was studied, which was the first time that a combined effect between an anticancer drug and the radiation-induced bystander effect was studied.

The results of the model studies carried out in the two-dimensional monolayer of cells in this project can serve as a fundamental frame to be further applied to a three dimensional tumor micrometastasis model (spheroids) in the future. The understanding of the role the bystander effect plays in tumor cell killing, its mechanisms and its interaction with other agents, may make it possible to manipulate these factors to improve the effectiveness of alpha-particle involved therapies.

Thesis Supervisor: Jeffrey A. Coderre, Ph.D.
Associate Professor of Nuclear Science & Engineering, Massachusetts Institute of Technology

ACKNOWLEDGEMENTS

Five years passed very fast. I had great experience at MIT. When I look back, I feel so lucky and grateful for all the wonderful people I knew. They are treasure of my life.

First of all, I would like to say "thank you" to my dear parents. Although they are not physically here with me, their love is always companying me and gives me power. I love them and miss them.

I would like to thank my advisor Prof. Jeffrey Coderre for his kindness, consideration, guidance and support. He instructed me, inspired me, helped me, but never constrained me or forced me in my study and research. His trust always backed me up. He provided me great opportunities to explore my potential. Under his guidance, I grew a lot in all aspects. No word is enough to express my appreciation to him. He is more than an advisor to me- he is like a father as well as a friend.

I also give my greatest appreciation to my thesis reader Prof. Yanch. She is one of the most wonderful women I have ever met. Her kind support has been with me along the way. I truly admire her and take her as my live model.

My academic advisor Prof. Sow-Hsin Chen is very kind to me. He is a wonderful professor and constantly gave me good suggestions. I thank him for his tutoring and caring.

I thank Prof. Kathryn Held and Prof. John Essigmann for being in my thesis committee and instructing my research and thesis. Prof. Held provided me valuable suggestions in my research and made important comments on my thesis.

I would like to thank Hatsumi Nagasawa, Edouard I. Azzam and Roger. W. Howell for helping me to start my research and to develop the alpha-particle irradiator.

A special "thank you" goes to my husband and my former officemate Hongyu Jiang. He gives me enormous support in my research and my life. He is extremely knowledgeable, helpful and reliable. I miss so much the time working with him, weekdays and weekends. With a good research partner, working becomes enjoyable; with a good life partner, everyday is enjoyable.

My officemates and good friends Antonio Damato and Brad Schuller make the office like a home. I become a funnier and happier person since they moved in my office. They are smart, funny and helpful. I had wonderful time with them.

My colleague Mike Folkert is a very nice and helpful person. He has a wide range of knowledge. I regard him as a good teacher and information source.

Other people who deserve my thanks include Prof. Todreas, Dr. Richard Lanza, Dr. John Bernard, Rachel Batista, Jianmei Che, Clare Egan, Ron Smith, Cathy Modica, Domingo Altarejos, my HST buddy Lisa Treat, Dusadee, Xuping Zhu, Chunqi Li, Susan White, Ray and Yoonsun Chung. Their kindness, help and friendship made my journey easier and cheerful.

There are a lot of people not listed here deserve my appreciation. They are my friends outside my research group, outside my department or even outside MIT. They all contribute to my unforgettable experience in the past five years. Thank you all!

TABLE OF CONTENTS

LIST OF FIGURES

Chapter 2

Chapter 3

Chapter 4

Chapter 5

LIST OF TABLES

Chapter 1 Introduction

1.1 Background

1.1.1 Prostate cancer

Carcinoma of the prostate is the most common male cancer in Western countries. Approximately 230,000 new cases were diagnosed, and about 30,000 died of prostate cancer in 2004 in the United States (1).

The prostate is a walnut-sized gland located between the bladder and the penis and in front of the rectum. The primary function of the prostate is the production of seminal fluid. Prostate cancer occurs when cells within the prostate grow uncontrollably, creating small tumors. There are different types of prostate tumor. The term "primary tumor" refers to the original tumor; secondary tumors are caused when the original cancer spreads to other locations in the body. In the early stage, prostate cancer typically is comprised of multiple very small, primary tumors within the prostate. At this stage, the disease is often curable (rates of 90% or better) with a wide range of treatments, such as external beam radiotherapy (2), surgery (radical prostatectomy), brachytherapy and hormone therapy (androgen deprivation therapy) (3), that aim to remove or kill all cancerous cells in the prostate (4). Unfortunately, at the early stage the cancer produces few or no symptoms and can be difficult to detect. The use of prostate-specific antigen (PSA) testing has allowed physicians to detect prostate tumors before the primary tumor spreads (5).

PSA is an enzyme produced by cells in the prostate that is found in the seminal fluid and the bloodstream. Although with a name specific to prostate, PSA is produced by other tissues as well, such as breast tissue and the periurethral glands. Prostate cancer tends

to elevate the PSA level in the bloodstream but an elevated PSA level does not necessarily indicate prostate cancer, since PSA can also be raised by infection or other prostate conditions. For diagnosis of prostate cancer in asymptomatic men, clinical practice guidelines recommend the use of both PSA and digital rectal exam, in which a physician will insert a gloved finger into the rectum to feel the peripheral zone of the prostate where most prostate cancers occur. Detection of the prostate cancer at an earlier stage is very important and can significantly increase the cure rate (5, 6).

If the prostate tumor is undetected and untreated, the cells from these tumors can spread through the lymphatic system and the bloodstream to other parts of the body where they lodge and form secondary tumors. This process is called metastasis. Once the cancer spreads beyond the prostate gland (30,000 – 40,000 cases annually in the US), the treatment options are largely ineffective and the cure rates drop dramatically. Metastatic prostate cancer responds initially to hormone therapy but the majority of patients develop hormone-resistant disease that in 80% of cases will develop metastases in bone. Chemotherapy is largely ineffective due to systemic toxicity (7). Bone-seeking radiopharmaceuticals are used for palliative relief of pain. The attachment of radioisotopes to tumor-specific monoclonal antibodies (Radioimmunotherapy) is an experimental approach being evaluated against both blood-borne tumors (leukemia) and metastatic solid tumors including prostate (8, 9).

1.1.2 Radioimmunotherapy

Radioimmunotherapy offers the potential for exquisite targeting of radionuclides to microscopic metastatic sites (9). Monoclonal antibodies recognize the antigenic determinant (epitope) on the surface of specific cancer cells and bind to it. The antibodies

can be used in two ways: conjugated or unconjugated. The unconjuaged or "naked" antibodies can kill cancer cells by enhancing complement fixation or initiating antibody-dependent cell-mediated cytotoxicity. They may also exert antitumor activity by modulating signaling pathways activated by the cell surface target to which they bind. When conjugated, antibodies can be used to deliver a variety of toxic agents to tumor cells. Antibodies can be conjugated to radioisotopes, cytotoxic agents or immunotoxins. Antibodies currently being investigated for prostate cancer include those that target tumor-specific antigens, such as mucin and prostate specific membrane antigen PSMA, cell surface receptors such as epidermal growth factor receptor EGFR, and immunostimulatory molecules such as CTLA-4, an antigen expressed on T cells. Radioimmunotherapy or RIT has been used for the treatment of leukemia and lymphoma. Compared with external radiation beam therapy, in which a limited area of the body is irradiated, and with chemotherapy in which the treatment is systemic and the therapy depends on the differences in drug toxicity between normal tissue and the tumor, systemic targeted radioimmunotherapy delivers the toxic substance – radiation – to the site of the tumor by monoclonal antibody. The radioisotope is linked to the monoclonal antibody by a chemical linkage that includes a specifically designed chemical chelator linkage to hold the radioisotope (9).

Multiple considerations are involved in selection of the therapeutic radioisotope. Ready availability and a half-life sufficiently long for formulation and delivery are clearly important. A major consideration is the path length of the decay particle, which can range from < 1 μm for Auger electrons to millimeters for some beta particles. The radioisotopes that are most commonly used in RIT are the β-particle-emitting radioisotopes, such as

iodine-131 (I-131) (8, 10, 11), yttrium-90 (Y-90) (11-14) and samarium-153 (Sm-153) (14, 15). I-131 is a beta decay product from tellurium-131. It has a half-life of eight days and decays by emitting a beta particle, forming a stable isotope of xenon-131, (decay energy: 0.971 MeV). It also gives off gamma radiation, which can be imaged with a standard gamma camera. Y-90 is the decay product of strontium-90. Y-90 has a half-life of 64 hours and decays to zirconium-90 by emitting a beta particle (decay energy: 2.282 MeV). There is essentially no gamma radiation associated with the decay of Yt-90, making it hard to image directly. Sm-153 is a beta decay product from promethium-153. Sm-153 has a half life of 46 hours and decays to europium-153 by emitting a beta particle, (decay energy: 0.808 MeV). β-particles emitted from these radioisotopes have maximum energies from 0.5 to 2.0 MeV and ranges of 1-10 mm in tissue, which are much larger than the diameter of a cell. This causes problems because the neighboring normal cells also receive a radiation dose even when the radioisotope is attached only to the tumor cells. Meanwhile, compared to high-LET (linear energy transfer) radiation such as alpha particles, protons and neutrons, the relatively low LET and small RBE (relative biological effect) of β-rays make them not very efficient in killing tumor cells. While successful in some applications, such as thyroid cancer and lymphoma, β-particle RIT has generally been disappointing, requiring high activities to compensate for poor overall efficiency in clinical trials (16).

To limit alpha-particle emitters deposit a large amount of energy over a short track length, and consequently a few alpha particles through the nucleus are sufficient to kill a cell (17-19). For example, by one dosimetric calculation, 8 alpha particle decays per cell (average dose 8 Gy) can provide 4 logs of cell killing, while 9,600 beta particles (average dose 30 Gy) would be required for the same effect (19). In addition, the cytotoxicity of

alpha particles is not affected by oxygen. Due to the short range, little collateral damage may be inflicted upon non-targeted cells so less side effects would be caused. Alpha emitters have the potential to yield a more homogeneous distribution of dose within a tumor, particularly in micrometastatic sites, compared to the longer-range beta emitters (20). It has been calculated that 60% of the radiation energy from a uniformly distributed alpha emitter is absorbed within a 100 μm diameter spheroid, while only 2% of the energy from a beta emitter is retained within a spheroid this size (19). As a result, alpha-particle therapy has received renewed interest recently, especially with bismuth-212 and bismuth-213, which can be eluted from radium-224 and actinium-225 generators, respectively (21). There are other alpha-particle emitting radioisotopes of therapeutic interests such as terbium-149, astatine-211 and actinium-225. Their properties are listed in table 1.

Table 1-1. The alpha-particle emitting radioisotopes of current interest in RIT (21)

Radioisotope	Half-life	Alpha-particle Energy (MeV)	Branching ratio (%)	Range (μm)
Terbium-149	4 h	3.97	17	26
Astatine-211	7.21 h	6.0 7.5	41.7 58.3	65 75
Bismuth-212	1 h	8.79 6.0	64 36	87 65
Bismuth-213	45.6 min	8.4 5.9	97.8 2.2	80 58
Actinium-225	10 days	6.0 6.0 7.0 8.4 5.9	100 100 100 97.8 2.2	65 65 70 85 58

In principle, alpha-emitting radionuclides are significantly more selective and potent in killing targeted cells. They have been proposed for use in single-cell disorders, such as leukemia, lymphoma and micrometastatic carcinomas (9, 17). Promising results for

alpha-emitting actinium antibody conjugates were recently reported in mouse xenograft models (22). However, the short range of the alpha particles (20 - 90 μm in tissue, depending on the energy), together with the limited penetration of the monoclonal antibodies or monoclonal antibody fragment into the tumor site, make it difficult to deliver a lethal dose to cells at depth in the tumor. Radioimmunotherapy has had most success in bloodborne tumors where access of the antibody to the tumor cells is unimpeded (13). In solid tumors, however, radioimmunotherapy has had only limited success due largely to the problems associated with non-uniform binding of the radioimmunoconjugate to the tumor and/or poor penetration of the antibody into tumor sites (23, 24).

1.1.3 The bystander effect

Until a decade ago, it had been generally accepted that the important biological effects of ionizing radiation in mammalian cells were direct consequences of un-repaired or mis-repaired DNA damage in the irradiated cells. It was presumed that no effect would be expected in cells that receive no direct radiation. However, recent experimental evidence, mainly from *in vitro* alpha-particle studies, indicated that ionizing radiation could also cause biological effects, including DNA damage, by mechanisms that are independent of nuclear traversal: cells in the vicinity of directly irradiated cells or recipients of medium from an irradiated culture can also show damage response (25-29). The radiation-induced bystander effect has been broadly defined as referring to the occurrence of biological effects in un-irradiated cells as a result of exposure of other cells to ionizing irradiation. The "bystander effect" was first described by Nagasawa and Little using low doses of alpha particles and sister chromatid exchange as endpoint (25). The fraction of Chinese Hamster ovary cells traversed by an alpha particle was calculated to be

less than 1%, but over 30% of cells showed chromosome damage (sister chromatid exchange). These results indicated that the target for genetic damage by alpha particles is much larger than the nucleus or even the cell itself. Since then, the literature on the bystander effect has expanded enormously. Other endpoints for bystander responses include gene mutations, micronucleus formation, apoptosis, changes in gene expression, oncogenic transformation and cell survival (28, 30-35).

The bystander effect is actually a class of effects that differs with cell type, endpoint and in actual mechanism (33, 34). Radiation induced bystander effects are under intense investigation in the radiation protection area, where the effects predominate at low doses and have been discussed mainly in terms of the impact on low-dose risk assessment. As a result, most of the bystander effect studies have been done with normal cell lines. The relevance of the bystander effect *in vivo* remains unclear. There have been very few studies of the bystander effect in three dimensional cell systems. Mothersill irradiated human urothelium explants and showed that the overlying medium could cause effects in unirradiated urothelium explants or cells in culture (36). Howell has used pelleted mixtures of V79 hamster fibroblasts, some with ^{125}I incorporated into the DNA, to show cell killing in a greater fraction of cells than was labeled; interpreted as evidence of a bystander effect in the cell pellet (37, 38). All of the above studies used normal cells or tissues. Carcinoma cells have been shown to undergo a bystander effect *in vitro*, where cells not directly irradiated, nevertheless die (39), and *in vivo*, where the specific irradiation of human tumor cells leads to a bystander effect in subcutaneously growing tumors (40).

These recent reports of bystander effects in tumor cells, together with the need to improve the uniformity of cell kill during targeted alpha-particle therapies of solid tumors

or micrometastatic disease prompted the studies described in this paper. In this project, we focus on the possible therapeutic implications of the bystander effect in RIT to see whether the bystander effect can be manipulated or exploited to increase the level of tumor cell kill in those cells not directly targeted with the alpha particles. (A more detailed background of the bystander effect will be given at the beginning of Chapter 4)

1.1.4 Combined modality therapy and synergy effect

There is a long history of attempts to combine radiation and chemotherapy with the hope of producing specific interactions that can enhance cytotoxicity in the tumor, but not in critical normal tissues. In 1979, Steel proposed a nomenclature for mechanisms by which radiation and chemotherapy might be combined (41). Synergistic effects between chemotherapy drugs and low LET irradiation (X-ray and gamma irradiation) have been reported in various cancer types, both *in vitro* and *in vivo* (42-48). Paclitaxel (Taxol), a microtubule stabilizer, has demonstrated efficacy in the treatment of various types of cancers (49-52). Taxol is also a potential radiation sensitizer. It has shown synergistic enhancement with both external beam radiation therapy (53) and Y-90 conjugated radioimmunotherapy in breast cancer (54, 55), ovarian cancer (56), prostate cancer (57) and lung cancer (43). Another chemotherapy drug Oxaliplatin, which forms reactive platinum complexes and interferes in the work of DNA repair enzymes, was also reported to demonstrate irradiation sensitizing activity, both *in vitro* and *in vivo* (46, 58). Hydroxymethylacyflulvene (HMAF), a novel agent with alkylating activity and a potent inducer of apoptosis, was shown to work with gamma irradiation additively or synergistically in inducing apoptosis in several prostate tumor cell lines, but not in normal cells (59). Most of the synergy studies have been investigated with low-LET irradiations.

Our studies, however, look into the combinational effects of chemotherapeutic drugs and high-LET alpha-particle irradiation. (A more detailed background of combined modality therapy will be given at the beginning of Chapter 5.)

1.2 Objective

This project will contribute to the overall goal of improving the effectiveness of radiation therapy for metastatic prostate carcinoma. The role that the bystander effect plays in damaging the non-irradiated tumor cells and the mechanisms of the bystander effect were investigated when the prostate tumor cells were irradiated with alpha particles. A combined modality study using alpha particles and chemotherapeutic drugs that have been reported to act synergistically when combined with gamma or beta irradiation, was carried out. Finally, as a brand new topic, the interactions between the chemotherapeutic drugs and the bystander effect were investigated. Potential synergistic effects between the drugs and alpha-particle-based radioimmunotherapy for prostate tumor cells could improve the clinical management of this disease at an early stage.

1.3 Study Design

Part 1: An alpha particle irradiator was designed, constructed and calibrated. Alpha particle fluxes were measured using a track-etch detector and the alpha-particle energy spectra were measured with a solid-state semiconductor detector. The dose rates to monolayer cells were calculated for different experimental conditions. The irradiator has been used for several alpha-particle irradiation studies and has proven to be consistent and convenient. (Chapter 2)

Part 2: The biologic effects of alpha-particle irradiation on the human prostate tumor cell line DU-145 were examined with three endpoints: the clonogenic assay (at population-level), the comet assay (at single-cell level) and micronucleus formation. (Chapter 3)

Part 3: Two experimental models were used to study the bystander effect (Chapter 4):

- Grids model: Three plastic mesh grids were designed and fabricated that can be interposed between the alpha-particle source and the Mylar bottoms of the cell dishes to block part of the monolayer of cells from the alpha-particle irradiation. As a result, two subpopulations of cells were formed - cells that were directly subject to alpha particle irradiation (hit cells) and the non-hit, neighboring cells. The clonogenic assay was used to measure if there is a bystander effect in those non-hit, neighboring cells.

- Co-culture model: A novel co-culture system was designed that enabled two layers of cells growing in the same medium. The cells growing on the bottom Mylar membrane were directly exposed to alpha particles. The cells co-cultivated on the inserts, positioned ~4 mm above the bottom cell layer and out of the range of the alpha particles, served as the non-targeted bystander cells. DNA damage, as measured by micronucleus (MN) formation in the non-targeted prostate tumor cells was used as a measure of the bystander effect.

Chapter 5: The effects of two chemotherapeutic drugs, Taxol and Oxaliplatin on the DU-145 cells were studied first. The combined effects of each drug with high-LET alpha-particle irradiation as well as the interactions between the drugs and the bystander effect *in vitro* were examined, with the hope of an enhanced toxicity or synergistic effect. A

synergetic effect *in vitro* indicates a possibility of beneficial combined drug-irradiation therapy *in vivo*.

Once established, this model system can be used to test for the synergistic effects in combined modality studies using other drugs and other cell lines.

The results of the model studies carried out in the two-dimensional monolayer of cells in this project can serve as a fundamental frame work to be further applied to a three dimensional tumor micrometastasis model – spheroids – in the future. The understanding of the role the bystander effect plays in tumor cell killing and its mechanisms may make it possible to manipulate these factors to improve the effectiveness of radioimmunotherapy. The ability of the treatment to increase the cell kill at depths beyond the range of the alpha particles will provide the ultimate test of this combined modality therapy.

References:

1. Jemal, A., Tiwari, R. C., Murray, T., Ghafoor, A., Samuels, A., Ward, E., Feuer, E. J., and Thun, M. J. Cancer statistics, 2004. CA Cancer J Clin, *54:* 8-29, 2004.
2. Pisansky, T. External beam radiotherapy as curative treatment of prostate cancer. Mayo Clin Proc, *80:* 883-898, 2005.
3. Drudge-Coates, L. Prostate cancer and the principles of hormone therapy. Br J Nurs, *14:* 368-375, 2005.
4. Trojan L, K. K., Knoll T, Alken P, Michel MS Prostate cancer therapy: standard management, new options and experimental approaches. Anticancer Res, *25:* 551-561, 2005.
5. Routh JC, L. B. Adenocarcinoma of the prostate: epidemiological trends, screening, diagnosis, and surgical management of localized disease. Mayo Clin Proc, *80:* 899-907, 2005.
6. Cohen S, S. S., Kelty P PSA screening. Med Health R I., *88:* 90-91, 2005.
7. Smith, D. C. Chemotherapy for hormone refractory prostate cancer. Urol Clin North Am, *26:* 323-331, 1999.
8. Meredith, R. F., Khazaeli, M. B., Macey, D. J., Grizzle, W. E., Mayo, M., Schlom, J., Russell, C. D., and LoBuglio, A. F. Phase II study of interferon-enhanced 131I-labeled high affinity CC49 monoclonal antibody therapy in patients with metastatic prostate cancer. Clin Cancer Res, *5:* 3254s-3258s, 1999.
9. McDevitt, M. R., Barendswaard, E., Ma, D., Lai, L., Curcio, M. J., Sgouros, G., Ballangrud, A. M., Yang, W. H., Finn, R. D., Pellegrini, V., Geerlings, M. W., Jr., Lee, M., Brechbiel, M. W., Bander, N. H., Cordon-Cardo, C., and Scheinberg, D. A. An alpha-particle emitting antibody ([213Bi]J591) for radioimmunotherapy of prostate cancer. Cancer Res, *60:* 6095-6100, 2000.
10. Denardo, S. J., O'Grady, L. F., Richman, C. M., Goldstein, D. S., O'Donnell, R. T., Denardo, D. A., Kroger, L. A., Lamborn, K. R., Hellstrom, K. E., Hellstrom, I., and Denardo, G. L. Radioimmunotherapy for advanced breast cancer using I-131-ChL6 antibody. Anticancer Res, *17:* 1745-1751., 1997.
11. Vallabhajosula, S., Smith-Jones, P. M., Navarro, V., Goldsmith, S. J., and Bander, N. H. Radioimmunotherapy of prostate cancer in human xenografts using monoclonal antibodies specific to prostate specific membrane antigen (PSMA): studies in nude mice. Prostate, *58:* 145-155, 2004.
12. Boiardi, A., Bartolomei, M., Silvani, A., Eoli, M., Salmaggi, A., Lamperti, E., Milanesi, I., Botturi, A., Rocca, P., Bodei, L., Broggi, G., and Paganelli, G. Intratumoral delivery of mitoxantrone in association with 90-Y radioimmunotherapy (RIT) in recurrent glioblastoma. J Neurooncol, *72:* 125-131, 2005.
13. Ma, D., McDevitt, M. R., Barendswaard, E., Lai, L., Curcio, M. J., Pellegrini, V., Brechbiel, M. W., and Scheinberg, D. A. Radioimmunotherapy for model B cell malignancies using 90Y-labeled anti-CD19 and anti-CD20 monoclonal antibodies. Leukemia, *16:* 60-66, 2002.
14. Li, G., Zhang, H., and Zhu, C. Radioimmunotherapy with 153Sm-CEA monoclonal antibody in nude mice bearing human colon carcinoma: an experimental study. Di Yi Jun Yi Da Xue Xue Bao, *23:* 1-5, 2003.

15. Fani, M., Vranjes, S., Archimandritis, S., Potamianos, S., Xanthopoulos, S., Bouziotis, P., and Varvarigou, A. Labeling of monoclonal antibodies with 153Sm for potential use in radioimmunotherapy. Appl Radiat Isot, *57:* 665-674, 2002.
16. PW, J. The emerging role of radioimmunotherapy in hematological malignancies. Br. J. Haematol, *108:* 679-688, 2000.
17. Allen, B. J. Targeted alpha therapy: evidence for potential efficacy of alpha-immunoconjugates in the management of micrometastatic cancer. Australas Radiol, *43:* 480-486, 1999.
18. Waldmann, T. ABCs of radioisotopes used for radioimmunotherapy: alpha- and beta-emitters. Leuk Lymphoma, *44:* S107-113, 2003.
19. Imam, S. K. Advancements in cancer therapy with alpha-emitters: a review. Int J Radiat Oncol Biol Phys, *51:* 271-278, 2001.
20. Ballangrud, A. M., Yang, W. H., Charlton, D. E., McDevitt, M. R., Hamacher, K. A., Panageas, K. S., Ma, D., Bander, N. H., Scheinberg, D. A., and Sgouros, G. Response of LNCaP spheroids after treatment with an alpha-particle emitter (213Bi)-labeled anti-prostate-specific membrane antigen antibody (J591). Cancer Res, *61:* 2008-2014, 2001.
21. McDevitt, M. R., Sgouros, G., Finn, R. D., Humm, J. L., Jurcic, J. G., Larson, S. M., and Scheinberg, D. A. Radioimmunotherapy with alpha-emitting nuclides. Eur J Nucl Med, *25:* 1341-1351, 1998.
22. McDevitt, M. R., Ma, D., Lai, L. T., Simon, J., Borchardt, P., Frank, R. K., Wu, K., Pellegrini, V., Curcio, M. J., Miederer, M., Bander, N. H., and Scheinberg, D. A. Tumor therapy with targeted atomic nanogenerators. Science, *294:* 1537-1540, 2001.
23. Koppe, M., Bleichrodt, R., Oyen, W., and Boerman, O. Radioimmunotherapy and colorectal cancer. Br J Surg, *92:* 264-276, 2005.
24. DeNardo, G. L., O'Donnell, R. T., Kroger, L. A., Richman, C. M., Goldstein, D. S., Shen, S., and DeNardo, S. J. Strategies for developing effective radioimmunotherapy for solid tumors. Clin Cancer Res, *5:* 3219s-3223s, 1999.
25. Nagasawa, H. and Little, J. B. Induction of sister chromatid exchanges by extremely low doses of alpha-particles. Cancer Res, *52:* 6394-6396, 1992.
26. Azzam, E. I. and Little, J. B. The radiation-induced bystander effect: evidence and significance. Hum Exp Toxicol, *23:* 61-65, 2004.
27. Azzam, E. I., de Toledo, S. M., and Little, J. B. Stress signaling from irradiated to non-irradiated cells. Curr Cancer Drug Targets, *4:* 53-64, 2004.
28. Nagasawa, H. and Little, J. B. Unexpected sensitivity to the induction of mutations by very low doses of alpha-particle radiation: evidence for a bystander effect. Radiat Res, *152:* 552-557, 1999.
29. Huo, L., Nagasawa, H., and Little, J. B. HPRT mutants induced in bystander cells by very low fluences of alpha particles result primarily from point mutations. Radiat Res, *156:* 521-525, 2001.
30. Prise, K. M., Belyakov, O. V., Folkard, M., and Michael, B. D. Studies of bystander effects in human fibroblasts using a charged particle microbeam. Int J Radiat Biol, *74:* 793-798, 1998.

31. Zhou, H., Randers-Pehrson, G., Waldren, C. A., Vannais, D., Hall, E. J., and Hei, T. K. Induction of a bystander mutagenic effect of alpha particles in mammalian cells. Proc Natl Acad Sci U S A, *97:* 2099-2104, 2000.
32. Azzam, E. I., de Toledo, S. M., and Little, J. B. Oxidative metabolism, gap junctions and the ionizing radiation-induced bystander effect. Oncogene, *22:* 7050-7057, 2003.
33. Mothersill, C. and Seymour, C. Radiation-induced bystander effects: past history and future directions. Radiat Res, *155:* 759-767, 2001.
34. Prise, K. M., Folkard, M., and Michael, B. D. A review of the bystander effect and its implications for low-dose exposure. Radiat Prot Dosimetry, *104:* 347-355, 2003.
35. McBride, W. H., Chiang, C. S., Olson, J. L., Wang, C. C., Hong, J. H., Pajonk, F., Dougherty, G. J., Iwamoto, K. S., Pervan, M., and Liao, Y. P. A sense of danger from radiation. Radiat Res, *162:* 1-19, 2004.
36. Mothersill, C., Rea, D., Wright, E. G., Lorimore, S. A., Murphy, D., Seymour, C. B., and O'Malley, K. Individual variation in the production of a 'bystander signal' following irradiation of primary cultures of normal human urothelium. Carcinogenesis, *22:* 1465-1471, 2001.
37. Bishayee, A., Hill, H. Z., Stein, D., Rao, D. V., and Howell, R. W. Free radical-initiated and gap junction-mediated bystander effect due to nonuniform distribution of incorporated radioactivity in a three-dimensional tissue culture model. Radiat Res, *155:* 335-344, 2001.
38. Howell, R. W. and Bishayee, A. Bystander effects caused by nonuniform distributions of DNA-incorporated (125)I. Micron, *33:* 127-132, 2002.
39. Carlin, S., Cunningham, S. H., Boyd, M., McCluskey, A. G., and Mairs, R. J. Experimental targeted radioiodide therapy following transfection of the sodium iodide symporter gene: effect on clonogenicity in both two-and three-dimensional models. Cancer Gene Ther, *7:* 1529-1536, 2000.
40. Kassis, A. I. In vivo validation of the bystander effect. Hum Exp Toxicol, *23:* 71-73, 2004.
41. Steel, G. Terminology in the description of drug-radiation interactions. Int J Radiat Oncol Biol Phys 1145-1150, 1979.
42. Lokeshwar, B., Ferrell, S., and Block, N. Enhancement of radiation response of prostatic carcinoma by taxol: therapeutic potential for late-stage malignancy. Anticancer Res, *15:* 93-98, 1995.
43. Choy, H. and Browne, M. J. Paclitaxel as a radiation sensitizer in non-small lung cancer. Semin Oncol 70-74, 1995.
44. Leonard, C., Chan, D., Chou, T., Kumar, R., and Bunn, P. Paclitaxel enhances in vitro radiosensitivity of squamous carcinoma cell lines of the head and neck. Cancer Res, *56:* 5198-5204, 1996.
45. Algur, E., Macklis, R., and Hafeli, U. Synergistic cytotoxic effects of zoledronic acid and radiation in human prostate cancer and myeloma cell lines. Int J Radiat Oncol Biol Phys, *61:* 535-542, 2005.
46. Cividalli, A., Ceciarelli, F., Livdi, E., Altavista, P., Cruciani, G., Marchetti, P., and Danesi, D. T. Radiosensitization by oxaliplatin in a mouse adenocarcinoma: influence of treatment schedule. Int J Radiat Oncol Biol Phys, *52:* 1092-1098, 2002.

47. Liebmann, J., Cook, J. A., Fisher, J., Teague, D., and Mitchell, J. B. In Vitro Studies of Taxol as a Radiation Sensitizer in Human Tumor Cells. J Natl Cancer Inst, *86:* 441-446, 1994.
48. Espinosa, M., Martinez, M., Aguilar, J. L., Mota, A., Garza, J. G. D. l., Maldonado, V., and Meléndez-Zajgla, J. Oxaliplatin activity in head and neck cancer cell lines. Cancer Chemotherapy and Pharmacology, *55:* 301-305, 2004.
49. Crown, J., O'Leary, M., and Ooi, W. Docetaxel and paclitaxel in the treatment of breast cancer: a review of clinical experience. Oncologist, *9:* 24-32, 2004.
50. Young, M. and Plosker, G. Paclitaxel: a pharmacoeconomic review of its use in the treatment of ovarian cancer. Pharmacoeconomics, *19:* 1227-1259, 2001.
51. Plosker, G. and Hurst, M. Paclitaxel: a pharmacoeconomic review of its use in non-small cell lung cancer. Pharmacoeconomics, *19:* 1111-1134, 2001.
52. Spencer, C. and Faulds, D. Paclitaxel. A review of its pharmacodynamic and pharmacokinetic properties and therapeutic potential in the treatment of cancer. Drugs, *48:* 794-847, 1994.
53. Geard, C. R., Jones, J. M., and Schiff, P. B. Taxol and radiation. J Natl Cancer Inst Monogr 89-94, 1993.
54. DeNardo, S. J., Kukis, D. L., Kroger, L. A., O'Donnell, R. T., Lamborn, K. R., Miers, L. A., DeNardo, D. G., Meares, C. F., and DeNardo, G. L. Synergy of Taxol and radioimmunotherapy with yttrium-90-labeled chimeric L6 antibody: efficacy and toxicity in breast cancer xenografts. Proc Natl Acad Sci U S A, *94:* 4000-4004, 1997.
55. DeNardo, S. J., Kroger, L. A., Lamborn, K. R., Miers, L. A., O'Donnell, R. T., Kukis, D. L., Richman, C. M., and DeNardo, G. L. Importance of temporal relationships in combined modality radioimmunotherapy of breast carcinoma. Cancer, *80:* 2583-2590 [pii], 1997.
56. Genevieve Griffon-Etienne, J.-L. M. a. C. M. Association of docetaxel/paclitaxel with irradiation in ovarian carcinoma cell lines in bidimensional (sulforhodamine B assay) and tridimensional (spheroids) cultures. Anti-Cancer Drugs 660-670, 1996.
57. O'Donnell, R. T., DeNardo, S. J., Miers, L. A., Lamborn, K. R., Kukis, D. L., DeNardo, G. L., and Meyers, F. J. Combined modality radioimmunotherapy for human prostate cancer xenografts with taxanes and 90yttrium-DOTA-peptide-ChL6. Prostate, *50:* 27-37, 2002.
58. Blackstock, A., Tepper, J., Hess, S. Oxaliplatin: In vitro and in vivo evidence of its radiation sensitizing activity (Abstr). Int J Radiat Oncol Biol Phys 724, 2000.
59. Woynarowska, B. A., Roberts K., Woynarowski J. M. , MacDonald J. R. and Herman, T. S. Targeting Apoptosis by Hydroxymethylacylfulvene in Combination with Gamma Radiation in Prostate Tumor Cells. Radiation Research 429-438, 2000.

Chapter 2 Bench-top Alpha-Particle Irradiator

2.1 Introduction

Alpha particles are a type of ionizing radiation. Ernest Rutherford discovered alpha particles in 1899 while working with uranium. They are large subatomic fragments consisting of 2 protons and 2 neutrons. An alpha particle is identical to a helium nucleus. It is a relatively heavy, high-energy particle, with a positive charge of two. Alpha-emitting atoms are usually large atoms with atomic numbers of 82 or more. There are many alpha-emitting radioactive elements, both natural and manmade, for examples: americium-241 (Am-241), plutonium-236 (Pu-236), uranium-238 (U-238), radium-226 (Ra-226), radon-222 (Rn-222) and polonium-210 (Po-210). Compared to X-rays or γ-rays, which are electromagnetic radiations, alpha particles belong to a category called particulate radiations.

The positive charge of alpha particles is useful in some industrial processes. For example, polonium-210 serves as a static eliminator in paper mills and other industries. The alpha particles, due to their positive charge, attract loose electrons, thus reducing static charge. Some smoke detectors take advantage of alpha emissions from americium-241 to help create an electrical current. The alpha particles strike air molecules (oxygen and nitrogen) within a chamber, knocking electrons off. The resulting positively charged ions and negatively charged electrons create a steady current as they are collected by the positively and negatively charged plates in the chamber. When smoke particles enter the chamber, they attach to the ions and neutralize them. This causes the electric current to fall, which sets off an alarm.

When radiation is absorbed in biological material, the energy is deposited along the tracks of charged particles in a pattern that is characteristic of the type of radiation involved. After exposure to x or gamma rays, the ionization density would be quite low. After exposure to neutrons, protons, or alpha particles, the ionization along the tracks would occur much more frequently, producing a much denser pattern of ionizations. Linear energy transfer (LET) is used to quantify the energy transferred per unit length of the track. The special unit usually used for this quantity is kiloelectron volt per micrometer (keV/μm. According to this definition, alpha particles are considered high LET radiations, and X-rays are considered low LET radiations (1).

The interests of researchers in alpha-particle irradiation mainly come from the concern of radiation exposure to the general population from natural sources, which are dominated by the alpha-emitting radionuclides radon-222 (Rn-222) and its progeny. Radon is a gas produced by the radioactive decay of radium-226, which is a decay product of uranium-238. The major source of radon is the soil; ground water, natural gas and building material also contribute to some radon dose. Radon has three decay products: polonium, bismuth and lead. The great majority of the radiation dose is not from radon itself, but from the short-lived alpha-emitting radon daughters, most notably Po-218 (physical half-life $T_{1/2}$=3 minutes), and Po-214 ($T_{1/2}$=0.164 milliseconds), along with beta particles from Bi-214 ($T_{1/2}$=19.7 minutes). The external dose from Rn-222 and its airborne progeny is a very small fraction of the natural external radiation dose received by individuals. However, inhalation of radon and its daughters may be followed by deposition of potentially large amounts of energy, i.e. absorbed dose in the tracheobronchial epithelium from the short-lived α-particle emitting decay products, primarily from Po-218, Pb-214, Bi-214, and Po-

214. According to the National Council on Radiation Protection and Measurements (NCRP 1987), the average annual effective dose equivalent for United States citizens from inhaled radon and its progeny is about 2 mSv, which accounts for two thirds of the estimated total of 3 mSv individual dose equivalent per year. The major health risk from exposure to radon progeny is bronchogenic carcinoma and lung cancer.

For research purposes, it is possible to produce mono-energetic alpha particles from a linear accelerator or cyclotron. Accelerator-based microbeams (2), which can provide single-particle and single-cell irradiation, have very elegant applications in some fields like bystander effect studies. But the prohibitively high cost and the difficulties in running and maintaining the complicated machine force many investigators to turn to natural radionuclide sources. As a result, many *in vitro* radiobiological studies were carried out by utilizing an alpha-particle exposure apparatus made from wide-field radioactive sources like Po-210, Pu-238, Pu-239 or Am-241, or adding shorter-lived isotopes Ra-222 (3) and Bi-212 (3-6) directly to cell culture medium. The alpha particles generated from these radionuclides have energies of 5 to 9 MeV and total ranges between 35 to 90 μm in tissue-equivalent material. They lose energy along densely ionizing tracks, starting with an initial linear energy transfer (LET) from 60 to 90 keV /μm and reaching a maximum LET of about 250 keV/μm near the end of the track (7). Examples of such convenient alpha-particle irradiators include the bench-top alpha-particle irradiator in J. Little's laboratory at the Harvard School of Public Health (7) and the multi-port alpha-particle irradiator in R. W. Howell's laboratory at the New Jersey Medical School (8).

Our study was to investigate the effect of alpha-particle irradiation on human prostate tumor cells *in vitro*, with the purpose to explore the possibility of increasing tumor

cell killing through the bystander effect or synergistic effect. In order to implement this investigation, it was necessary to construct an alpha-particle irradiator with well-defined exposure conditions for irradiation of cell monolayers.

Two alpha-particle irradiators were designed, constructed and calibrated. The first one was very simple but had no mechanism to control the exposure time accurately for short exposures. The second design includes an electronic shutter and was proven to meet the requirements and was used in all experiments in this study, as well as several other research projects. Simulations were used to understand the influences of different thickness of air gap and Mylar/polypropylene film on the energy and LET spectra of the alpha particles at the position of the monolayer of cells. The energy spectra were measured using a passivated implanted planar silicon (PIPS) detector. The energy spectra were then translated into the LET spectra through published energy-LET tables for alpha particles. Two methods were used to measure the alpha-particle flux at the cell position: the PIPS detector and the CR-39 "track-etch" detector. The measuring results from the two different detectors were compared. The average dose rate to the monolayer of cells was calculated from the average alpha-particle flux and the average LET.

2.2 Materials and Methods

2.2.1 The alpha isotope foils

Five sealed Am-241 alpha foils were purchased from NRD LLC, Grand Island, NY. Am-241 has a half life of 433 years. It decays to Np-237 by releasing an alpha particle and a low energy gamma ray: $^{241}_{95}Am=^{237}_{93}Np+^{4}_{2}He(\alpha)+\gamma$

From the 8th edition of the *Table of Isotopes*, the alpha-particle energies from the decay of Am-241 are (with branching ratio): 5.486 MeV (85.2%), 5.443 MeV (12.8%), 5.388 MeV (1.4%), 5.544 MeV (0.34%), and 5.512 MeV (0.2%). The weighted average energy is 5.476 MeV. The energy of the gamma ray with the highest branching ratio (36%) is 59.537 keV.

The Am-241 foils were produced by mining AmO_2 and gold powders into a 0.5-μm-thick active layer. The active layer was sandwiched between gold foil layers, mounted on a silver plate and electro-coated with an additional layer of gold (figure 2-1)

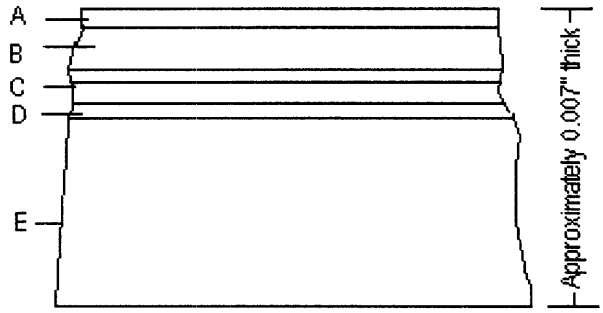

A: Gold plate 0.00005 cm

B: Gold, 0.0001 cm

C: Am-241 and gold, 0.00005 cm

D: Gold, 0.00076 cm

E: Silver, 0.018 cm

Figure 2-1. The layer structure of the Am-241 alpha foils

Am-241 alpha foil #	Active area (cm^2)	Nominal activity ($\mu Ci/cm^2$)	Total activity (mCi)
# 5	7.6×7.6	100	5.8
# 4	7.6×7.6	10	0.58
# 3	7.6×17.8	1	0.135
# 2	7.6×17.8	0.1	0.013
# 1	7.6×17.8	0.01	0.0013

Table 2-1. Dimensions and activities for the five Am-241 alpha foils

Different applications need different activities. The activities of the five foils obstained from the manufacturer vary by factors of 10. The dimensions and activities of

the foils are listed in Table 2-1. The total activity equals the product of the nominal activity and the active area.

2.2.2 The alpha-particle irradiator

In 1995, Noelle F. Metting, Hatsumi Nagasawa and John B. Little at the Harvard School of Public Health published a paper describing the design, construction and calibration of a collimated Pu-238 alpha-particle irradiator. In their construction, a plexiglas beam delimiter and a stainless steel honeycomb collimator were used to constrain the direction of the beam. The source and collimator were located in a helium-filled plexiglass box, with a 1.5μm-thick Mylar exit window to separate the inside helium gas from the outside air. A Copal shutter was located above the Mylar exit window and used to control the radiation time. Alpha particles traveled through 42 mm of helium gas, 1.5 μm Mylar (the exit window), 6 mm of air, and the 1.5 μm thick Mylar bottom of a custom-built cell culture dish to reach the monolayer of cells (7).

Based on the above design, Prasad Neti and Roger Howell at the New Jersey Medical School built an advanced multi-port alpha-particle irradiator (figure 2-2). Four individual planar Am-241 alpha-particle sources (NRD Inc., Buffalo, NY) are housed inside a helium-filled Plexiglas box (53.34 x 40.64 x 20.32 cm). Three of the radioactive sources consist of 0.540 mCi (60 mCi/in^2) each of ^{241}Am oxide foil. The fourth source, used to produce higher dose-rates, consists of 13.5 mCi (1500 mCi/in^2). Americium-241 emits alpha particles with almost the same energy as ^{238}Pu, the source used in the original Metting design. The foil is comprised of a silver overcoat and undercoat, silver plus ^{241}Am oxide active layer, and 0.01524 cm thick silver backing that is welded and rolled. The foil was fabricated with the active layer centered between 2 inactive margins. The result is a

planar 7.62 x 7.62 cm source that emits 4.7 MeV alpha particles (0.7 MeV FWHM). The four sources are mounted parallel to their respective 1.5-μm-thick Mylar exit windows on turntables rotated at 88 rpm. The turntables are included to ensure uniform irradiation of the Mylar-bottomed cell culture dishes. A stainless-steel honeycomb collimator is placed between the four sources and their exit windows by a cantilever attachment to the platform of an orbital shaker (Roto Mix, Thermolyne) that moves its table in an orbit of 1.9 cm. During the irradiation the collimator is moved at 150 orbits per minute. Each exit window is equipped with a beam delimiter to optimize the uniformity of the beam and a high precision electronic Copal specialty shutter (model DC-392). Opening and closing of the shutters is controlled with a high precision timer (Logotron LGT 12C DC, Entrelec). The specially designed stainless steel Mylar-bottomed dishes are placed on an adaptor on the shutter. The latter allows irradiation of the monolayer over times ranging from 0.01 s to 20 min. (8).

Figure 2-2. The multi-port alpha-particle irradiator built in Roger Howell's Lab (8)

Based on these two designs, we aimed to build a more flexible and convenient irradiator to facilitate our studies.

2.2.2.1 The first design of irradiator

In the first design, as shown in figure 2-3, the Am-241 foil was adhered to the surface of the bottom aluminum plate with 2-sided tape. The upper aluminum plate with holes served as a holder for the Mylar dishes. There were three holes/holders for the bigger-size alpha foil #1, #2 and #3 to enable simultaneous irradiation of three cell dishes. Four screws were used to connect the two plates together with screw caps and thin washers in between. The distance (air gap) between the alpha foil and the Mylar bottom of the cell dishes was adjustable by changing the number of screw caps or washers. The advantage of this design was that the air gap could be easily adjusted, starting from virtually 0. The distance would affect the alpha-particle energy received by the monolayer of cells. The biggest drawback of this design was that with no shutter, it was hard to control the exposure time accurately, especially for very short exposures.

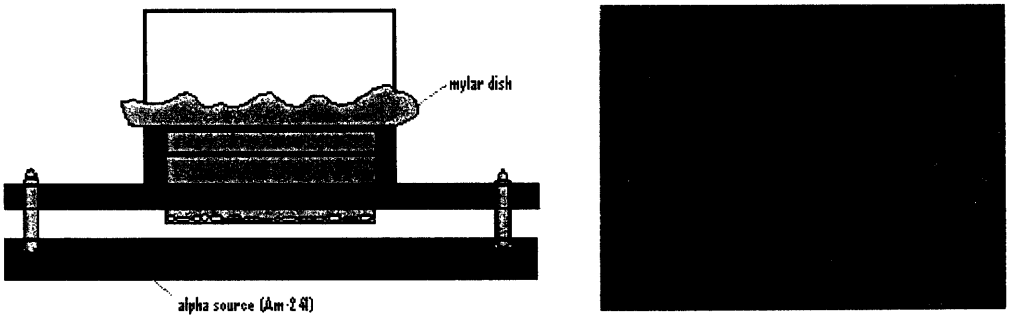

Figure 2-3. The first design of the alpha-particle irradiation system. The Am-241 foil was adhered to the surface of the bottom aluminum plate with 2-sided tape. The upper aluminum plate with holes served as a holder for the Mylar dishes.

2.2.2.2 The second design of irradiator

The second design (figure 2-4) solved the exposure control problem. A Copal electronic shutter (model DC-392) sitting right above the alpha foil was used to control the exposure time. A metal adaptor was made to hold the Mylar dish on the shutter so that the bottom of the Mylar dish was as close to the blades of the shutter as possible, which resulted in a 5 mm air gap between the alpha foil and the Mylar dish bottom. The system was located in a 185 mm × 185 mm lead-acrylic transparent box, with a lid not shown in the picture. The lead-acrylic box effectively shielded the 60 keV gamma rays and allowed the users to handle and use the irradiator more safely.

An external power supply (Model 250, GIBCO BRL, Life Technologies) was used to provide the 24 V voltage to open the electronic shutter. A single shot digi-set timing module (Part number: ENTTDUSL3002A from SSAC), connecting the power supply and the electronic shutter, was used to control the exposure time of the shutter accurately from 0.1 s to 100 s. Longer exposures could be controlled manually with the help of an external timer.

There was no collimator and delimiter in this design. The alpha particles hit the cells at all angles, theoretically. There was no rotation of either the alpha source or the cell dish. The uniformity of the alpha-particle hits was directly determined by the uniformity of the americium foil itself. The alpha-particle uniformity and the resulting energy spectrum to the monolayer of cells needed to be carefully examined before the irradiator was put into use.

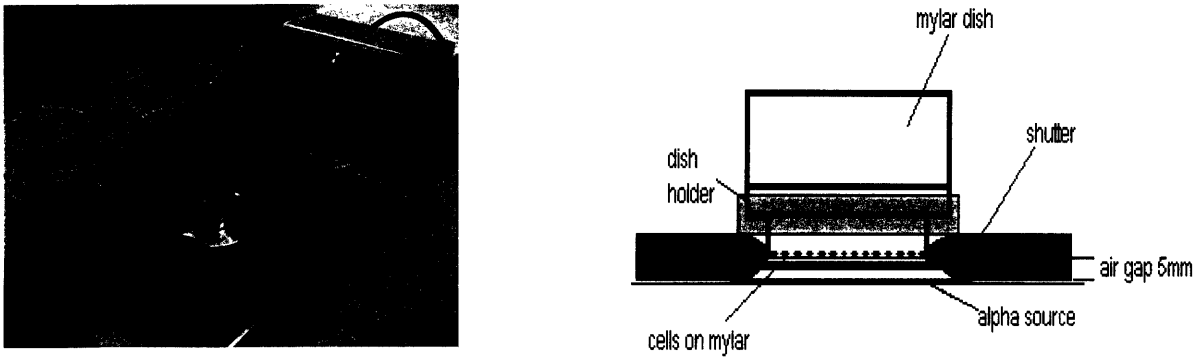

Figure 2-4. The second design of the alpha-particle irradiation system. The cells are grown on the Mylar membrane 5 mm above the surface of the alpha-emitting foil. An electronic shutter controls the exposure time.

2.2.2.3 The Mylar dish

Stainless steel cell culture dishes with replaceable Mylar-bottoms were constructed according to the prototype in Metting's paper (7). Some changes were made to enable the dish to fit into our own irradiator. A market search was done for the thinnest Mylar film commercially available. As a result, 1.4 μm-thick Mylar film was used to make the dish bottom, on which the cells were grown (Steinerfilm, Inc., Williamstown, MA). Cells do not attach well to Mylar, therefore pretreatment was needed to facilitate the attachment of cells. FNC coating mix from AthenaES (Athena Environmental Sciences, Inc. Baltimore, MD) was used to pre-coat the surface of the Mylar bottom before the cells were added. If not otherwise specified, the Mylar dish was always pre-coated for use in this paper. The cell culture dish had a total height of 4.05 cm and an inside diameter of 3.81 cm, providing a surface area of 11.4 cm^2 (figure 2-5).

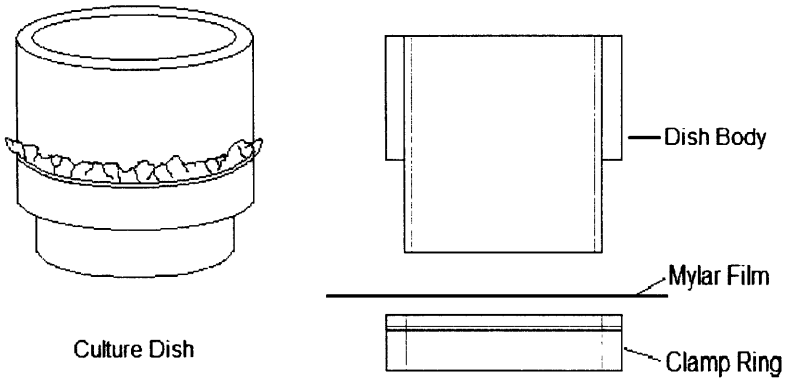

Figure 2-5. Schematic view of the Mylar dish. The Mylar dish was composed of three parts: the dish body, 1.4 μm-thick Mylar film and a clamp ring to tighten the Mylar film as dish bottom.

2.2.3 Simulations

Before the construction of the alpha-particle irradiator, simulations were utilized to estimate the energy spectra and LET spectra that cells would receive from a non-collimated alpha source, assuming it was a uniform source. The design parameters were not decided at the beginning, including the material of the film used as dish bottome (Mylar film or the polypropylene film), the thickness of the Mylar/polypropylene and the distance between the alpha foil and the dish bottom. By choosing different inputs, the SRIM simulations were used to examine the influences of these factors and variables on the energy spectra and LET spectra that the monolayer of cells received.

SRIM (the Stopping and Range of Ions in Matter) is a group of programs which calculate the stopping and range of ions (up to 2 GeV/amu) into matter using a quantum mechanical treatment of ion-atom collisions. TRIM (the Transport of Ions in Matter) is the most comprehensive program included. TRIM will accept complex targets made of compound materials with up to eight layers, each of different materials. It will calculate

both the final 3D distribution of the ions and also all kinetic phenomena associated with the ion's energy loss: target damage, sputtering, ionization, and photon production. All target atom cascades in the target are followed in detail. The programs were made so they could be interrupted at any time, and then resumed later. Plots of the calculation may be saved, and displayed when needed (9). The version used in this paper was SRIM 2003.

In order to run the simulation, two types of information were needed: the Ion Data and the Target Data (figure 2-6). The Ion Data included the name of the ion, the initial energy of the ion and the angle of incidence. The target consisted of multiple layers. The Target Data included the material and thickness of each layer. In our case, the alpha particles emitted from the foil would pass through a certain thickness of air, a thin Mylar/polypropene film and hit the monolayer of cells in the medium. For simplification, liquid water was used to represent the cell and medium layer due to the similarity in density and elemental components. Once a material was chosen, the program would give the overall density and the components of the material automatically. The program tracks the path of each individual ion and produces a record for it. The movement of all the ions could be visualized in four different views: XY Longitudinal, XZ Longitudinal, XY Ions Only and YZ Lateral. All the input information and results were output to the SRIM sub-directory "SRIM Output" in txt files. The easiest way to manipulate these files was to load them into a spreadsheet.

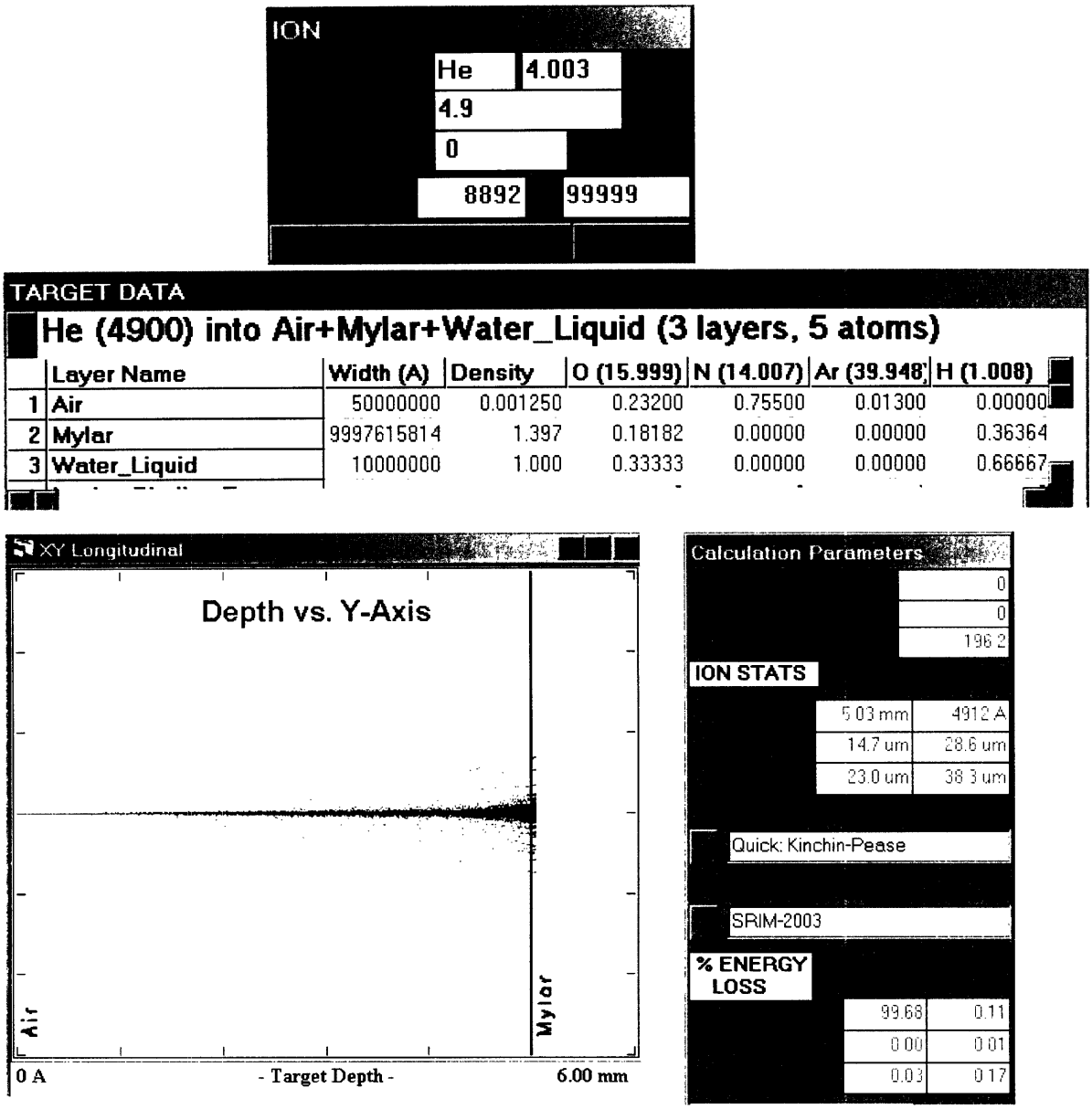

Figure 2-6. SRIM interface: *Top:* the Input data for the Ion, including ion name, initial incident energy, number of ions; *Middle*: the target data for each layer, including material and thickness; *Bottom Left:* the XY Longitudinal view of an ongoing simulation. *Bottom Right:* the calculation parameters and results for ion statistics.

2.2.4 Dosimetry Measurements

2.2.4.1 Alpha-particle energy spectra

A passivated implanted planar silicon (PIPS) detector (Canberra, Meriden, CT; model A450-18AM) (figure 2-7) was used to measure both the flux and the energy spectra of the ^{241}Am α-particles under different conditions. The detector active area is 450 mm^2; the energy resolution is 18 keV; the bias voltage used was 40 V. A multichannel analyzer software package (Canberra AccuSpec) was used to obtain alpha-particle energy spectra. The detector was calibrated by measuring a standard ^{241}Am point source in vacuum. The channel number corresponding to the peak of the ^{241}Am standard source was set to 5.486 MeV. The energy spectra of the alpha particles emitted from the ^{241}Am foils were measured directly above the gold surface of the foil, and in the cell irradiation position, i.e., inside the cell irradiation dish above the surface of the 1.4 μm-thick Mylar membrane. For the high-activity sources, the detector surface was shielded with a 0.025 mm-thick stainless steel foil containing a 0.8 mm-diameter pinhole to avoid count rate saturation (figure 2-8). Because the size of the pinhole was much larger than the thickness of the stainless steel foil, the collimation effect from the pinhole was minimal. The pinhole method was tested with a low activity source to verify that the count rate and the energy spectrum were the same with and without the pinhole. The alpha-particle flux was also measured by the system. A similar pinhole method was used to avoid count rate saturation and a large dead time. The alpha-particle flux was calculated by dividing the total number of recorded particles by the measurement time and the effective detector area.

Figure 2-7. The PIPS detector(Canberra, Meriden, CT; model A450-18AM). The active area of the detector is 450 mm2.

Figure 2-8. Schematic pinhole method. *Left:* the unshielded detector; *Right:* for the high-activity sources, the detector surface was shielded with a 0.025 mm-thick stainless steel foil containing a 0.8-mm-diameter pinhole to avoid count rate saturation. The drawing is not in proportion of the real situation. The distance between the source surface and the active area of the PIPS detector was about 5 mm.

2.2.4.2 Alpha-particle LET spectra

The LET spectrum of the alpha particles at the cell irradiation position was generated by converting the energy in each channel of the energy spectrum into the corresponding LET using the ASTAR program and the stopping power and range tables available in the National Institute of Standards and Technology database.

(http://physics.nist.gov/PhysRefData/Star/Text/ASTAR.html).

2.2.4.3 Alpha-particle flux uniformity

The alpha-particle flux at the cell irradiation position was also measured using a "track-etch" technique (10). The plastic track detector CR-39 is sensitive to damage by heavy charged particles but not to x-rays or gamma rays (10). All charged particles deposit energy along their trail when they travel through matter. In organic plastic materials this energy loss creates a submicroscopic cylinder of "damaged" molecules, the so-called latent track. This latent track is invisible under optical microscopes and it can be made visible by etching the exposed detector with appropriate chemical solutions, usually high concentration NaOH solution. In the etching solution, two etching processes happen at the same time: the bulk or material etching which removes a layer of the detector surface, and the track etching which produces cone-shape etch-pits (11) (see figure 2-9). For the experiments, the CR-39 track detector was obtained from Track Analysis Systems, Ltd. (Bristol, UK). The manufacturer cut the CR-39 into disks 3.7 cm in diameter that fit into the cell irradiation dishes. The CR-39 disk was placed on the Mylar bottom and irradiated with alpha particles at the same position of the cell monolayer. After the irradiation, the CR-39 was etched to enlarge the latent molecular-scale damage along the alpha-particle tracks for visual inspection under light microscopy. The chemical etching was carried out in 7 N NaOH at 90 °C for 50 minutes. Images of the etched tracks were recorded in a rectangular area using a CCD camera at 50× magnification. The image area was calibrated by using a stage micrometer at the same magnification. The track images were printed and the track numbers were scored in 20 random fields per source.

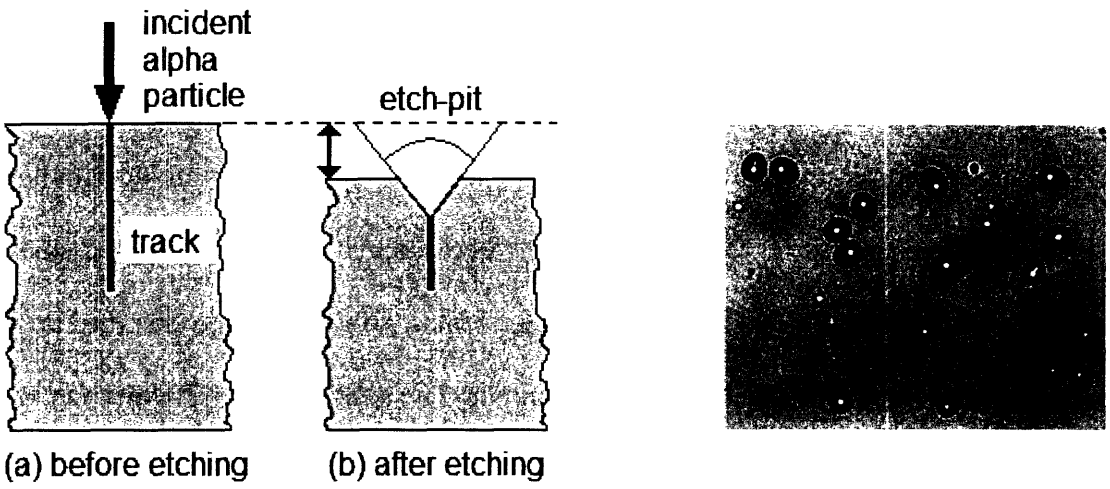

Figure 2-9. Left: Schematic etching process along alpha-particle trajectory a) the damage along the trajectory caused by the passage of the alpha particle is invisible; b) the damage zone is revealed as a cone shaped etch-pit when the surface of the CR-39 is etched in a controlled manner using a hot sodium hydroxide solution. Right: a picture of "etch pits" on CR-39. Each dot represents one alpha-particle hit.

2.2.4.4 Dose calculation

The average absorbed dose rate to the cells on the Mylar surface was calculated by multiplying alpha-particle fluence N by the stopping power S in cells, and by the appropriate conversion factors: Dose (Gy) = N×S×0.016 (12, 13), where N is the number of alpha particles hitting the monolayer of cells per μm^2; S, defined by –dE/dx, is the stopping power for tissue in $MeV \cdot cm^2/g$. The concept of stopping power is closely related to the concept of linear energy transfer (LET). The difference between these two concepts is that the LET refers to all the energy deposited in or absorbed by the material, while stopping power S refers to the energy transferred or lost from the charged particle itself. In practice, the numerical value of LET is often equal to that of S, with the exception that LET does not include the energy released due to bremmstrahlung radiation, which usually accounts for one or two percent of the total energy loss. Dose, or absorbed dose, measured

in gray (Gy), is defined as the amount of energy actually absorbed in some material. One gray is equal to one joule of energy deposited in one kg of a material. For the purpose of measuring absorbed dose in the monolayer of cells, the LET should be more appropriate than stopping power since it represents the energy that is actually deposited in that small volume. Thus we used the LET of the alpha particle in water to calculate the absorbed dose to the monolayer of cells. The factor 0.016 is a unit conversion factor. LET ($MeV \cdot cm^2/g$) × N (number of alpha particles/μm^2) results in dose unit in $MeV \cdot cm^2/g \cdot \mu m^2$.

$$\frac{MeV \cdot cm^2}{g \cdot \mu m^2} = \frac{10^6 eV \times (10^4)^2 \mu m}{10^{-3} kg \cdot \mu m^2} = \frac{10^6 \times 1.6 \times 10^{(-19)} \times 10^8 Joule}{10^{-3} kg} = 0.016 \frac{Joule}{kg} = 0.016 Gy$$

In order to get dose rate in Gy/min, we can directly apply alpha-particle flux F, which is fluence N divided by time (min), to the equation.

The dose rate from the 60 keV gamma rays released during the decay of ^{241}Am in the alpha-particle foils was measured directly above the surface of the foils using an ion chamber (Bicron). The direct measurements were in units of gamma exposure (Roentgen), which were converted to dose by assuming 1 R = 0.95 rad in tissue.

2.3 Results

2.3.1 The Simulation Results

The alpha particles hit the cells from different incident angles, leading to different path lengths through the cells and hence to different absorbed doses. A simple mathematical model was established to address the incident angle problem in order to get the overall energy spectra at the cell position. All the simulations were based on the second irradiator design, in which the # 4 alpha foil was used. The size of the # 4 foil was 7.6 cm × 7.6 cm. The vertical distance between the foil surface and the cell layer was symbolized

as h, which was fixed at 5 mm. From the information provided by the manufacturer, the energy spectrum at the # 4 foil surface peaks at 4.9 MeV with a FWHM of 58.3 keV. We assumed a single energy (4.9 MeV) emission from the foil surface in the simulation for simplicity. For each different incident angle which corresponded to a different r in figure 2-10, alpha particles produced different residual energies at the cell layer. These different residual energies formed the energy spectra that the cells received. The residual energies of alpha particles with different incident angles can be obtained from the SRIM simulation by setting the incident energy at 4.9 MeV and varying the incident angles. When the incident angle was larger than 78 degrees, the alpha particles could not penetrate the Mylar film due to long passage distance in the Mylar (Mylar density is much higher than air density). At that incident angle, r was equal to 2.35 cm.

After calculating the residual energies of the alpha particles with different incident angles, the number of alpha particles at each incident angle was also needed in order to get the overall energy spectra at the cell position. Assuming a homogeneous activity in the foil surface, the number of alpha particles hitting cells from each incident angle and resulting in specific residual energy deposition was determined by two factors: one factor was the perimeter for different radius $2\pi r$, which represents the contribution of all alpha particles from the alpha foil with the same incident angle β. However, for each source point on the perimeter, the irradiation was isotropic. So the other factor was the percentage of irradiation a cell could receive from each source point on the $2\pi r$ perimeter, which was inversely proportional to the surface area of the sphere centered at the source point with a radius d: $4\pi d^2$. From figure 2-10, $d^2 = (r^2+h^2)$. So the overall contribution from any

particular incident angle was proportional to $r/(r^2+h^2)$. For a fixed h, the value r could be obtained from the incident angle β according to the relation $\tan(\beta) = r/h$.

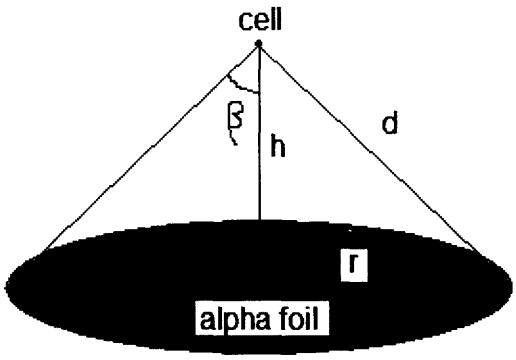

Figure 2-10. Illustrative mathematic model for a cell irradiated by alpha particles from different incident angles.

In Table 2-2, different cases with different air and Mylar thicknesses were simulated. The first column is different incident angles for the alpha particles. In the actual situation, the incident angles are continuous and range from 0 degrees (vertical) to 90 degrees (horizontal). Twelve to thirteen representative incident angles were picked for the simulation in each case. The maximum representative incident angles were obtained in the following way: a series of integral incident angles around 80 degrees were used in the simulation to determine the minimum angle at which there was no alpha particle passing through the air and the Mylar layers. The maximum representative incident angles are the minimum angles plus 1 degree. For simplicity, only the incident angles with integral values were considered. The second column is corresponding r for a chosen h and different incident angles according to the geometric relationship $r = \tan(\beta)\times h$ in figure 2-10. The h is the vertical distance between the alpha foil and the cell layer, which is equal to air distance plus Mylar distance. The third column is the relative contribution of the alpha particles at a

incident angle β (degree)	h = 2mm corresponding r (mm) r = tan(β)×h	2mm air + 4μm polypropylene relative contribution r/(r²+h²)	standardized contribution	Energy (MeV)	LET (keV/μm)
0	0	0	0	3.935	108.3
10	0.353	0.086	0.347	3.925	108.5
15	0.536	0.125	0.508	3.915	108.7
20	0.728	0.161	0.653	3.890	109.1
30	1.155	0.217	0.879	3.826	110.4
40	1.678	0.246	1.000	3.712	112.6
50	2.384	0.246	1.000	3.555	115.9
60	3.464	0.216	0.879	3.200	124.3
65	4.289	0.192	0.778	2.890	132.9
70	5.495	0.161	0.653	2.415	149.4
75	7.464	0.125	0.508	1.425	203.5
78	9.409	0.102	0.413	0.045	97.6
80	11.34	0.086	0.347	0	0
	h = 3mm	3mm air + 4μm polypropylene			
0	0	0	0	3.830	110.3
10	0.529	0.057	0.347	3.815	110.6
15	0.804	0.083	0.508	3.800	110.8
20	1.092	0.107	0.653	3.775	111.3
30	1.732	0.144	0.879	3.710	112.6
40	2.517	0.164	1.000	3.580	115.3
50	3.575	0.164	1.000	3.370	120.1
60	5.196	0.144	0.879	2.920	131.9
65	6.433	0.128	0.778	2.578	143.2
70	8.242	0.107	0.653	1.965	170.2
75	11.20	0.083	0.508	0.500	242.8
76	12.03	0.078	0.477	0.062	113
80	17.01	0.057	0.347	0	0
	h = 2mm	2mm air + 3μm polypropylene			
0	0	0	0	4.040	106.4
10	0.354	0.086	0.347	4.030	106.5
15	0.536	0.125	0.508	4.020	106.7
20	0.728	0.167	0.653	4.000	107.0
30	1.155	0.217	0.879	3.960	107.7
40	1.678	0.247	1.000	3.870	109.5
50	2.384	0.246	1.000	3.720	112.3
60	3.464	0.217	0.879	3.460	118.0
65	4.289	0.192	0.778	3.230	123.5
70	5.495	0.161	0.653	2.856	133.9
75	7.464	0.125	0.508	2.000	160.4
79	10.29	0.094	0.380	0.715	247.5
80	11.34	0.086	0.347	0	0
	h = 2mm	2mm air + 2μm polypropylene			
0	0	0	0	4.153	104.4
10	0.353	0.086	0.347	4.150	104.5
15	0.536	0.125	0.508	4.140	104.5
20	0.728	0.161	0.653	4.125	104.9

30	1.155	0.217	0.879	4.080	105.6
40	1.678	0.246	1.000	4.000	107.0
50	2.384	0.246	1.000	3.905	108.8
60	3.464	0.217	0.879	3.710	112.6
65	4.289	0.192	0.778	3.530	116.4
70	5.495	0.161	0.653	3.250	123.0
75	7.464	0.125	0.508	2.730	137.9
81	12.63	0.077	0.314	0	0
	h = 2mm	2mm air + 1.5μm Mylar			
0	0	0	0	4.157	104.4
10	0.353	0.086	0.347	4.150	104.5
15	0.536	0.125	0.508	4.140	104.5
20	0.728	0.161	0.653	4.125	104.9
30	1.155	0.217	0.879	4.080	105.6
40	1.678	0.246	1.000	4.000	107.0
50	2.384	0.246	1.000	3.905	108.8
60	3.464	0.217	0.879	3.710	112.6
65	4.289	0.192	0.778	3.530	116.4
70	5.495	0.161	0.653	3.250	123.0
75	7.464	0.125	0.508	2.550	144.2
81	12.63	0.077	0.314	0.816	244.4
	h = 3mm	3mm air + 2μm Mylar			
0	0	0	0	3.970	107.6
10	0.529	0.057	0.347	3.960	107.8
15	0.804	0.083	0.508	3.952	107.9
20	1.092	0.107	0.653	3.938	108.3
30	1.732	0.144	0.879	3.870	109.5
40	2.517	0.164	1.000	3.775	111.3
50	3.575	0.164	1.000	3.620	114.4
60	5.196	0.144	0.879	3.320	121.3
65	6.434	0.128	0.778	3.038	128.7
70	8.242	0.107	0.653	2.570	143.5
75	11.20	0.083	0.508	1.730	183.4
78	14.11	0.068	0.413	0.641	248.1

Table 2-2. Simulation Results for residual energy and LET at the cell position for different alpha-particle incident angles. The influences of different thickness of air and different thickness of polypropylene/Mylar were examined, assuming an initial incident energy of 4.9 MeV.

specific incident angle and specific residual energy. The forth column is a standardized contribution which came directly from the relative contribution in column three and divided by the maximum relative contribution value in each case. The standardized

contribution was used to facilitate plotting visualization and comparison for different cases. The fifth column is the average residual alpha-particle energy from SRIM simulations for each incident angle. It is the energy that the monolayer of cells received from the incident alpha particles. For each case, about 10^6 alpha particles were tracked. Each alpha particle produced a residual energy. The average residual energy from all alpha particles was calculated as the energy that the cells received from the alpha particles with a certain incident angle. The final column is LET value corresponding to residual energy in water.

Figure 2-11 shows graphically the relationship between the incident angle and residual energy as well as the resulting energy spectra at the cell position for various thicknesses of Mylar, polypropylene and air.

Figure 2-12 shows graphically the relationship between the incident angle and the LET, as well as the resulting LET spectra at the cell position for various thicknesses of Mylar, polypropylene and air.

Table 2-3 repeats the mathematical modeling described in Table 2-2 for the actual geometry of the alpha-particle irradiator used in all cell irradiation experiments assuming the initial incident alpha-particle energy of 4.7 MeV, which was obtained from our surface energy measurement. Figure 2-13 shows the simulated energy spectrum and LET spectrum at the cell position for the actual geometry of the irradiator. The initial alpha-particle energy from the #4 foil was 4.7 MeV. The alpha particles passed through 5 mm air and 1.4 μm Mylar before they hit the monolayer of cells.

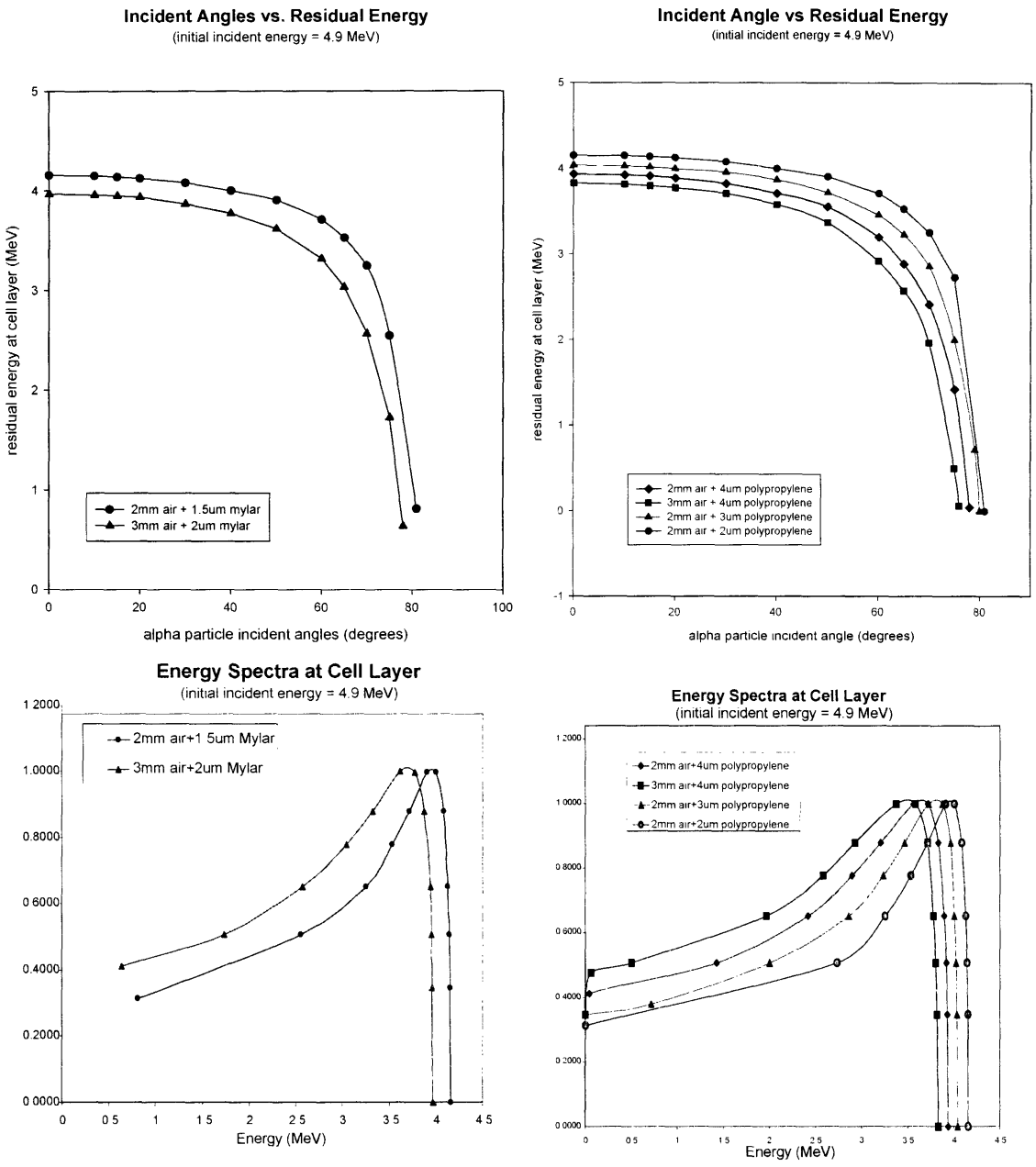

Figure 2-11. *Top:* the alpha-particle residual energies for different incident angles. The initial alpha-particle energy from the alpha foil was set at 4.9 MeV. The x-axis represents different incident angles in degrees and the y-axis represents corresponding residual energies in MeV, which are the energies that the monolayer of cells received. The left figure is for Mylar and the right figure is for polypropylene. *Bottom:* the energy spectra at the cell layer. The x-axis represents energy in MeV and the y-axis represents relative frequency, which was from the standardized contribution in Table 2-2. The left figure is for Mylar and the right figure is for polypropylene.

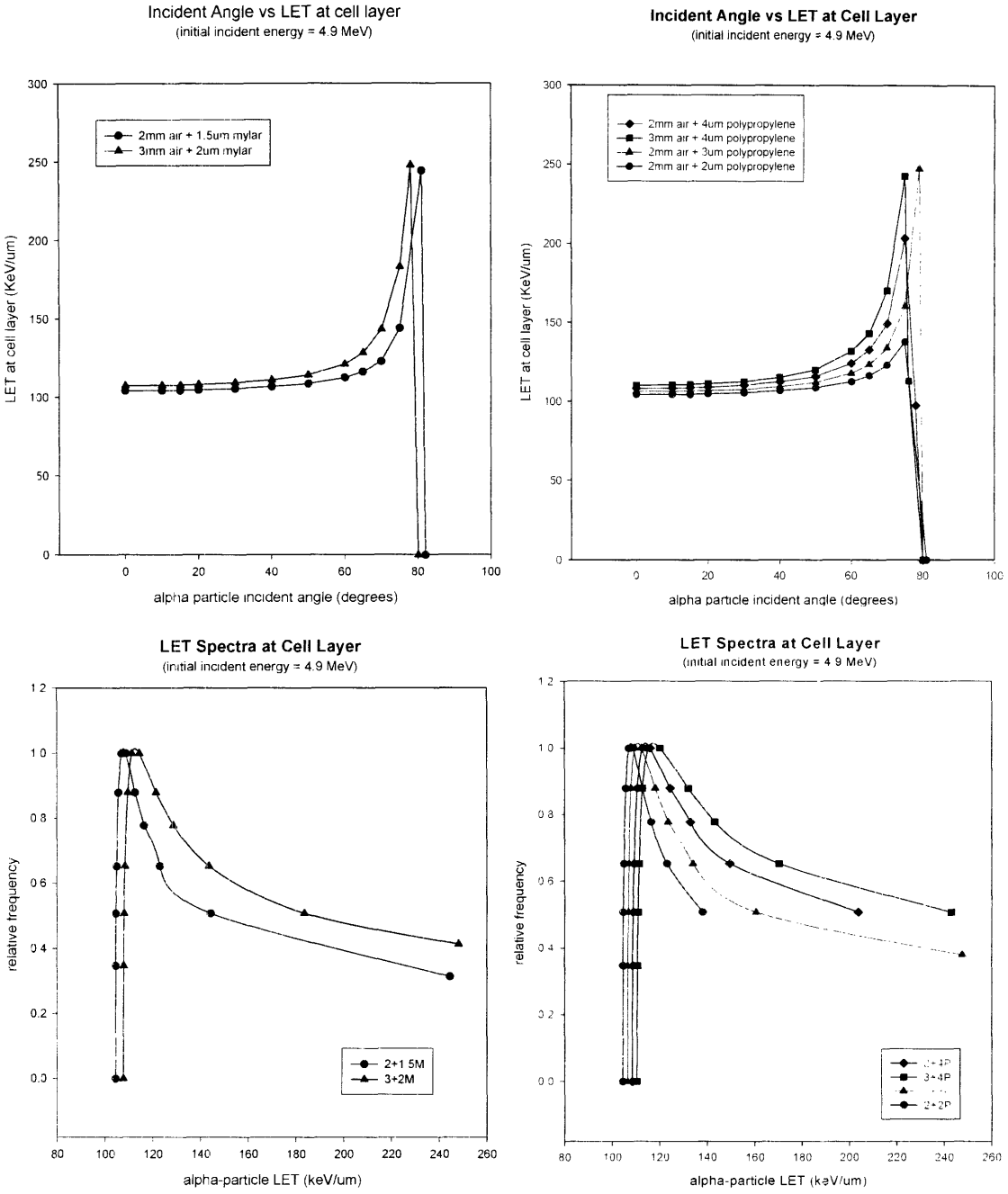

Figure 2-12. *Top:* the LET values at the cell layer for different incident angles. The x-axis represents different incident angles in degrees. The y-axis represents the corresponding LET values for the alpha particle at the cell layer. The left figure is for Mylar and the right figure is for polypropylene. *Bottom:* the LET spectra at the cell layer. The x-axis represents the alpha-particle LET in keV/μm at the cell layer. The y-axis represents the relative frequency, which came from the standardized contribution in Table 2-2. The left figure is for Mylar and the right figure is for polypropylene.

	h = 5 mm	5mm air + 1.4μm Mylar		
Incident angle β (degree)	corresponding r (mm) $r = \tan(\beta) \times h$	relative contribution $r/(r^2+h^2)$	Residual Energy (MeV)	LET (keV/μm)
0	0	0	4.203	100.0
10	0.882	0.034	4.192	100.2
15	1.340	0.050	4.176	100.4
20	1.820	0.064	4.157	100.8
30	2.887	0.087	4.093	101.8
40	4.195	0.098	3.986	103.7
50	5.959	0.098	3.797	107.2
60	8.660	0.087	3.449	114.5
65	10.72	0.077	3.154	121.5
70	13.74	0.064	2.662	135.9
75	18.66	0.050	1.736	176.2
76	20.05	0.047	1.256	204.9
77	21.66	0.044	0.800	226.0
78	23.52	0.041	0.244	173.4

Table 2-3. The simulation results for residual energies and LET at the cell position for different incident angles in the second design of alpha-particle irradiator, assuming the initial incident energy of the alpha particle was 4.7 MeV; the alpha particles passed through 5 mm air and 1.4 μm Mylar film before they hit the monolayer of cells grown on the Mylar bottom.

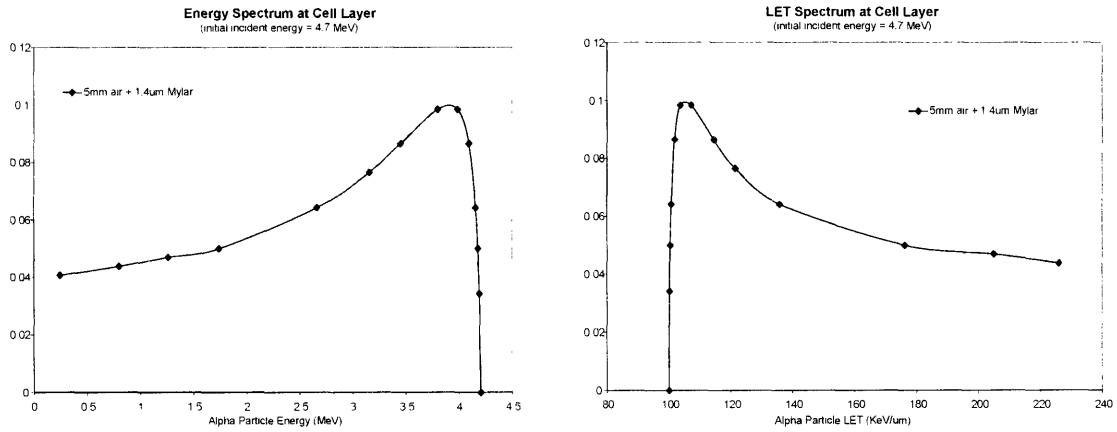

Figure 2-13. Simulated energy spectrum (left) and LET spectrum (right) at the cell position for the actual irradiator geometry described in 2.2.2.2 (the second design of the irradiator), which was used in all following cell irradiation experiments. For the energy spectrum, the x-axis represents the alpha-particle residual energies at the cell position in MeV. The y-axis represents the relative frequency of different energies, which came from the relative contribution in Table 2-3. For the LET spectrum, the x-axis represents the alpha-particle LET at the cell position in keV/μm. The y-axis represents the relative frequency of different energies, which came from the relative contribution in Table 2-3.

2.3.2 Measurements

2.3.2.1 Alpha-particle energy and LET spectra at the cell irradiation position

The measured energy spectra of the ^{241}Am alpha particles under several different conditions are shown in figure 2-14. The sharp peak at 5.49 MeV is the ^{241}Am calibration source measured in a vacuum. The FWHM of the ^{241}Am calibration peak is 0.028 MeV. The broader peak with a relative frequency maximum at ~ 4.7 MeV is the energy spectrum obtained with the PIPS detector directly above the ^{241}Am foil # 4 (see Table 2-1). The peak with a relative frequency maximum at 3.95 MeV was obtained with the PIPS detector positioned inside the cell irradiation dish directly above the 1.4 μm-thick Mylar bottom of the cell culture dish, positioned in the irradiator above foil #4. The E_{max} is progressively attenuated and the peak is broadened due to the energy straggling of the alpha particles through the gold surface coating of the source, 5 mm of air and then the 1.4 μm of Mylar. Due to the un-collimated nature of this planar source, the energy spectrum is skewed with a tail at lower energies. The PIPS detector was used with the 0.8 mm diameter pinhole to measure the alpha-particle flux at the cell position: inside the cell irradiation dish, directly above the Mylar membrane. The pinhole method was tested on the # 3 foil first and the result is shown in figure 2-15. If the pinhole caused a significant collimation effect, it would differentiate the two spectra (with and without pinhole) at lower energies. From the result shown in figure 2-15, it is clear that the two spectra overlap each other, which means that the collimation effect caused by the pinhole was minimal.

The PIPS detector was also used to measure the alpha-particle flux with the 0.8 mm diameter pinhole. The obtained count rate was 998 α-particles/mm^2/s. The reproducibility error of the system was 2 %. So the count rate with error was 998 ± 20 α-particles/mm^2/s.

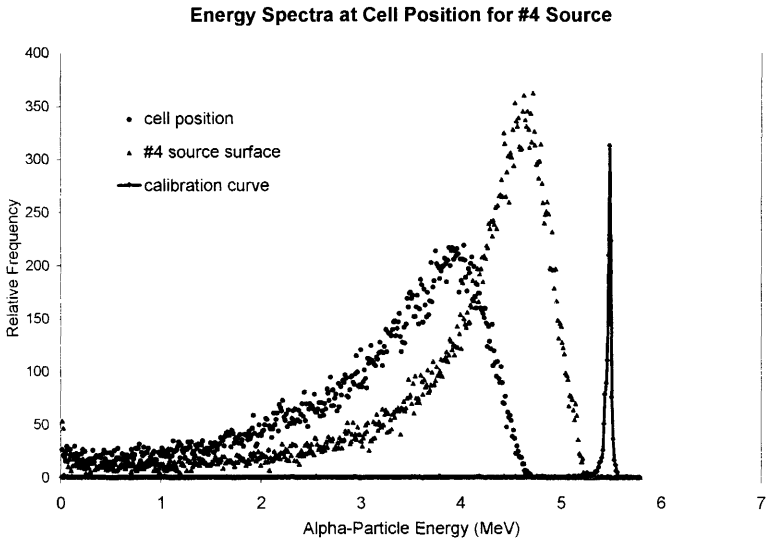

Figure 2-14. Energy spectra measured with the solid state (PIPS) detector at various positions above the alpha-particle source used for all of the cell irradiations (^{241}Am foil #4: nominal activity, 10 μCi ^{241}Am/cm^2). Triangles: measurement directly above the gold surface of the bare foil. Circles: measurement at the cell irradiation position, inside the cell culture dish directly above the Mylar membrane. Filled circles: a ^{241}Am point source measured in a vacuum. The ^{241}Am energy peak at 5.49 MeV was used to calibrate the multi-channel analyzer; the FWHM of the calibration peak was 0.028 MeV.

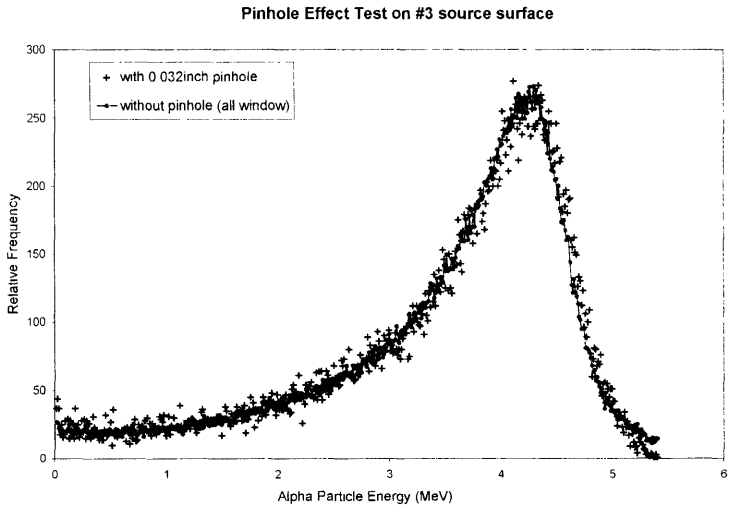

Figure 2-15. Energy spectra with and without the pinhole tested on the # 3 alpha source surface. The two spectra overlap each other, suggesting no significant collimation effect from the pinhole.

For the #4 alpha source, the average energy to the monolayer of cells was calculated as a weighted average energy for all energy channels with the weighting factor being the number of alpha-particle counts per energy channel. The average energy was 3.14 MeV. The reproducibility of the measuring system was estimated to be 2%. So the error on the average energy was 0.06 MeV. The energy spectrum of the alpha particles at the cell irradiation position was converted to an LET spectrum by a point-by-point interpolation using published stopping power and range tables from the National Institute of Standards and Technology database. As an alpha particle travels through a medium and continuously loses its energy, its energy deposition demonstrates a peak near the end of the alpha particle range, which is called the Bragg peak. Figure 2-16 shows the relationship between the energy and the LET of the alpha particles due to the Bragg peak effect. The maximum LET was 227 keV/μm, corresponding to the energy of 0.73 MeV. From figure 2-16, two different alpha-particle energies on either side of the peak may have the same LET value. For example, both 0.17 MeV and 2.33 MeV correspond to the same LET of 148 keV/μm. The final LET spectrum was obtained by adding the counts of each LET value on the lower energy side to the counts of the same LET value on the higher energy side of the Bragg peak. The resulting LET spectrum is shown in figure 2-17. The weighted-average LET was calculated from the LET spectrum using the alpha-particle counts per channel as the weighting factor. The average LET of the alpha particles at the cell irradiation position was 127 keV/μm. The uncertainty in stopping power depends on the energy of the particle and the material composition. It's estimated to be 5% (14). So the average LET with error was (127 ± 6) keV/μm.

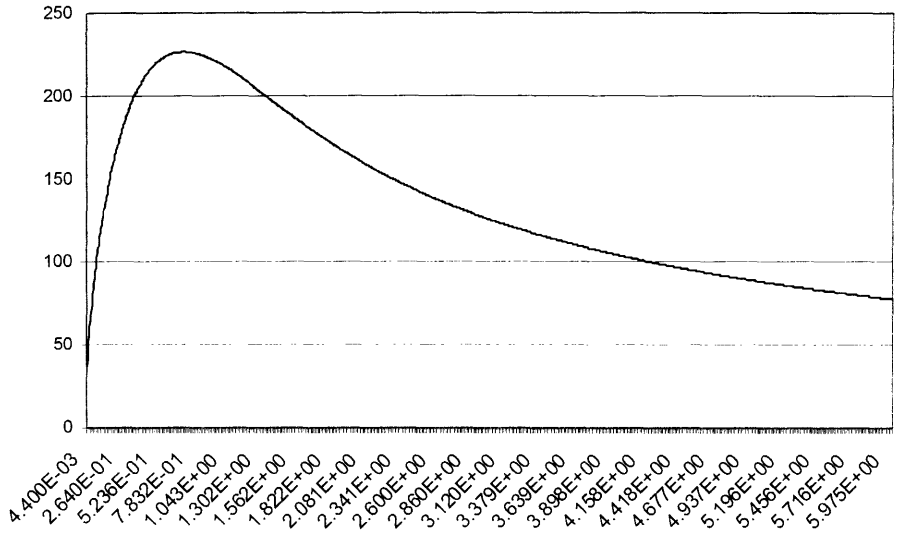

Figure 2-16. The relationship between the energy (x-axis, MeV) and the LET (y-axis, keV/μm) of alpha particles due to a Bragg peak effect. The maximum LET is 227 keV/μm, corresponding to the energy of 0.73 MeV.

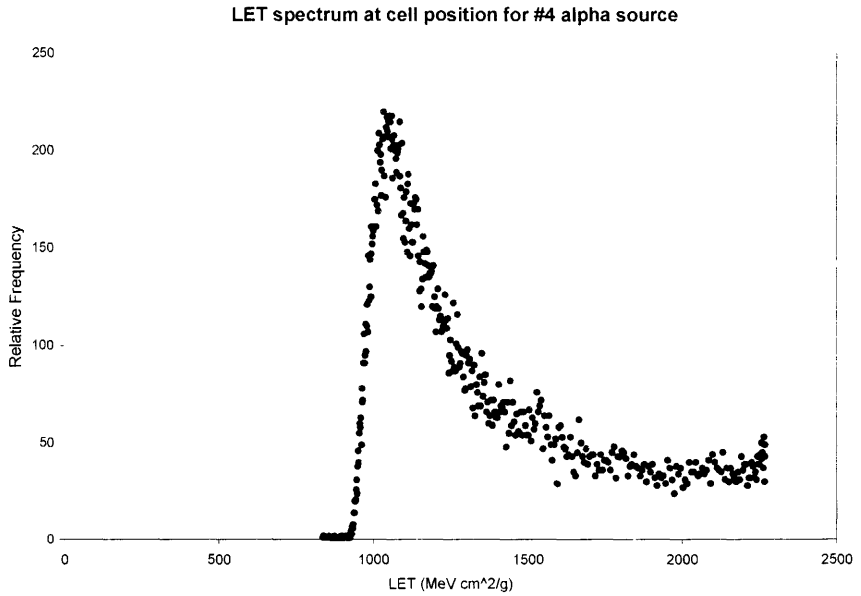

Figure 2-17. LET spectrum at the cell irradiation position, calculated from the measured energy spectrum of the # 4 alpha source shown in figure 2-14.

2.3.2.2 Alpha-particle fluence and uniformity measurements with CR-39

The CR-39 plastic track detectors were placed inside the cell irradiation dish directly on the Mylar membrane. The #4 alpha-particle source has a relatively high activity. In order to avoid track overlap and saturation on the CR-39 track detector, 0.2 s exposures were used for this high-activity source. Counts from 20 random fields (1.03 mm × 1.03 mm) indicated 306 ± 15 particles for the 0.2 s exposures, corresponding to an alpha-particle flux of (1440 ± 70) counts /mm^2/sec at the cell irradiation position. This value is considerably higher than the value (998 ± 20) particles/mm^2/sec obtained with the PIPS detector for the same #4 alpha-particle source using a 0.8 mm diameter pinhole. A possible explanation is that there was a short shutter opening and closing time. With such a short irradiation time (0.2 s), the shutter opening/closing time became critical and brought a large error to the result. When the CR-39 track detectors were used with a lower activity alpha source (^{241}Am foil #2, Table 2-1) so that a longer exposure time was used for recording, the CR-39 results were in much closer agreement with the PIPS detector. CR-39 exposures in 15-second increments from 15 to 105 seconds produced a linear response, as shown in figure 2-18 (R^2= 0.998); scoring 20 random fields per CR-39 exposure resulted in a variance of approximately 10% at each dose level. The CR-39-determined alpha-particle flux from all 7 exposure times for the #2 ^{241}Am foil was 9.9 ± 0.8 tracks/mm^2/s (n=140). The PIPS detector produced a reading of 11.2 ± 0.2 tracks/mm^2/s in the same location, which is slightly higher than the CR-39 average. For the track-etch detector, not all the alpha particles traveling into the CR-39 are detected: the detection efficiency depends on the particle energy, charge and incident angle (11). For example, alpha particles with big incident angles ($\beta \geq \pi/2 - \theta_{lim}$) would not form etch-pits (figure 2-19), which leads to an

underestimate. These explain why the CR-39 results were 11% lower than the PIPS results. Similar relationship was obtained by Neti *et al.*: the PIPS measurements were 6%, 19% and 22% higher than the CR-39 averages for their three ^{241}Am alpha sources. They concluded that the fluences obtained with the PIPS detector had a much higher degree of accuracy and precision than the CR-39 measurements (8). Therefore, the PIPS results was considered more reliable and has been used in the calculation of the #4 alpha source dose rate to the cell monolayers.

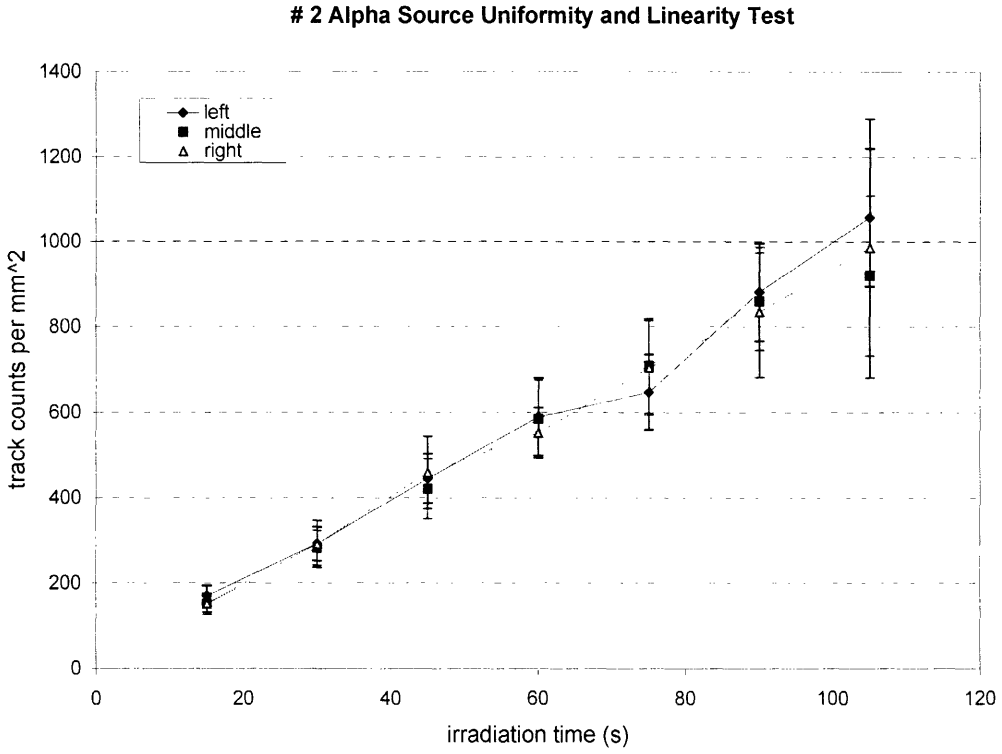

Figure 2-18. The CR-39 track detector results (tracks/mm^2) for the alpha-particle flux, uniformity and linearity on the #2 alpha foil. Left, middle and right denote the positions of the three holes shown in figure 2-3. Irradiations were in 15-second increments from 15 to 105 seconds. For each time point, 20 random fields were scored. The average values and standard deviations from the 20 counts were calculated and shown in the graph.

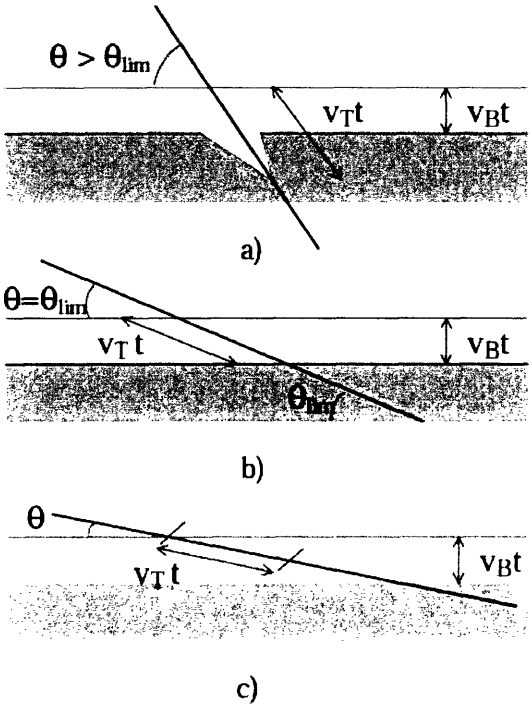

Figure 2-19. The track formation for different incident angles β ($\theta = \pi/2 - \beta$). (a) when $\theta > \theta_{lim}$ the etch-pit is formed; (b) (c) when $\theta \leq \theta_{lim}$, no etch-pit is formed. V_B is the bulk or material etching rate and V_T is the track etching rate. The limit angle θ_{lim} is decided by $\sin(\theta_{lim}) = V_B / V_T$ (11).

Figure 2-20 shows a superimposed image of DU-145 human prostate carcinoma cells and CR-39 pits at the same magnification of 50×. The DU-145 cells were grown on a glass slide until confluent. Then the slide was stained with methylene blue solution and pictured by an epi-fluorescent microscope. The CR-39 track etch image was from a 0.2 second exposure using the #4 alpha source at the cell position. The CR-39 picture was superimposed on the confluent DU-145 cell image using Photoshop.

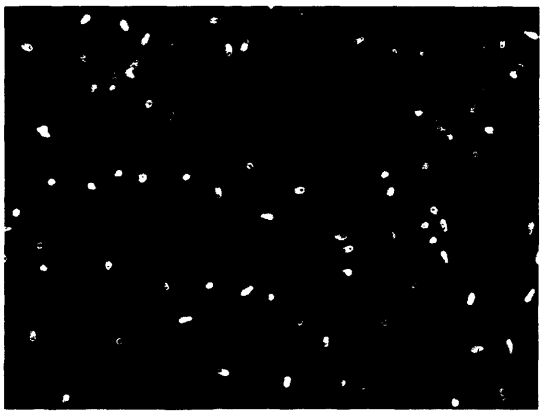

Figure 2-20. Superimposed image of DU-145 human prostate carcinoma cells and CR-39 pits after 0.2 second exposure of the #4 alpha source. Magnifications for both images were 50×.

2.3.2.3 Dose rate calculation

The dose rate was calculated from the equation: Dose Rate (Gy/min) = F×S×0.016. The average LET was 127 ± 6 keV/μm and the average track density was 998 ± 20 counts/mm^2·s. The percentage of error to the dose rate was calculated to be 5.4%. The average dose rate to the cell monolayers on the Mylar dish bottom was calculated to be 1.2 ± 0.06 Gy/min.

2.3.2.4 Surface dosimetry of the five alpha-particle foils

Figure 2-21 shows the surface energy spectra for all five alpha foils. Table 2-4 shows the measured and calculated characteristics of the five ^{241}Am alpha-particle foils. The nominal activity concentration of ^{241}Am included in each foil during manufacture ranges from 0.01 μCi/cm^2 for foil #1 and increases by a factor of 10 for each foil up to a maximum of 100 μCi/cm^2 for foil #5. The energy spectra and the total alpha-particle flux per unit area were measured with the PIPS detector. The variations observed in Table 2-4 for the average energy of the foils was most likely due to slight variations in the thickness

of the gold coating on the surface of the foil from the manufacturing process. The average dose rates were calculated from the measured alpha-particle fluxes and the average LET values for each foil. The gamma doses measured at the foil surface were negligible compared to the alpha-particle doses (see Table 2-4). Foil #4 was used for all the cell irradiation experiments in this study.

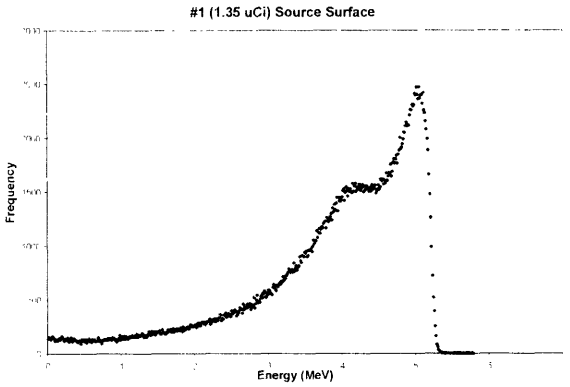

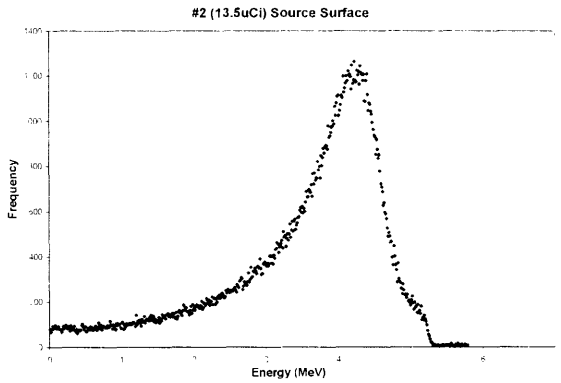

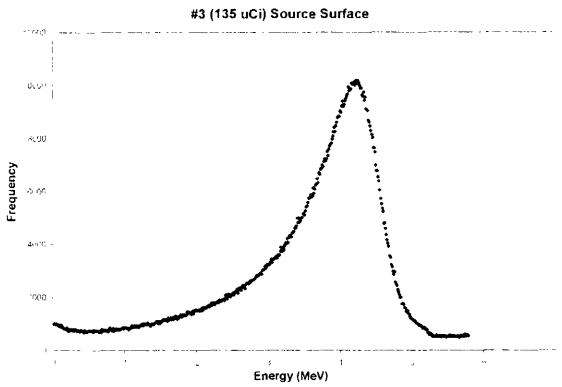

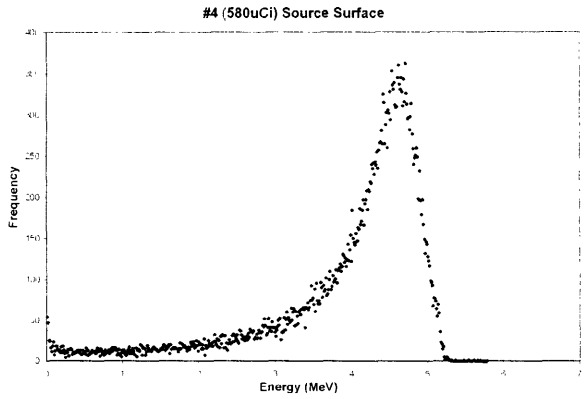

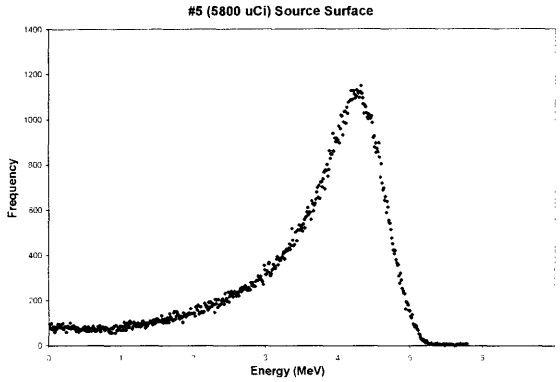

Figure 2-21. Energy spectra at the surface of the five alpha foils. All spectra peak between 4-5 MeV and have skewed tails in the low-energy part due to the non-collimated sources. All alpha foils should have the same energy spectra if they were manufactured to exactly the same specifications since the activities do not affect the energies. The differences in the spectra shown here for the five alpha foils most likely come from variations in the manufacturing process (homogeneity of the radioisotope layer or the thickness of the gold layers). Especially for the #1 alpha foil, there is a second peak at about 4 MeV, which may come from an impurity of the radioisotope.

Alpha foil #	Average Energy (MeV)	Average LET (keV/μm)	Average Alpha-particle Flux (counts/mm^2/s)	Alpha Dose Rate (Gy/min)	Gamma exposure Rate (mR/h) R: Roentgen	Gamma Dose Rate (Gy/min)
#1	3.89	110.6	3.16	0.003	nd[1]	nd[1]
#2	3.54	117.6	12.90	0.015	0.2	3×10^{-8}
#3	3.50	118.4	106.72	0.12	2.5	4×10^{-7}
#4	3.98	107.4	1162.05	1.17	27	4.3×10^{-6}
#5	3.56	116.9	12430.2	13.9	290	4.6×10^{-5}

nd: not detectable

Table 2-4. Surface dosimetry for the five ^{241}Am foils. Alpha-particle energy and flux measurements were made with the PIPS detector directly over the bare foil surfaces. The errors of the results are not shown in this table. The percentage errors for the alpha dose rates were estimated to be 5.4% for all five foils.

2.3.2.5 The application of #5 alpha-particle source in another project (15)

The highest activity # 5 source was used in another project "Differential Oxidation of Deoxyribose in DNA by γ- and α-Radiation" by Christiane Collins from Prof. Peter C. Dedon's group in the Biological Engineering Division at MIT. This project was looking at the chemical mechanisms of how radiation causes DNA single strand breaks and whether radiations with different LET properties (low-LET gamma vs. high-LET alpha particles) cause single strand breaks by different mechanisms. The Dedon Lab has developed analytical techniques to measure the deoxyribose oxidation of the DNA that are characteristic of radical attack at specific positions on the deoxyribose. For the experiments with the #5 alpha-particle source, the amount of a fragment known as phosphoglycolaldehyde (PGA) was used to compare the different radiations. Specifically, a recently developed gas chromatography/negative chemical ionization mass spectrometry method was used to quantify PGA residues in purified DNA and in human TK6 lymphoblastoid cells subjected to γ-radiation (^{60}Co) and α-particles (^{241}Am). The α-particle irradiations were done in our lab. Since very high alpha-particle doses were required in order to produce enough PGA for quantitative analysis by the mass spectrometry technique, the #5 source was chosen to deliver the α-radiation to the 1 ml DNA solutions, which were contained in the cell irradiation dishes with replaceable 3.7 μm polypropylene bottom. The depth of 1 ml DNA solution is ~830 μm in the irradiation dish with a 3.81 cm diameter. The residual range in water of α-particles coming through the 3.7 μm polypropylene is ~25 μm (16). In order to deliver a homogeneous dose to all the DNA in the 1 ml volume, a magnetic stirring system was used. The Mylar dish was placed 1 mm above the #5 alpha foil, which was placed upon a magnetic stirrer. A specially designed

stir bar (by Christiane Collins) was place inside the 1 ml DNA solution. DNA solutions were exposed to α-radiation for 0 to 240 min at ambient temperature with rapid stirring.

For the dosimetry, the PIPS detector was used to measure the energy spectrum directly above the 3.7 μm polypropylene bottom of the cell irradiation dish. The energy spectrum is shown in figure 2-22. From the measured spectrum, the average energy was calculated to be 3.12 MeV. The alpha-particle flux above the polypropylene was measured to be 9882 particles/mm²/s. The diameter of the dish was 3.81 cm and the area of the dish was $\pi\ (3.81/2)^2 = 11.4\ cm^2$. Since the depth of the DNA solution was much larger than the ranges of the alpha particles in water, all the residual energy of the incident alpha particles would be deposited in the 1 ml volume. The total energy deposited per unit time is: (3.12 MeV) × (9882 particles /mm²/s) × (11.4 × 100 mm²) = 3.515×10^7 MeV/s, which was converted into Joules: 3.515×10^7 (MeV/s) × 1.6×10^{-19} (Joule/eV) × 10^6 (eV/MeV) = 5.6×10^{-6} (J/s).

Assuming that the density of the DNA mixture was 1 g/cm^3, for a total volume of 1 ml, the total mass would be 1g. Since dose is the energy deposited per unit mass, the dose rate to the DNA was calculated as:

$$\frac{5.6\times10^{-6}\,J/s}{1\times10^{-3}\,kg} = 5.6\times10^{-3}\,J/kg\cdot s = 5.6\times10^{-3}\,Gy/s = 5.6\times10^{-3}\times60Gy/\min = 0.34Gy/\min$$

And the error to this dose rate was estimated to be 0.018 Gy/min.

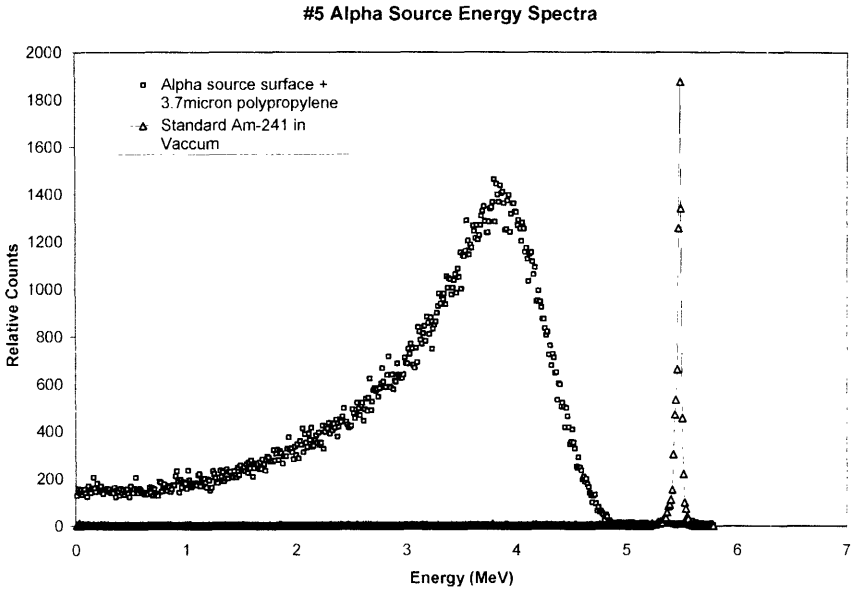

Figure 2-22. Energy spectra of the bare ^{241}Am calibration source in vacuum (Δ) and the #5 ^{241}Am foil above the polypropylene in the cell dish (□).

2.4 Discussion

In this chapter, a cell irradiation system based on an isotopic alpha-particle emitter ^{241}Am is described. ^{241}Am has a half-life of 232.2 years and emits alpha particles with three main branches of energies that are close enough to make the source essentially monoenergetic: 5.485, 5.433, and 5.388 MeV (relative abundances 84.5, 13.0, and 1.6% respectively). The average energy of approximately 5.48 MeV is similar to the energies of alpha-emitting isotopes used in radioimmunotherapy: e.g., ^{211}At, 5.87 MeV; ^{212}Bi, 6.05 MeV. Compared to the Pu-238 alpha-particle irradiator of Noelle F. Metting, Hatsumi Nagasawa and John B. Little (7) and the Am-241 multi-port alpha-particle irradiator of Neti and Roger Howell (8), the source designed for the studies reported here has been simplified considerably. Our irradiator does not have the collimator system, the beam delimiter, rotation of the source or rotation of the collimator. Would these differences

cause problems for the cell irradiations planned here? What is the advantage of our simple irradiator?

For the alpha-particle irradiators described in the literature (7, 8), the collimator, the delimiter and the rotation system are all intended to produce a more homogeneous irradiation of the cells: the collimator will eliminate the alpha particles with shallow incident angles and should produce a narrower energy spectrum without a low-energy tail (see figure 2-23). The beam delimiter was described as substantially improving the uniformity of the beam, particularly at the edges of the growth surface (7). The rotation systems for both the source and the collimator were intended to average out any "hot-spots" or "cold-spots" on the alpha-particle sources and to provide more uniform irradiation to the cells. With all these parts built into the irradiation systems, the gap between the alpha source and the dish bottom was large (48 mm (7) and 51 mm (8)). Both designs used helium gas to minimize the alpha-particle energy loss because air attenuates the alpha-particle energy more than helium gas (air contains heavier elements like O and N). As a result, the alpha particles would travel through 42 mm helium gas (in Metting's design) (7) or 45 mm helium gas (in Neti's design) (8), 1.5 μm Mylar (the exit window), 6 mm air and the 1.5 μm Mylar dish bottom to reach the cell layer. In our design, the alpha particles only needed to travel through 5 mm air and 1.4 μm Mylar dish bottom before they hit the cell layer.

The simple design is in keeping with the experimental objective of these studies: the focus is on the bystander cells growing on an insert, the bottom layer of cells receive a distribution of alpha-particle energies and LETs that is more reflective of the actual situation during targeted alpha-particle therapy of solid tumors. We have used an

uncollimated planar source to irradiate a monolayer of tumor cells growing on a Mylar film. As a result, alpha particles entering the cell layer at shallow angles will have a broader distribution of energies, LET values and residual ranges compared to a monoenergetic microbeam source, or to collimated accelerator or planar isotopic sources.

For radiobiological studies on the effects of alpha particles, it is desirable to use well-defined exposure conditions where the angle of the particle trajectory through the cell, and the residual range (energy) of the particle at the cell surface are known (and ideally controlled to a narrow range). It is only the well-collimated accelerator-based alpha-particle beams and the accelerator-based microbeams that can approach this ideal situation and carry out cell irradiations in "track mode", where the change in LET is small over the dimensions of the cellular target. With the planar isotopic sources that have been described in the literature (7), there is always beam broadening and energy straggling due to the exit window, the Mylar cell support membrane, the distance of air or other gas traversed by the alpha particles, even when honeycomb collimators are built into the design of the irradiators. For example, using a planar ^{239}Pu source electroplated onto stainless steel, Inkret et al, reported a mean energy of 3.23 MeV (^{239}Pu emits 3 alpha particles at 5.35, 5.45 and 5.50 MeV), an energy-weighted stopping power of 123 keV/μm, and a cell surface dose rate of 2.2 Gy/min (17). Nasgasawa and Little also used a collimated ^{239}Pu source for the initial description of the bystander effect (7, 12). The energy of the alpha particles coming through the Mylar cell growth membrane was estimated to be 3.65 MeV by particle range experiments with increasing thicknesses of air or Mylar. This alpha-particle energy corresponds to an LET of 112 keV/μm (7). No spectra or range of values were provided, but the alpha particles were certainly not monoenergetic as can be inferred

by the broad shoulder on the particle flux vs absorber thickness plots (7). Neti *et al.* have used a planar ^{241}Am source in a collimated geometry similar to that described by Metting *et al.* The maximum energy for that irradiator was 2.9 MeV: the energy-weighted average LET was 132 keV/μm (range: 70-200 keV/μm) (8).

We have used planar ^{241}Am sources from the same manufacturer as Howell (8) (but different activity concentrations). Interestingly, for the uncollimated irradiator described here the alpha-particle characteristics are not that different from those reported for collimated planar sources. For the ^{241}Am cell irradiator described here the peak alpha-particle energy was 3.9 MeV. The corresponding LET spectrum calculated from the measured energy spectrum showed a maximum at 100 keV/μm (range: ~ 70 – 220 keV/μm) and an energy-weighted average stopping power of 128 keV/μm.

The lower E_{max} (3.9 MeV) and broad tail at lower energies compared to the ^{241}Am calibration source represents the energy straggling of the α-particles following passage through 1 to 1.5 μm of gold, 5 mm of air and 1.4 μm of Mylar. The maximum residual range in water of 3.9 MeV α-particles is ~30 μm (16). Alpha particles that traverse the gold, air and Mylar at shallow angles will have a low residual energy, a short residual range, and a correspondingly high LET. This is reflected in the tails at low energy and high LET evident in figures 2-14 and figure 2-17. The average dose rate delivered to the cells on the Mylar membrane inside the cell dish (within the 25 μm range of the α-particles) was calculated by assuming that the average dose rate was the product of the average LET (1266 MeV cm^2 g^{-1}) and the average track density (998 tracks mm^{-2} s^{-1}). Thus, the average dose rate using the #4 source at the cell irradiation position on the Mylar surface was 1.2 Gy/min.

The main purpose of this project is to study the bystander effect as well as its synergy with anti-cancer drugs in tumor cells. With targeted alpha therapies for solid tumors or micrometastatic disease, the non-uniform delivery of MAbs bearing alpha emitting radionuclides, or ^{10}B containing drugs used for boron neutron capture therapy results in a non-uniform delivery of alpha particles to the tumor site. The bystander cells are the ones that escape direct alpha-particle traversals. The 3-D tumor site is exposed to alpha particles of all energies, residual ranges and LETs ranging down from the original emitted properties. Thus our simplified alpha-particle irradiator design mimics the real clinical situation of radioimmunotheray.

In addition, our simple and portable design of alpha-particle irradiator makes some other research applications possible. The small irradiator could be put inside an X-ray machine to study the combined effects between high-LET and low-LET irradiations, (ie, additive or synergetic). The irradiator could also be placed into a refrigerator or an incubator to deliver radiation to cells at different temperatures to study the effect on DNA repair or the temperature dependence of bystander signal generation. The irradiator can be easily and safely carried to another location to conduct experiments in other facilities or labs.

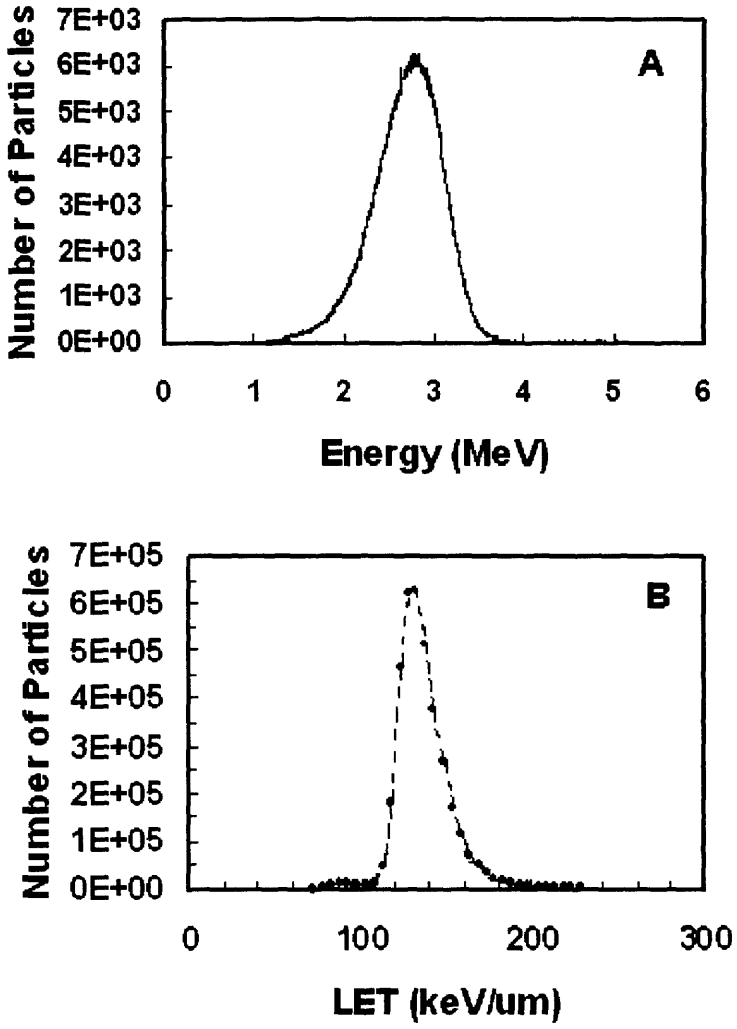

Figure 2-23. The energy spectrum and LET spectrum for the 241Am irradiator described in reference (8). They have less low-energy and high-LET tails than the spectra of the uncollimated alpha source shown in figure 2-14 and figure 2-17, which is due to the cut-off of the shallow-incident-angle alpha particles by the collimator.

References:

1. Hall, E. J. Radiobiology for the radiologist, 5th edition, p. 553. Philadelphia: Lippincott Williams & Wilkins, 2000.
2. G. Randers-Pehrson, C. R. G., G. Johnson, C. D. Elliston and D. J. Brenner The Columbia University single-ion microbeam. Radiation Research 210-214, 2001.
3. Jostes RF, H. T., James AC, Cross FT, Schwartz JL, Rotmensch J, Atcher RW, Evans HH, Mencl J, Bakale G, et al. In vitro exposure of mammalian cells to radon: dosimetric considerations. Radiat Res., *127:* 211-219, 1991.
4. Macklis, R., Kinsey, B., Kassis, A., Ferrara, J., Atcher, R., Hines, J., Coleman, C., Adelstein, S., and Burakoff, S. Radioimmunotherapy with alpha-particle-emitting immunoconjugates. Science, *240:* 1024-1026, 1988.
5. Macklis, R., Kaplan, W., Ferrara, J., Atcher, R., Hines, J., Burakoff, S., and Coleman, C. Alpha particle radio-immunotherapy: animal models and clinical prospects. Int J Radiat Oncol Biol Phys, *16:* 1377-1387, 1989.
6. Metting, N., Palayoor, S., Macklis, R., Atcher, R., Liber, H., and Little, J. Induction of mutations by bismuth-212 alpha particles at two genetic loci in human B-lymphoblasts. Radiat Res, *132:* 339-345, 1992.
7. Metting, N. F., Koehler, A. M., Nagasawa, H., Nelson, J. M., and Little, J. B. Design of a benchtop alpha particle irradiator. Health Phys, *68:* 710-715, 1995.
8. Neti, P. V., de Toledo, S. M., Perumal, V., Azzam, E. I., and Howell, R. W. A multi-port low-fluence alpha-particle irradiator: fabrication, testing and benchmark radiobiological studies. Radiat Res, *161:* 732-738, 2004.
9. J. F. Ziegler, J. P. B. a. U. L. The Stopping and Range of Ions in Solids. Pergamon Press, New York, 1985.
10. Cartwright, B. J., Shirk, E. K., and Price, P. B. A nuclear-track-recording polymer of unique sensitivity and resolution. Nucl. Inst. and Meth., *153:* 457-460, 1978.
11. Enge, W. Introduction to plastic nuclear track detectors. Nuclear Tracks, *4:* 283-308, 1980.
12. Nagasawa, H. and Little, J. B. Induction of sister chromatid exchanges by extremely low doses of alpha-particles. Cancer Res, *52:* 6394-6396, 1992.
13. Raju, M. R., Eisen, Y., Carpenter, S., and Inkret, W. C. Radiobiology of alpha particles. III. Cell inactivation by alpha-particle traversals of the cell nucleus. Radiat Res, *128:* 204-209, 1991.
14. ICRU Stopping Powers and Ranges for Protons and Alpha Particles. International Commission on Radiation Units and Measurements, *ICRU Report 49*, 1993.
15. Christiane Collins, X. Z., Rong Wang, Marita C. Barth, Tao Jiang, Jeffrey A. and Coderre, a. P. C. D. Differential Oxidation of Deoxyribose in DNA by ã- and á-Radiation. Radiation Research, 2005.
16. Ziegler, J. F. Comments on ICRU report no. 49: stopping powers and ranges for protons and alpha particles. Radiat Res, *152:* 219-222, 1999.
17. Inkret, W. C., Eisen, Y., Harvey, W. F., Koehler, A. M., and Raju, M. R. Radiobiology of alpha particles. I. Exposure system and dosimetry. Radiat Res, *123:* 304-310, 1990.

Chapter 3 Direct Alpha-Particle Irradiation

3.1 Introduction

The interaction of radiation with matter results in physical, chemical and biological changes. The transfer of energy from radiation to biologic material leads to ionization or excitation of its atoms or molecules. In the case of ionization, radiation with sufficient energy (>33.9 eV in dry air) ejects one or more orbital electrons from an atom or molecule and produces an ion pair. Ion pairs themselves can interact with surrounding matter producing more ion pairs or secondary ionization. This radiation is called ionizing radiation. If the energy transferred is not sufficient to cause ionization, excitation happens, in which an orbital electron is raised to a higher energy level. Electrons in an excited state may form or break molecular bonds or simply go back to their original energy level by emission of electromagnetic radiation. There are two basic types of interactions between radiation and biologic material: direct and indirect interactions. In direct interaction, the energy of the radiation is deposited directly in critical biologic targets resulting in excitation or ionization. Direct effects are the dominant process in the case of high-LET radiations, such as neutrons and alpha-particle irradiations. Alternatively, the radiation may interact with other atoms or molecules around the critical biologic targets, mostly water, to produce free radicals that are able to diffuse far enough to reach and damage the critical targets. This is called the indirect interaction of radiation. A radical is a free atom or molecule carrying an unpaired orbital electron in the outer shell, which is associated with a high degree of chemical reactivity. Free radicals like hydroxyl radicals (·OH) are very reactive and will react with any nearby molecule. If the ·OH reacts with DNA, a variety of lesions such as adducts can be formed.

Radiations of different qualities have different degrees of effectiveness in producing biological effects. The amount of radiation energy absorbed per unit mass of biologic material is measured by absorbed dose. The SI unit of absorbed dose is joule per kilogram (J/kg), which is defined as the gray (Gy). Equal doses of different types of radiation do not produce equal biologic effects. High-LET radiations produce much denser ionizations along the tracks than low-LET radiations. These differences in density of ionizations are a major reason that neutrons, protons, and alpha particles produce more biological effects per unit of absorbed radiation dose than do more sparsely ionizing radiations such as x rays, gamma rays, or electrons. Analysis of the relative biologic effectiveness (RBE) is a useful way to compare the effects of different radiations. The relative biological effectiveness for a given test radiation is defined by the ratio D_{250}/D_T , where D_{250} and D_T are, respectively, the dose of a reference radiation, usually 250-kV x-rays, and the test radiation required to produce the same biological effect (1).

Many scientific investigations have been conducted to determine the critical irradiation targets for the cells and the corresponding irradiation properties of the targets. By employing a polonium tipped microneedle as a microbeam source to selectively irradiate the nucleus or the cytoplasm of the cell with alpha particles, Munro et al. reported that irradiation of the cytoplasm did not cause a decrease in cell growth, whereas much lower doses of alpha particles targeted to cell nuclei were frankly lethal (2). Other investigators have used radioactive compounds that preferentially localize in the cell nucleus, the plasma membrane, or the cytoplasm, and have observed that the irradiation of the extranuclear region of a cell is far less effective than irradiation of the cell nucleus (3, 4). Those experiments showed that although some minor effects could be induced after

irradiating the cytoplasm, a cell's nucleus and particularly genomic DNA is the critical target for the biologic effects of ionizing radiation.

Further studies on the relationship between alpha-particle traversal of the cell nucleus and cell damage were carried out. Raju and co-workers used alpha particles to irradiate five different cell lines and found that the mean number of alpha-particle traversals inducing a lethal lesion varied between 2 for HS-23 cells and 6 for C3H 10T1/2 cells. The RBE values for all cell lines were about 3.8 at 10% survival. The average number of alpha-particle traversals producing a single lethal lesion was greater than one. The traversals that do not kill the cells may lead to carcinogenic effects (5).

The development of charged-particle microbeam technology (figure 3-1), cell subcompartment staining techniques, image analysis and automated cell positioning have provided better tools to assess a variety of endpoints with exact numbers of alpha particles targeted to cell nuclei and their cytoplasm compartments. Miller et al. investigated the oncogenic effects produced by the passage of exact numbers of alpha particles traversing mammalian cell nuclei. By using a microbeam to produce an exact number of alpha particles and a broad beam to produce a mean number of alpha particles determined by Poisson statistics distribution, they found that the effect of exactly one alpha particle traversal was not significantly different from the controls with no traversal and concluded that the majority of transformed cells resulted from more than one alpha-particle traversal (6). Hei et al. used the microbeam source to examine the relationship between exact numbers of nuclear hits by alpha particles and mutagenicity for a human-hamster hybrid (A_L) cell line. They found that although single-particle traversal was only slightly cytotoxic to A_L cells (survival fraction approximately 0.82), it was highly mutagenic. The mutant

induction increased with increasing nuclear traversals over a dose range of 1-8 alpha particles per nucleus. These data provided direct evidence that a single alpha-particle traversal of a nucleus would have a high probability of mutation (7). The microbeam studies also provided further evidence that cellular cytoplasm is less radiosensitive than DNA (6).

Although the microbeam technique has improved the accuracy of the nuclear irradiation experiments, other problems still existed. When alpha particles were aimed at the nuclei of the cells, they had an opportunity to react with nearby extracellular fluid, the cell membrane and the cytoplasmic compartment on their way to reach the nuclei. So the nuclear effects might also reflect effects coming from other targets.

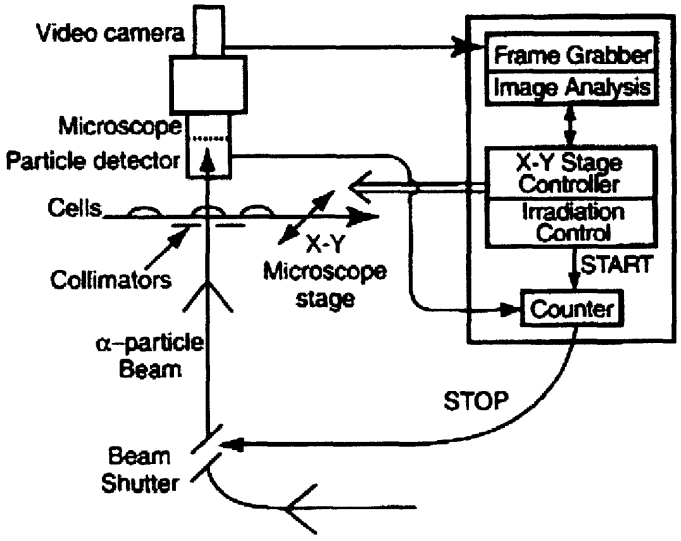

Figure 3-1. A schematic diagram of the microbeam system in the Center for Radiological Research at Columbia University. The microbeam facility was designed to deliver defined numbers of helium or hydrogen ions produced by a 4-MV van de Graaff accelerator, covering a range of LET from 30 to 220 keV/μm, into an area smaller than the nuclei of human cells growing in culture on thin plastic films. The overall irradiation throughput for the microbeam was about 10,000 cells/h (6).

Radiation can induce different types of DNA damage such as DNA single strand breaks and double strand breaks, modification of deoxyribose rings and bases, intra- and inter-strand DNA-DNA cross-links and DNA-protein cross-links, through direct and indirect interactions. Some damage like single strand breaks can be easily repaired, resulting in little biologic consequence. Mis-repaired or un-repaired damage lead to destructive consequences such as cell death, immediate or delayed reproductive incapacitation, chromosomal aberration, mutation and carcinogenesis.

In experimental radiobiology, a variety of protocols or assays have been developed to detect and measure cell damage. The clonogenic assay (colony forming assay) is a fundamental way to evaluate one kind of severe cell damage - cell death. A cell-survival curve describes the relationship between the radiation dose and the proportion of cells that survive. Cell death may have different meanings in different contexts. In the clonogenic assay, cell death means loss of the capacity for sustained proliferation or loss of reproductive integrity. A cell may still be physically present and be able to make proteins or synthesize DNA, and may even be able to struggle through one or two cell cycles; but if it has lost the capacity to divide indefinitely, it is, by definition, dead. Only cells that are able to proliferate indefinitely to produce a large clone or colony containing more than 50 cells are considered to be clonogenic or to have survived. This assay can only be used with immortal cell lines.

Compared to the clonogenic assay which provides cell survival information at the population level, the single cell gel electrophoresis assay (also known as the comet assay) is a simple, rapid and sensitive technique for analysing and measuring DNA damage in individual mammalian (and to some extent prokaryotic) cells. It was first introduced by

Ostling and Johanson in 1984 (8). Their version was a neutral assay in which the lysis and electrophoresis were done under neutral conditions. Staining was done with acridine orange. The resulted image looked like a "comet" with a distinct head, comprised of intact DNA, and a tail, consisting of damaged or broken pieces of DNA. This was where the name "comet assay" came from. The extent of DNA liberated from the head of the comet was a function of the radiation dose. However, in this procedure, only double strand breaks could be analyzed.

The neutral assay was modified by two groups, Singh and co-workers in 1988 (9) and Olive et al. in 1989 (10). Singh et al. used microgels, involving electrophoresis under highly alkaline conditions (pH>13). This enabled the DNA supercoils to relax and unwind, which are then pulled out during application of an electric current which made possible the detection of single strand breaks in DNA and alkali-labile sites expressed as frank single strand breaks in individual cells. This method was developed to measure low levels of strand breaks (9). Olive and co-workers conducted the electrophoresis under neutral or mild alkaline conditions (pH=12.3) to detect single strand breaks. This method was optimized to detect a subpopulation of cells with varying sensitivity to drug or radiation (10). The alkaline buffer technique of Singh et al. was found to be one or two orders of magnitude more sensitive than the other techniques.

Since then a number of advancements has greatly increased the flexibility and utility of this technique for detecting various forms of DNA damage (11-15). The comet assay essentially measures the sizes of DNA fragments within the cell. It is therefore necessary to convert DNA damage to DNA fragments by introducing breaks at the sites of DNA damage before being able to detect with the comet assay. The simplest types of

DNA damage detected by the neutral comet assay are the Double Strand Breaks (DSBs). DSBs within the DNA result in DNA fragments and can be detected by merely subjecting them to electrophoresis at neutral pH. Single Strand Breaks (SSBs) do not produce DNA fragments unless the two strands of the DNA are separated/denatured. This is accomplished by unwinding the DNA at pH 12.1. Other types of DNA damage broadly termed as alkali labile sites (ALS) are expressed when the DNA is treated with alkali at pH greater than pH 13. Furthermore, breaks can be introduced at the sites of DNA base modifications by treating the DNA with lesion-specific glycosylases/endonucleases and the fragments thus produced can also be detected by the comet assay. Therefore, by controlling the conditions that produce breaks at the sites of specific DNA lesions, the comet assay can be used to detect various classes of DNA damage and DNA repair in virtually any eukaryotic cell.

In summary, the assay works upon the principle that strand breakage of the supercoiled duplex DNA leads to the reduction of the size of the large molecule and these strands can be stretched out by electrophoresis. Also, under highly alkaline conditions there is denaturation, unwinding of the duplex DNA and expression of alkali labile sites as single strand breaks. Comets form as the broken ends of the negatively charged DNA molecule become free to migrate in the electric field towards the anode. Two principles in the formation of the comet are:

- DNA migration is a function of both size and the number of broken ends of the DNA
- Tail length increases with damage initially and then reaches a maximum that is dependent on the electrophoretic conditions, not the size of fragments.

Jostes *et al.* used the comet assay to identify cells that are hit by the alpha particles from the cells that escape damage (16). The histogram of their comet assay results showed a bimodal distribution after 0.39 Gy Radon (alpha-particle irradiation) in the A_L cell line (figure 3-2) and the CHO cell line (not shown here). Our hypothesis is, if the comet assay is sensitive enough to differentiate the hit cells from the non-hit cells after the alpha-particle irradiation, it might be able to differentiate the bystander cells from both hit and non-hit cells in the same population. To observe and study the bystander effect is the main focus of this project.

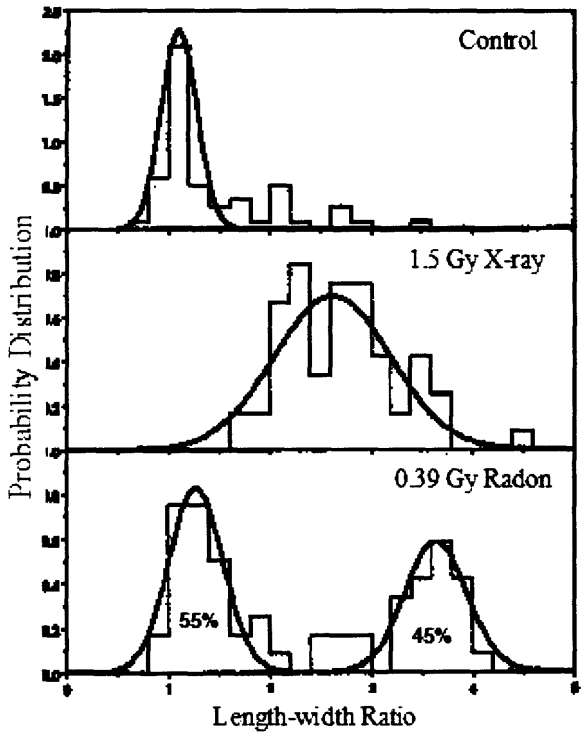

Figure 3-2. Graph from Jostes's paper "Single-cell gel technique supports hit probability calculation". Single –cell gel data from the A_L cell line. Two slides, representing a total of 60 cells, were evaluated for each of the treatments. The top panel illustrates the probability distribution for the unirradiated cell population; the middle panel illustrates the probability distribution for the low-LET X-ray control; the bottom panel illustrate the probability distribution for the radon-irradiated population (16).

3.2 Materials and Methods

3.2.1 Cell culture conditions

The DU-145 human prostate carcinoma (metastatic) cell line was obtained from the American Type Culture Collection (Cat. No. HTB-81). The cells were grown at 37 °C in a humidified atmosphere of 95% air and 5% CO_2 with Eagle's Minimum Essential Medium containing Earle's BSS and 2 mM L-glutamine (MEM/EBSS; HyClone), supplemented with 1.0 mM sodium pyruvate (SH30239.01, HyClone), 0.1 mM nonessential amino acids (SH30238.01, HyClone), 1.5 g/L sodium bicarbonate (SH30033.01, HyClone) and 14% fetal bovine serum (FBS; Sigma). The cell doubling time was about 34 hours. The cells were sub-cultured once per week, and the medium was changed approximately every 3-4 days. The DU-145 cell line passage number was 57 upon arrival from the ATCC. The cells were cultured for another three passages before multiple aliquots (~ 10^7 cells per vial) were frozen in cryovials and stored in liquid nitrogen. Since one passage of cells would be slightly different than another passage, every frozen vial of stock DU-145 cells was used for about two months (8 passages) and all experiments were carried out with cells between passage numbers 60 and 68.

3.2.2 Cell counting methods

For many applications that require the use of suspensions of cells, it is necessary to determine cell concentration and cell number. The most widely used type of cell counting device is the hemocytometer (see figure 3-3).

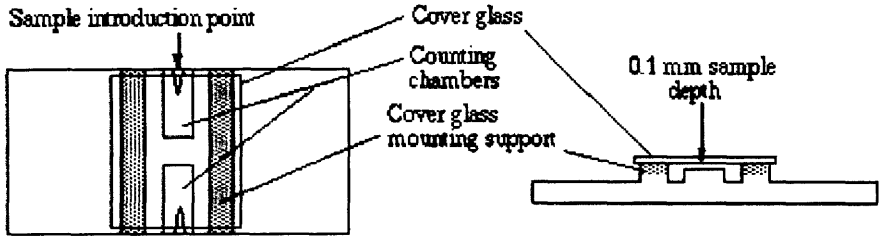

Figure 3-3. Schematic view of the hemocytometer

Before use, the mirror-like polished surface and the coverslip were carefully cleaned with alcohol. Coverslips for the hemocytometer are specially made and are thicker than those for conventional microscopy, since they must be heavy enough to overcome the surface tension of a drop of liquid. The coverslip was placed over the hemocytometer prior to putting on the cell suspension. The suspension was introduced into one of the V-shaped wells with a pipet. The area under the coverslip was filled by capillary action. Enough liquid should be introduced so that the mirrored surface is just covered. The filled hemocytometer was then placed on the light microscope stage and the counting grid was brought into focus at 100× (10× objective) (see figure 3-4). The main divisions separate the grid into 9 large squares. Each square has a surface area of one square millimeter, and the depth of the chamber is 0.1 mm. Thus the entire counting grid lies under a volume of 0.9 mm^3.

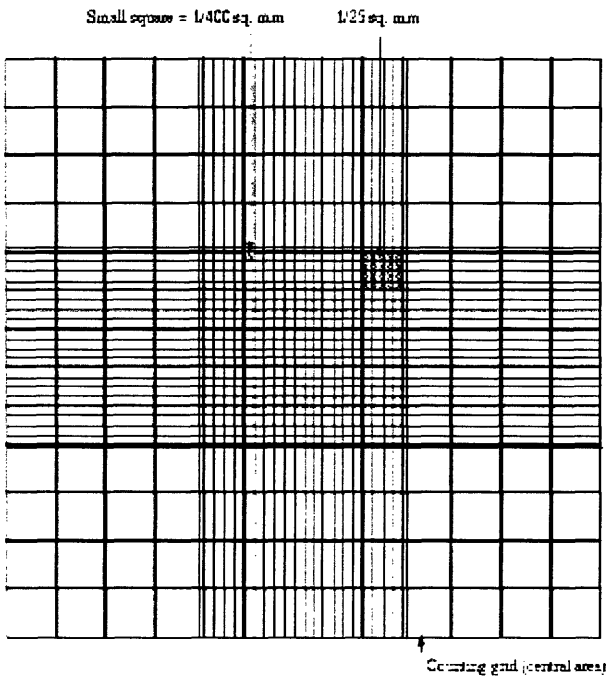

Figure 3-4. An entire counting grid of a hemocytometer, consisting of nine 1-mm^2 squares

Cell suspensions should be diluted to an extent that the cells won't overlap each other on the grid and there are at least 100 cells in each of the nine large squares to achieve a statistical meaning. The cell numbers in the four large corner squares and the middle one are counted. For cells that overlapped a ruling, a cell was counted as "in" if it overlapped the top or right ruling, and "out" if it overlapped the bottom and left ruling. Five cell numbers were obtained from one counting grid, n_1, n_2, n_3, n_4 and n_5. Another five cell numbers were obtained from the counting grid on the other side of the hemocytometer, n_6, n_7, n_8, n_9 and n_{10}. In order to determine the original cell concentration, the average count in ten large squares was calculated as n; then the average count n was divided by 0.1 mm^2 or 0.0001 ml, the volume under each large square. The resulting original cell concentration is $n \times 10^4$ cells/ml.

Use of the hemocytometer is time consuming and the results are affected by human factors, such as the volume of cell suspension introduced into the counting chamber. An automated cell counting device called Coulter Counter was used to save the time and improve the consistency and accuracy of the results.

The Z2 Coulter Counter from Beckman Coulter is a cell and particle counter using the Coulter principle (Electrical Sensing Zone Method). The Coulter method of sizing and counting particles is based on measurable changes in electrical resistance produced by nonconductive particles suspended in an electrolyte. In addition to reporting cell count and concentration, it also provides size distribution of the cell population. To use the Coulter Counter, 1 ml of cell suspension was diluted to a total volume of 10 ml with electrolyte in a special cup. The cup was then put onto the Coulter Counter stage and the "start" button was pushed to start the process. The results were displayed on the screen of the control panel connected to the counter. The Coulter Counter was calibrated by the hemocytometer: the Coulter Counter was regarded as reliable when its counting result agreed with the hemocytometer counting result for the same cell suspension sample. Three measures were performed for each cup of cell sample and the average was calculated as the final result.

3.2.3 Cell survival experiments

For cell survival experiments, ~ 5 x 10^5 DU-145 cells were plated into the pre-coated Mylar dishes and allowed to attach overnight (16-22 hr). The medium was changed half an hour before the irradiation. Dose response curves were obtained by irradiating dishes with graded doses of alpha particles at room temperature. Following the irradiation, the cells were trypsinized (0.25% trypsin with 0.1% EDTA at 37 °C for 3 min), re-suspended with full growth medium and plated into 100 mm culture dishes for colony

formation assay. The medium was changed once after 5 days of growth (some protocol does not suggest medium change during the colony formation period and similar results were obtained using the two protocols in our lab). After 10 days of growth, the colonies were washed with phosphate buffered saline (PBS), fixed with 95% ethanol, and stained with 1% methylene blue aqueous solution. After staining for 5 to 10 minutes, the extra methylene blue solution was collected back into the original bottle, and the dishes were rinsed with running tap water and allowed to air dry. The colonies that contained 50 or more cells were counted. Each colony represented one surviving cell. Five duplicate dishes were scored per dose point in each experiment. The average cell survival fraction equaled the average number of colonies divided by the average number of cells plated. The surviving fraction for the control group is called plating efficiency (PE ratio). The surviving fractions in the radiation groups were normalized to the corresponding plating efficiencies. For X-ray irradiations, DU-145 cells were plated into the pre-coated Mylar dishes and allowed to attach overnight. Irradiations with X-rays were carried out using a Phillips RT250 unit operating at 250 kV and 12 mA with 0.4 mm Sn plus 0.25 mm Cu added filtration and a focus-to-target distance of 32 cm. The average X-ray dose rate in the cell culture flask was 1.0 Gy/min. After irradiation, the cells were trypsinized and plated for colony formation as described before. The data for each dose point were pooled from multiple experiments. All data were shown as means ± standard deviation.

3.2.4 The comet assay

In order to run the comet assay, some basic materials and equipment were needed, including the comet assay slides, an electrophoresis tank and a variety of reagents. Although regular unpolished glass microscope slides work fine for the comet assay, sample

loss might occur during the slide washing steps. Trevigen (Trevigen, Inc., MD) provided a comet assay kit which contained specially designed and treated CometSlides and the following components:

Component	**Size**	**Storage Temp**
Lysis Solution	2 x 500 ml	18 – 24 °C
Comet LMAgarose	15 ml	18 – 24 °C
CometSlide	25 ea	18 – 24 °C
200 mM EDTA	12.5 ml	18 – 24 °C
SYBR® Green I nucleic acid gel stain	5 µl	-20 °C

Table 3-1. Components of the Trevigen comet assay kit

For convenience, the Trevigen comet assay kit was first used in our comet assay experiments. But sample loss still occurred during slide processing. Also it was recommended to use freshly made lysis solution before each experiment. To improve the outcome of the experiments, the comet assay slides and all necessary reagents were made freshly before the experiments.

2.1.1.1 Comet assay slides

Singh used newly designed clear window frosted slides for the comet assay in 1999 to improve agarose attachment (17). A similar type of commercially available slides (MGE slides, Erie Scientific Company, Portsmouth, NH, Cat. No. ES 370) coated with a thin layer of normal melting agarose were used in our experiments. The surrounding frosted area provided better attachment for agarose and the middle clear window avoided the uneven background for image analysis. It worked much better and no sample loss ever occurred after using these pre-coated slides. The following is the procedure to prepare the slides:

1. Prepare 0.5% low melting agarose (LMA) (250 mg per 50 ml) and 1.0% normal melting agarose (NMA) (500 mg per 50 ml) in PBS. Microwave or heat until near boiling and the agarose dissolves. For LMA, aliquot 5 ml samples into scintillation vials (or other suitable containers) and refrigerate until needed. When needed, briefly melt agarose in microwave or 100°C water bath. Then place melted LMA vial in a 37°C water bath to cool and stabilize the temperature.
2. While NMA agarose is hot, dip the MGE slides (or conventional slides) to a desired position and gently remove. Wipe underside of slide to remove agarose and lay the slide in a tray on a flat surface to dry. The slides may be air dried or warmed for quicker drying. Store the slides at room temperature until needed; avoid high humidity conditions.

3.2.4.1 Electrophoresis apparatus

A horizontal electrophoresis tank with passive re-circulation from Fisher Scientific (FB-SBR-2025) was used in our experiments. The power supply was set to generate 1 volt per cm. The distance between the two electrodes was 36 cm. So the applied voltage was 36 volt. The volume of the buffer was adjusted to generate 250 mA current in the buffer (about 1.6 L). The electrophoresis time was chosen according to the specific cell line and the extent of the DNA damage. The optimal time should result in minimum DNA migration in control cells but maximum DNA migration in treated cells. H_2O_2 is an agent known to cause single strand breaks in DNA. 100 μM H_2O_2 treatment for 20 minutes at 4 °C was used as positive control. The alkaline comet assay was used for detection of single strand breaks after H_2O_2 treatment. During electrophoresis, the slides were placed along the edge of one side (see figure 3-5) to ensure that all samples were subject to as even an

electric field as possible. If the sample slides were not enough to fill all the positions on the edge, slides without cell samples were used to occupy the empty positions. The sample slides were preferably placed in the positions from '2' to '7' to avoid a "fringe effect" of the electric field. The test for the uniformity of the electric field along the edge was performed by comparing the comet assay results among slides placed in different positions from '2' to '7' with the same batch of cells after 100 μM H_2O_2 treatments for 20 minutes.

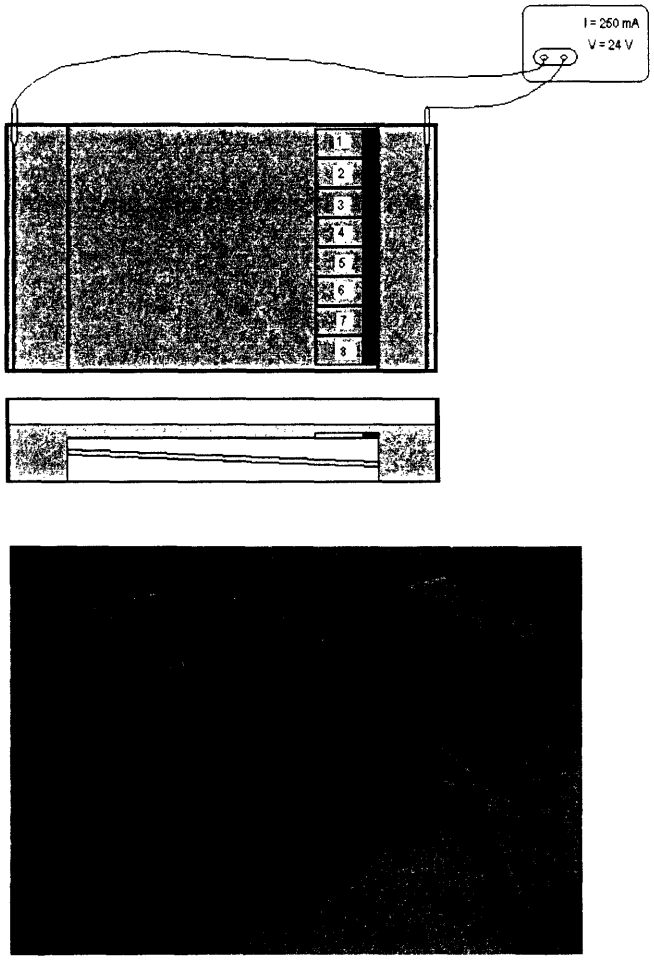

Figure 3-5. *Top.* Schematic top-view and side-view of the electrophoresis tank. *Bottom:* The picture of the electrophoresis tank connected with the power supply.

3.2.4.2 Reagent preparation

1. 1×PBS (phosphate buffered saline) was diluted from 10×PBS stock in DI water. It was calcium and magnesium free to inhibit endonuclease activities.

2. Lysis solution could be obtained directly from the Trevigen kit or made freshly. If it was made freshly, the following was the procedure: Ingredients per 1000 ml: 2.5 M NaCl (146.1 mg), 100 mM EDTA (37.2 mg) and 10 mM Trizma base (1.2 mg). Add ingredients to about 700 ml distilled water, (DI water) and begin stirring the mixture. Add ~8 gm NaOH and allow the mixture to dissolve (about 20 min). Adjust the pH to 10.0 using concentrated HCl or NaOH and volume to 890 ml with distilled water (the Triton X-100 and DMSO (dimethyl sulfoxide) will increase the volume to the correct amount), and store at room temperature. Final lysing solution: add fresh 1% Triton X-100 and 10% DMSO, and then refrigerate for at least 30 minutes prior to slide addition.

3. Alkali solution was prepared freshly according to the following formula: 0.6 g NaOH pellets + 250 μL 200 mM EDTA + 49.75 ml DI water = 50 ml alkali solution.

4. Neutralization Buffer was prepared according to the following formula: 48.5 mg 0.4 M Tris was added to ~800 ml DI water, adjust pH to 7.5 with concentrated 10 M HCl: q.s. to 1000 ml with DI water, store at room temperature.

5. TBE Electrophoresis buffer was prepared: 1×TBE (0.089 M TRIS, 0.089 M Borate, 0.002 M EDTA) was diluted from 10×TBE stock in DI water. 1×TBE was used for electrophoresis because of its buffering capacity. To prepare 10×TBE, dissolve 108

g Tris base, 55 g boric acid and 9.3 g of EDTA disodium salt in 900 ml of DI water. Adjust volume to 1 liter and autoclave. The total volume of buffer used in the experiments was 1.6 liter.

6. SYBR Green staining solution was prepared from the SYBR Green concentrate provided by the Trevigen kit. Dilute 1 μL of the concentrate to 10 ml TE (pH=7.5). SYBR Green's maximum excitation and emission are respectively 494nm/521nm. The diluted stock was stable for several weeks when stored at 4 °C in the dark.

During sample preparation, all the buffers were chilled to 4 °C to inhibit endogenous damage from occurring and to inhibit repair in the unfixed cells.

3.2.4.3 Cell culture and treatment

The DU-145 cells were plated into the Mylar dishes one day before the experiments and allowed to attach overnight. For positive control experiments with H_2O_2, the cells could be grown in either T25 flasks or Mylar dishes. Irradiation or H_2O_2 treatments at different doses were performed. After irradiation or H_2O_2 treatment, attached monolayer cells were trypsinized at 4 °C for about 10 min. The reason that the trypsinization was performed at 4 °C was to prevent the repair process that happens at 37 °C. This was also why the cells should be kept on ice or at 4 °C all the time. After trypsinization, the cells were resuspended at a concentration of about 1×10^5 cells/ml in ice cold medium. To ensure the required concentration, pilot studies were conducted to determine the yield of cells from T25 flasks or Mylar dishes and the appropriate volume of ice cold medium to use for resuspending the cells. Cell samples were handled under dimmed light to prevent DNA damage from ultraviolet light.

3.2.4.4 Experimental procedure

Figure 3-6 shows the experimental protocol of the comet assay. After treatment by radiation or other agents, the single cell suspension of the DU-145 cells was suspended in low melting agarose and layered onto MGE slides pre-coated with agarose. Lysis of the cells under high salt concentration was then carried out to remove cellular proteins and liberate the damaged DNA. The liberated DNA was subjected to unwinding under alkaline condition to allow DNA supercoils to relax and express DNA single strand breaks and alkali labile sites. Electrophoresis was then carried out under neutral condition, which allowed the smaller DNA fragments to migrate towards the anode under the effect of the electric field. The staining was done using fluorescent DNA dyes SYBR (or Ethidium Bromide). The slides were then kept in a humidified slide chamber until they were scored.

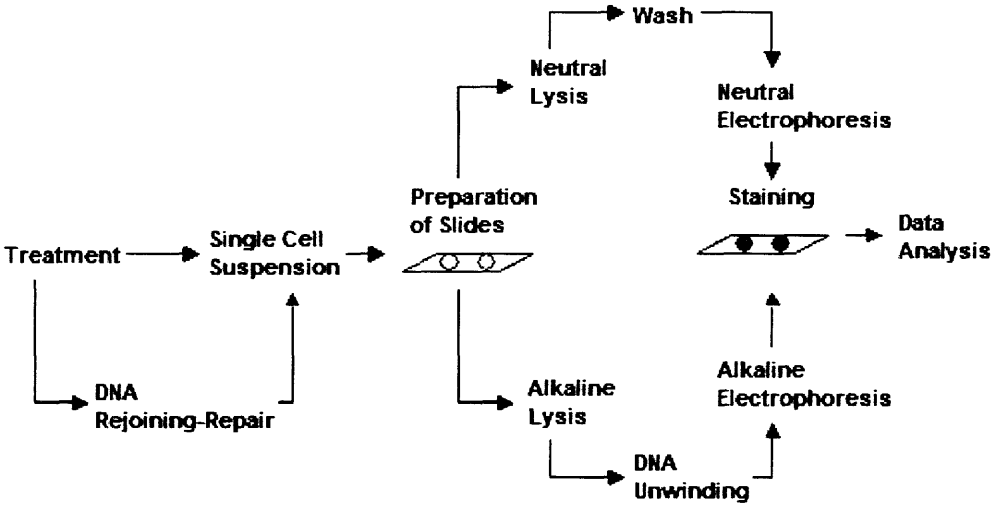

Figure 3-6. The schematic experimental protocol of the comet assay (Neutral and Alkaline)

The following is the detailed alkaline comet assay procedure used in the experiments described in this chapter:

1) Melt LMA in a beaker of boiling water for 5 minutes, with the cap loosened. Place bottle in a 37°C water bath for at least 20 minutes to cool down. The temperature of the agarose was critical. If it was too high, the cells would be damaged.

2) Combine cells at 1×10^5 cells/ml with molten LMA (at 37°C) at a ratio of 1:10 in volume. Mix them by gently pipetting twice and immediately transfer 75 µl onto the pre-coated slides. Let the agarose/cell cover the sample area.

3) Place the slides flat at 4 °C in the dark refrigerator for 10 min for adherence.

4) Immerse the slides in pre-chilled lysis solution and leave at 4 °C for 60 min.

5) Tap off excess lysis solution from the slides and immerse in freshly prepared alkaline solution (pH > 13). Leave the slides in alkaline solution for 60 minutes at room temperature, in the dark.

6) Remove the slides from alkaline solution, gently tap excess buffer from the slides and wash by immersing in 1×TBE buffer for 5 min twice.

7) Transfer the slides from 1×TBE buffer to a horizontal electrophoresis apparatus. Place the slides flat onto the gel tray and align equidistant from the electrodes. Pour 1.6 liter pre-chilled 1×TBE buffer to the tank. Set power supply to 36 volt (1 volt per cm). The volume of the buffer was adjusted to generate 250 mA current. Apply voltage for a period of time. The optimal time should result in minimum DNA migration in control cells but maximum DNA migration in treated cells. It was determined in one experiment on cells treated with 100 µM H_2O_2 for 20 minutes.

8) At the end of the electrophoresis, turn off the power and gently lift the slides from the buffer and place on a drain tray.

9) Very gently tap off excess liquid and dip the slides in cold 100% ethanol for 5 min.

10) Air dry samples. Drying brings all the cells in a single plane to facilitate observation. Sample slides were stored at room temperature, with desiccant until scoring.

11) Before scoring, stain the slides with 100 µl diluted SYBR Green solution for 10 min at room temperature. Place a cover slip to ensure even staining. Then take off the cover slip and wash the slides with PBS twice. Place a fresh cover slip and blot away excess liquid on the back and edges. Score at least 200 cells per sample. After scoring, remove cover slip, rinse in 100% alcohol to remove stain, let dry and store.

3.2.4.5 Data analysis

There are a number of different methods to score the DNA in the tail of the unwound comets. The simplest technique is to score the comets empirically on the basis of damage extent. Because the assay produces a visual endpoint, it is possible to score the comets based on their appearance as damaged, undamaged, or with a simple scoring system to grade the extent of damage. This method of evaluation, although lacking in sophisticated image analysis, has been used with some success (18). This qualitative analysis was performed at an early stage of the experiments. After staining with SYBR, the sample slides were observed and recorded under a fluorescent microscope (Zeiss, Axioplan-2 imaging). The comets were put into one of four categories according to their appearance (length and intensity of the tails).

To facilitate the data analysis process, an automated comet assay analysis system from Loats Associates (LAI) was used for the quantitative analysis of the comet data. The LAI Automated Comet Assay Analysis System (LACAAS) from Loats Associates, Inc. (LAI), is a modular system of hardware and software that offers the features and components needed for collection and automated analysis of large sets of fluorescent single-cell comet images. Appropriate measurement and quantitative analysis of fluorescence intensities exhibited by the cells indicated cellular DNA content, distribution, and damage. The LACAAS Comet Assay software was designed to operate under the Windows operating system. It offers a proprietary image capture system that provides extended dynamic range imaging (EDRI) capabilities. Unlike conventional image capture systems, the EDRI system enables detection and digital recording of the full range of fluorescent intensity important for accurate analysis of comet images. Comet images were corrected to remove

any superimposed background noise signals, before quantitative analysis for DNA damage proceeds. The LACAAS automatically generated multiple quantitative measures of each cell analyzed, including standardized measures of comet tail length, area, moment, moment arm and moment of inertia, as well as measures of cellular DNA content, percent of total cellular DNA in the tail and a measure of total cellular DNA fragmentation. All measures were automatically saved to a data base, along with their corresponding comet images, for subsequent review and statistical analysis (see figure 3-7). The data were exported to Microsoft Excel for further analysis.

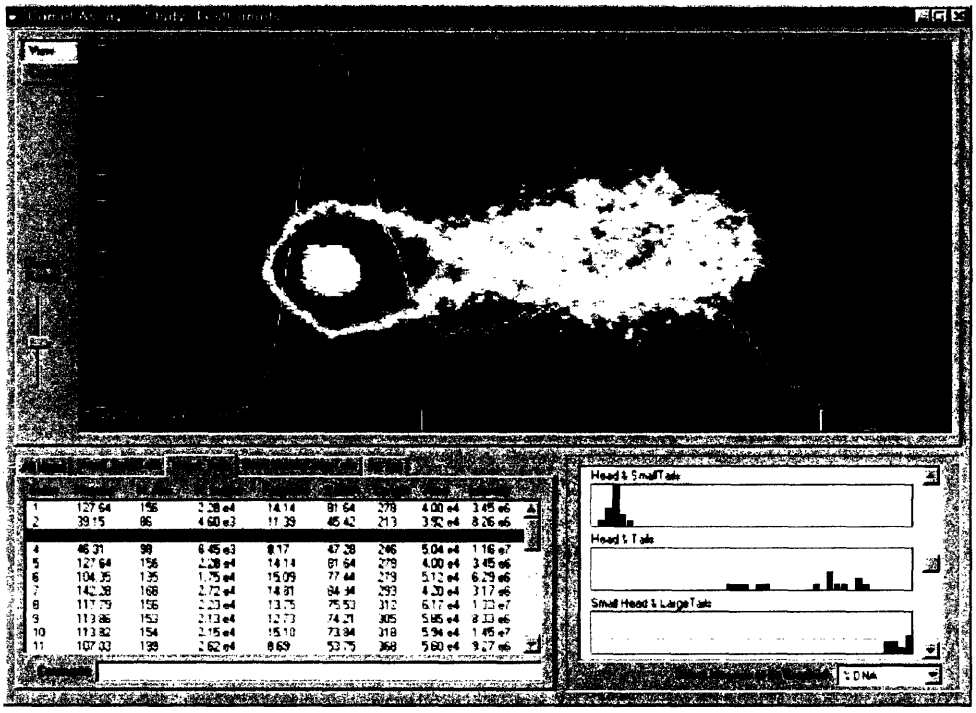

Figure 3-7. The integrated window of the LAI's Automated Comet Assay Analysis System. The upper window is for the comet images. Different colors represent different fluorescent intensities (white-high intensity; red-low intensity). The image comes with an intensity curve and two bars, which define the tail region. The lower left window gives measured data for individual comets. The lower right window provides group statistical information and comparison of multiple study groups, with respect to the distributional properties of selected comet analysis endpoints.

The distance of DNA migration from the nuclear core, as defined as tail length, is a parameter commonly used to evaluate the extent of DNA damage. An increasing popular method of comet evaluation is "tail moment", which is defined as the product of the tail length and the fraction of total DNA in the tail. Tail moment incorporates a measure of both the smallest detectable size of migrating DNA (reflected in the comet tail length) and the number of relaxed/broken pieces (represented by the intensity of DNA in the tail). Tail length and tail moment were two endpoints used in this study.

Three different graphical tools are used to demonstrate the results in this chapter: mean ± SD, histogram and boxplot. The "mean ± SD" is the most fundamental statistical way to describe a group of experimental data. The histogram shows the frequency distribution of the experimental data using bars. And the boxplot is a graphical summary of a distribution as shown in figure 3-8.

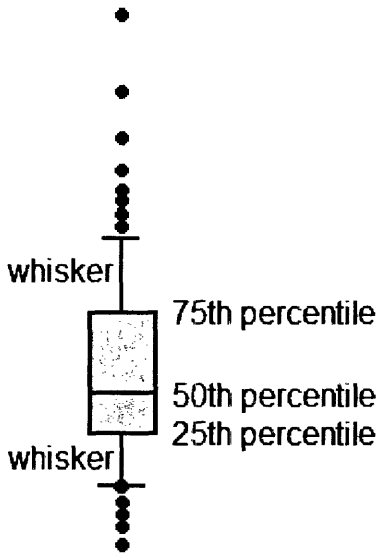

Figure 3-8. Illustration of the boxplot. The boxplot is often called the "box and whisker" plot. The "box" in a boxplot is defined by the lower 25th percentile line and the upper 75th percentile line. The median is the score at the 50% percentile: half of all scores are higher than the median, and half of them are lower than it. The 25th percentile is the point than which 25% of the scores are lower. The 75th percentile is the point than which 75% of the scores are lower. Thus, the area in the "box" represents the middle 50% of the data. The length of the box in a box plot, i.e., the distance between the 25th and 75th percentiles, is known as the interquartile range. Whiskers above and below the box indicate the 90th and 10th percentiles. The symbols beyond the 10th and 90th percentiles represent outliers or extreme data.

2.1.2 Micronucleus assay

The presence of micronuclei (MN) was evaluated by the cytokinesis-block technique (19) (see figure 3-9). After trypsinization, all harvested cells were transferred into two-well chamber slides (Lab-Tek Π, Nalge Nunc Int., Rochester, NY). Gentle pipetting was used to separate the cells and to distribute them evenly on the slides. The cells were allowed to attach in the chamber slides for 3-5 hrs before the medium was replaced with fresh growth medium containing 3 μg/ml cytochalasin-B (Sigma) to block cytokinesis. Cytochalasin-B works to inhibit the actins, proteins involved in cell division and therefore to inhibit the cytokinesis. The cells were incubated for 42 hrs (~1.5 doubling times) to accumulate bi-nucleated cells (BN). At the end of the incubation, the cells were rinsed twice with PBS and fixed twice at 4°C with ice cold fixation solution (3:1 methanol to acetic acid) for 1 hr each time. The chamber slides were air-dried, stained with 1 ml of 10 μg/ml DAPI (Sigma-Aldrich) for 10 minutes, and then washed once with PBS. The chamber walls were then removed, the mounting medium with anti-fade reagent (Fluoro Guard, Bio-Rad Laboratories) was added to the slides, the cover-slips were added and pressed to spread the anti-fade reagent evenly and squeeze out the air. The slides were finally sealed with nail polish. The slides could be stored at 4°C in the dark for several months to be scored before fading became apparent. The slides were observed under an epi-fluorescence microscope (Olympus BX51) at 400× magnification (see figure 3-10). For each sample, 1000-2000 bi-nucleated cells were scored and the percentage of bi-nucleated cells that contains MN (expressed as MN/BN ratio) was determined. Data from multiple replicate experiments were combined and plotted as mean ± SD. For statistical analyses of the MN/BN ratios between different experimental groups, the mean, SD and number of

independent samples scored were compared using an unpaired t-test (GraphPad Software, Inc.).

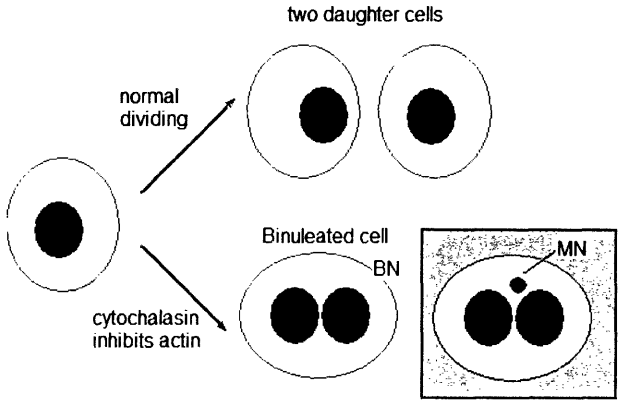

Figure 3-9. Schematic view of the micronucleus formation process. In a normal situation (the upper process), a cell divides into two separate daughter cells, each containing one nucleus. With cytochalasin-B, an inhibitor of actins, the cell is blocked from cell division after the completion of nuclear division (the lower process). The resulting one cell containing two daughter nuclei is called a binucleated cell or BN. The micronucleus forms when a fragment of chromosome is broken off the main chromosome body due to damage, resulting in one or more micronuclei (MN) within the binucleated cell (BN). The presence of MN is a sign of severe damage to the cells. A BN cell with one or more MN was scored as one MN.

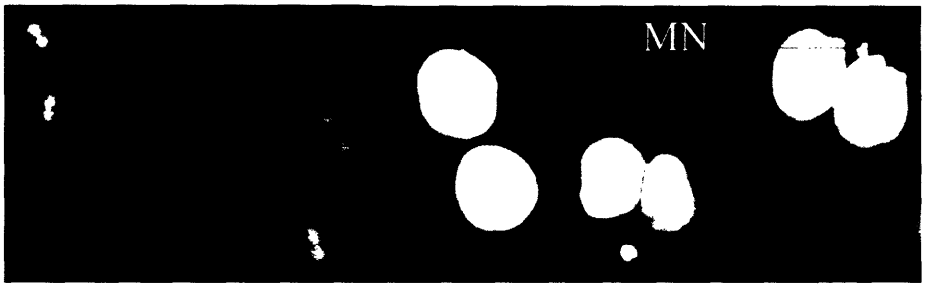

Figure 3-10. Pictures of binucleated cells (BN) with and without micronucleus (MN), stained by DAPI and recorded by an Olympus BX51 epi-fluorescence microscope. The magnification for the left image was 100× and for the right image was 400×.

Micronucleus assay was conducted on the directly irradiated cells in the Mylar dishes. Approximately 5×10^5 DU-145 cells were seeded in the Mylar dish the day before the experiments. The medium over the cells was replaced with fresh full growth medium half an hour before the irradiation. The monolayer of cells was then irradiated at doses of 0.1 Gy, 0.2 Gy, 0.3 Gy and 0.6 Gy. After the irradiation, the cells were trypsinized and processed for the micronucleus assay.

3.3 Results

3.3.1 Cell survival curves

Figure 3-11 shows the survival curves for DU-145 cells irradiated with alpha particles from foil #4 and with 250 kVp X rays. The data represent two independent X-ray experiments and five independent alpha-particle experiments. The alpha-particle dose response curve was fitted with an exponential function: surviving fraction SF = $\exp(-\alpha D)$, where $\alpha = 3.6\ Gy^{-1}$. The X-ray survival curve was fitted to the linear quadratic function: SF = $\exp(-\alpha D - \beta D^2)$, $\alpha = 0.37\ Gy^{-1}$ and $\beta = 0.0304\ Gy^{-2}$. The D_0 was 0.28 Gy for alpha-particle survival curve and 1.3 Gy for X-rays. The RBEs of the ^{241}Am alpha particles compared to the 250 kVp X rays at the 0.37, 0.1, and 0.01 surviving fraction levels were 12.0, 9.0, and 6.8, respectively. The RBE of the alpha particles estimated from the ratio of the initial slopes was 10.0.

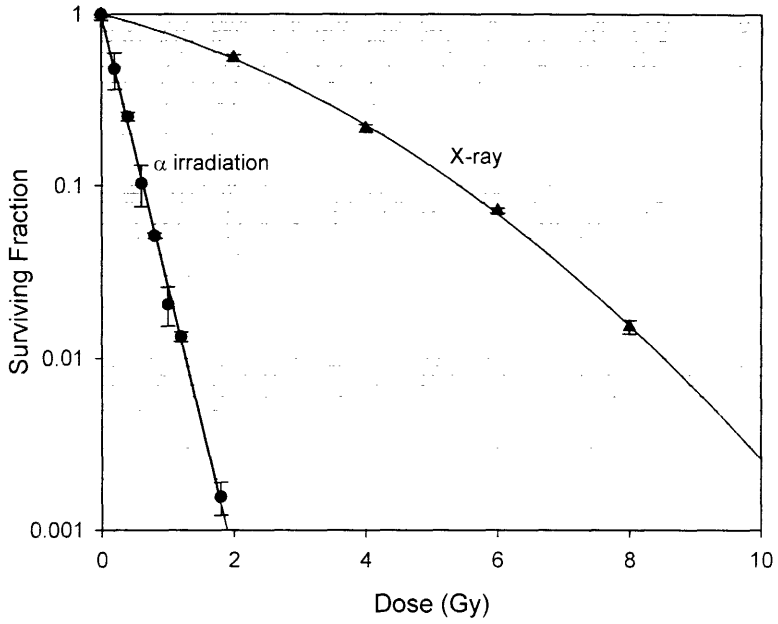

Figure 3-11. DU-145 cells survival curves for alpha-particle and X-ray irradiation. The fraction of cells surviving is plotted on a log scale against dose on a linear scale. For alpha-particle irradiation, the dose-response curve is a straight line from the origin, described by a linear function SF = exp (-3.6×D). For X-ray irradiation, the dose-response curve has an initial linear slope, followed by a shoulder, and tends to become straight again at higher doses. The X-ray curve can be fitted to a linear-quadratic function SF = exp (-0.37×D – 0.0304×D^2).

3.3.2 Comet assay results

Figure 3-12 shows the comet images at different damage levels after 1.2 Gy alpha-particle irradiation. Alpha-particle irradiation produced heterogeneous comets since irradiated cells could receive different numbers of alpha-particle hits for a irradiation dose. Table 3-2 gives the eight measurements from the LACAAS for the six comet images shown in figure 3-12.

Figure 3-13 shows comet images with unclean background. In this case, no accurate measurements could be obtained from the LACAAS.

Figure 3-14 shows the results of the uniformity test of the electric field in the electrophoresis tank. Figure 3-15 shows the electrophoresis time responses demonstrated in mean ± SD (from 20 to 100 minutes) after 100 μM H_2O_2 treatment for 20 min at 4 °C. Figure 3-16 shows the electrophoresis time response demonstrated in box plots for control and the 100 μM H_2O_2 treatment group. Figure 3-17 shows the tail lengths in histogram and box plot after graded alpha-particle irradiations (0, 0.2 Gy, 0.6 Gy and 1.2 Gy). Figure 3-18 shows the tail moment in histogram and box plot after graded alpha-particle irradiations.

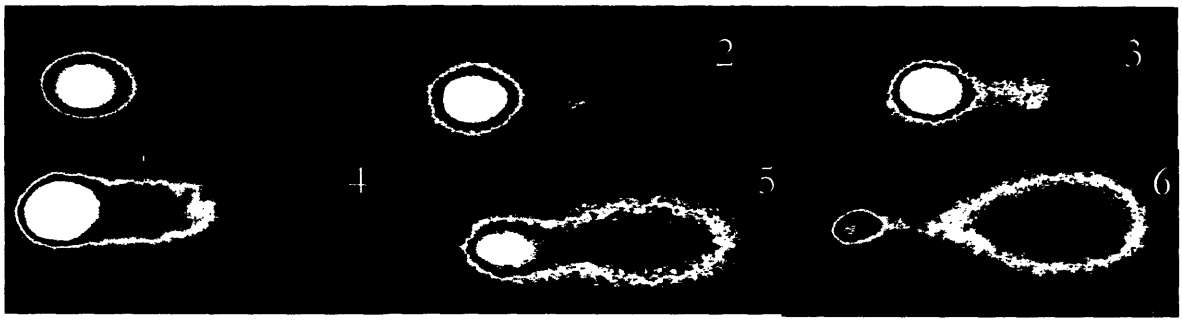

Figure 3-12. The DU-145 comet images at different damage levels after 1.2 Gy alpha-particle irradiation.

#	Moment	M. Arm	M. Inertia	Fragment.	% DNA	Length	Area	Intensity
1	0.00	0	0	4.80	0.06	1	54	244000
2	2.15	45	152	3.18	4.82	95	4500	3380000
3	3.30	45	204	3.67	7.29	105	6450	3180000
4	9.24	57	752	3.09	16.17	145	17500	6900000
5	56.57	109	8010	9.36	51.84	235	35300	4370000
6	142.28	168	27200	14.81	84.94	293	42000	3170000

Table 3-2. The comet assay analysis results for the six comet images showed in figure 3-12. Eight measurements were automatically generated by LACAAS for every captured comet image. Among the eight measures, the tail moment, % DNA and tail length are most commonly used for results analysis and demonstration.

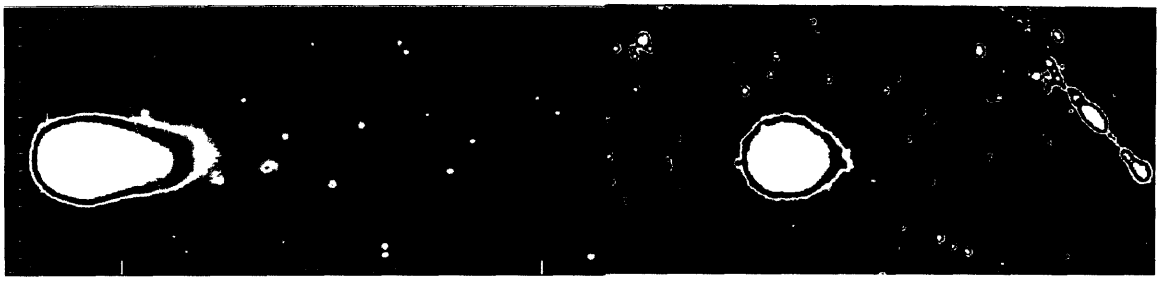

Figure 3-13. A common problem encountered in the comet assay analysis was unclean background. The LACAAS could not handle this situation therefore the results were unreliable. The problem usually came from careless handling of the sample slides so that dirt fell onto the slides and was stained by the fluorescent dye. Data corresponding to these images should be removed from the Excel files before further statistical analysis.

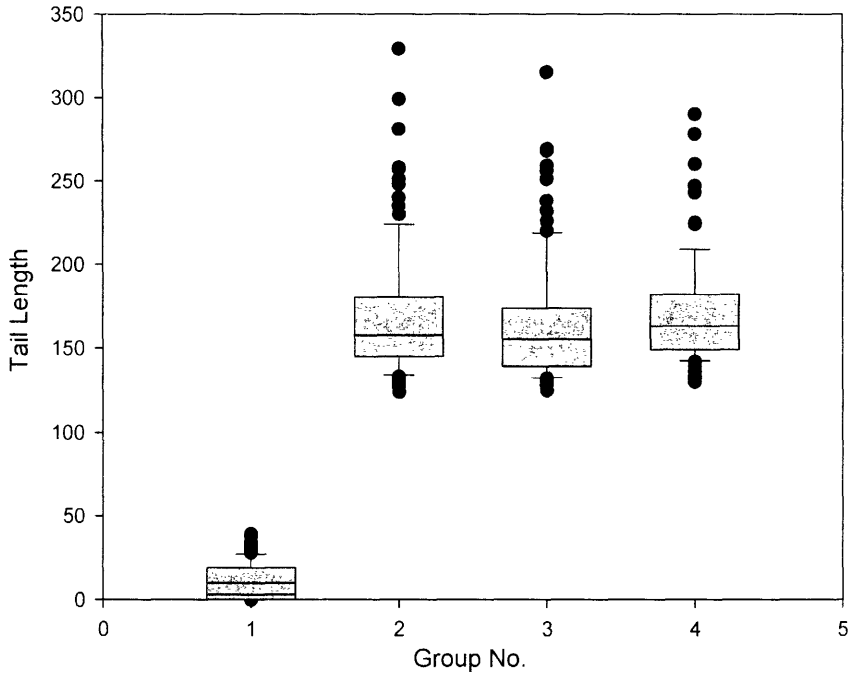

Figure 3-14. The uniformity test of the electric field. Group 1 was the control group, in which the cells were not treated with any damaging agent. Groups 2, 3 and 4 were cells treated with 100 μM H_2O_2 for 20 minutes at 4 °C. The control slide was placed in position 3 and the slides with 100 μM H_2O_2 treated cells were placed in positions 2, 4 and 6 along the edge of the electrophoresis tank. Positions 1, 5 and 7 were occupied with spare slides (see figure 3-7). About 100 cells were scored in each sample.

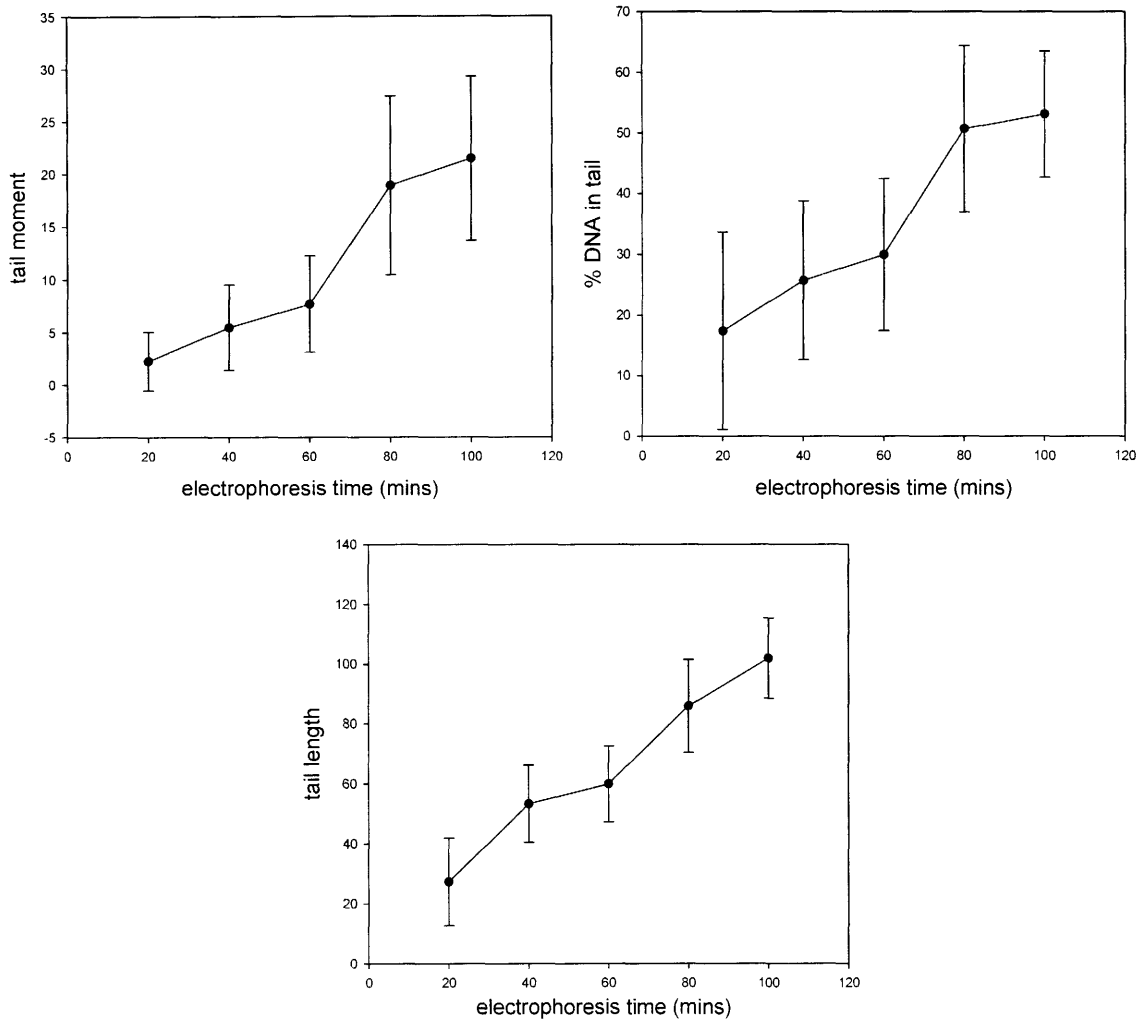

Figure 3-15. The test of different electrophoresis time in DU-145 cells treated with 100 μM H_2O_2 for 20 min at 4 °C. The x-axis represents different electrophoresis time. On the y-axis, the tail moment (up left), % DNA in tail (up right) and tail length (bottom) are demonstrated in mean ± SD. H_2O_2 is an agent to induce single strand breaks in cellular DNA. The alkaline comet assay was used to express the single strand breaks. 100-200 cells were scored in each group.

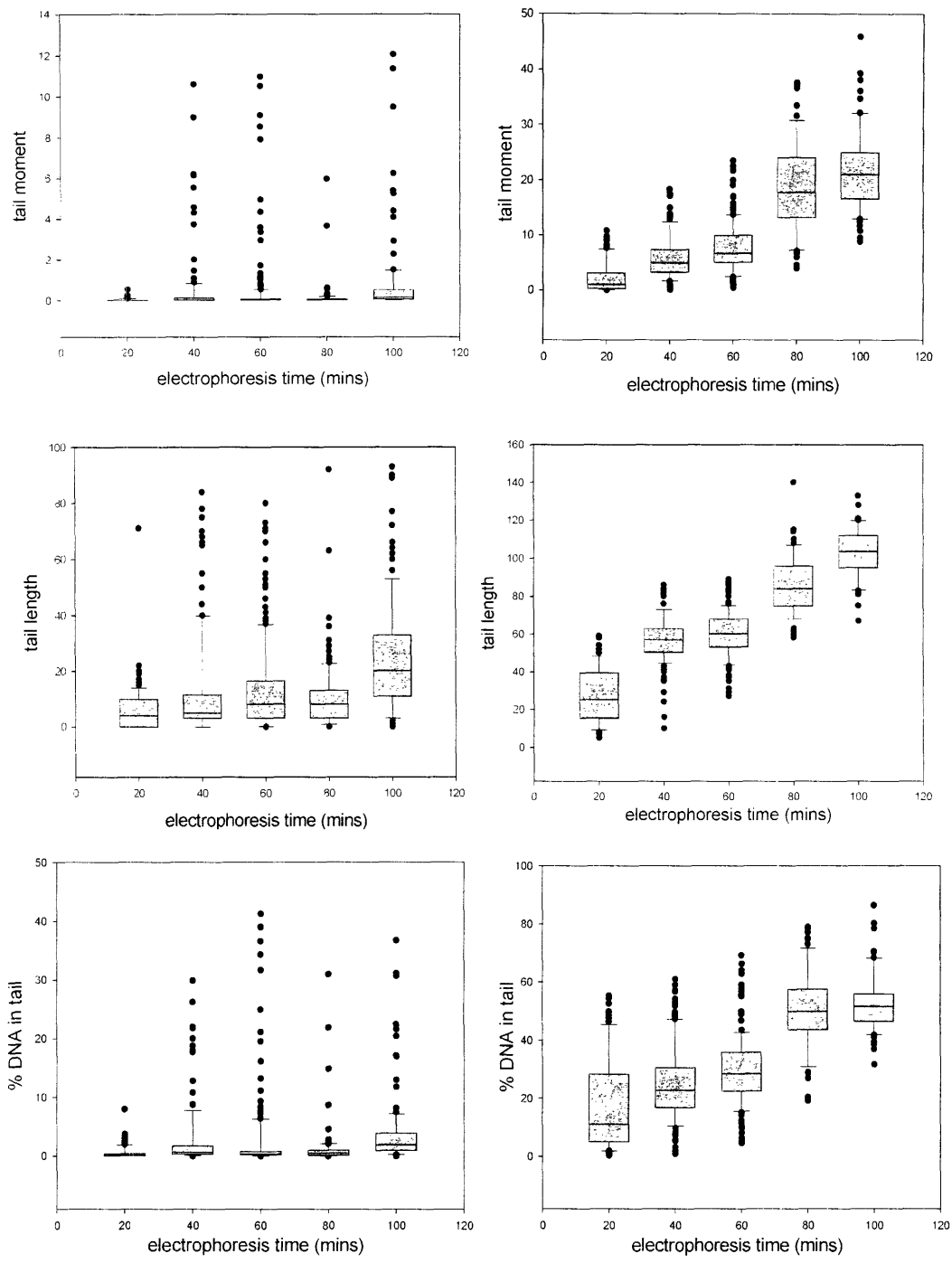

Figure 3-16. The tests of different electrophoresis time in control cells (left) and cells treated with 100 μM H_2O_2 for 20 mins at 4 °C (right). The x-axis represents different electrophoresis time. For the y-axes, the tail moment, tail length and % DNA in tail are shown in box plots. From the results, 40 mins was chosen for further experiments because it differentiated the H_2O_2 treated cells from the control cells better than 20 mins in all three endpoints. 60 mins did not seem to improve much compared to 40 mins.

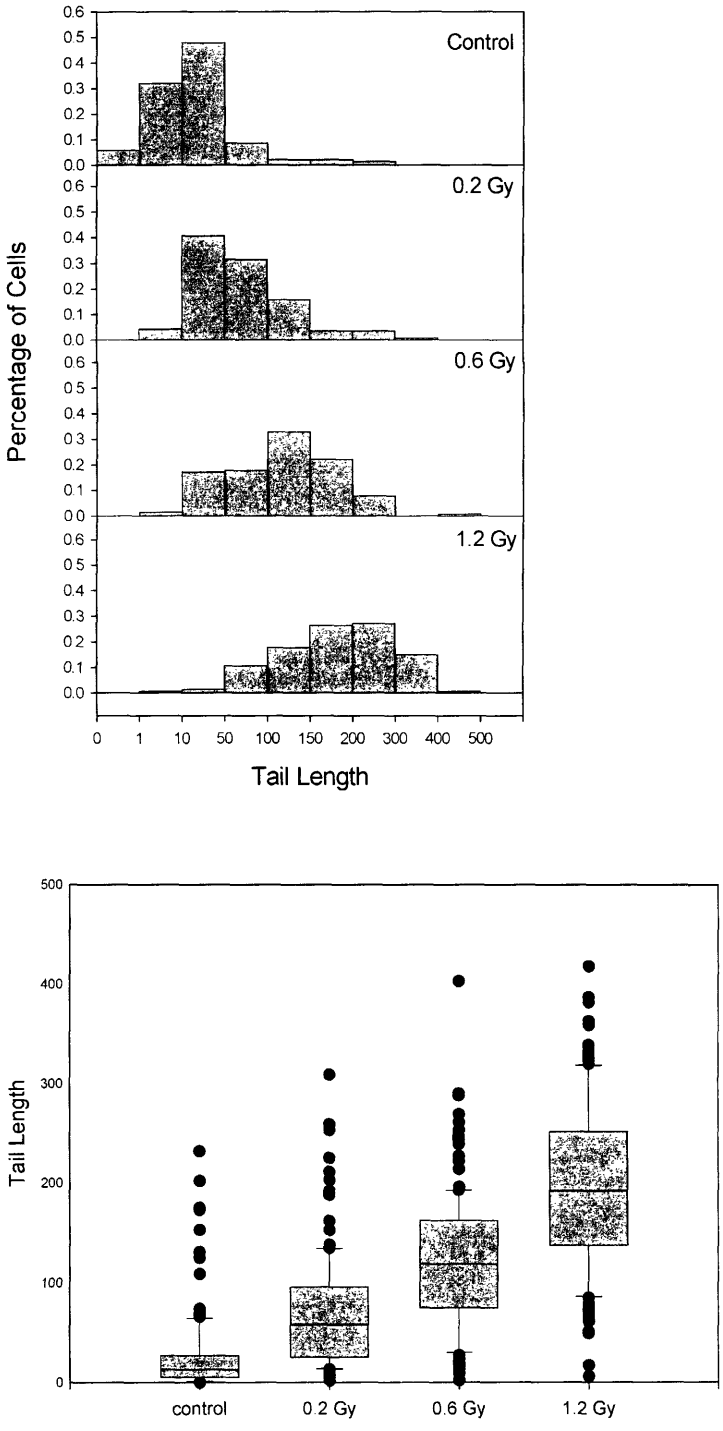

Figure 3-17. Tail length histogram (top) and box plot (bottom) for DU-145 cell comet assay results after 0, 0.2 Gy, 0.6 Gy and 1.2 Gy alpha-particle irradiations, under the alkaline comet assay condition and 40 minutes electrophoresis. More than 100 cells were scored in each group.

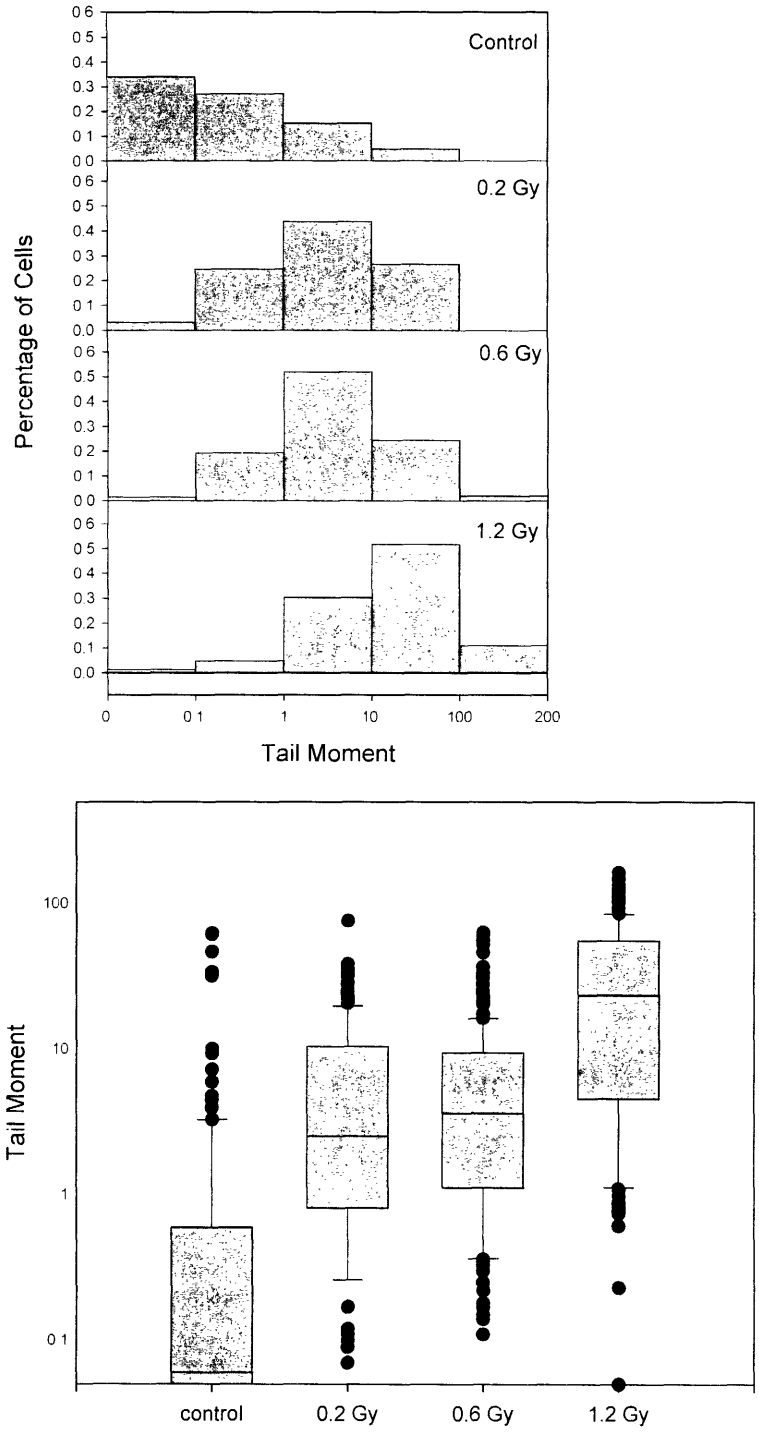

Figure 3-18. Tail moment histogram (top) and box plot (bottom) for the DU-145 cells after 0, 0.2 Gy, 0.6 Gy and 1.2 Gy alpha-particle irradiations, under alkaline comet assay condition and 40 minutes electrophoresis. For the box plot, the y-axis is on a log scale. More than 100 cells were scored in each group.

3.3.3 Micronucleus formation results

Figure 3-19 shows that, in the directly irradiated cells, the MN/BN ratio is a linear function of the average alpha-particle dose in the range of 0.1 to 0.6 Gy. Each data point is the mean of four independent samples and scoring of approximately 1000 cells per sample.

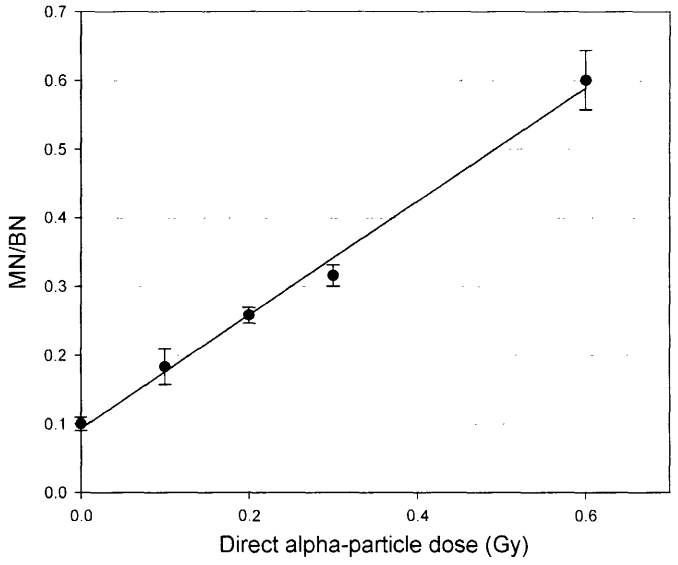

Figure 3-19. Dose response for micronucleus formation in DU-145 cells growing on the Mylar membrane and directly irradiated with alpha particles. Data points represent the mean ± SD of two independent experiments with approximately 1000 cells scored per experiment.

Inspection of the data in figures 3-11 and 3-19 allows a direct comparison of survival and MN/BN ratio for the DU-145 cells under the same irradiation conditions. E.g., a direct alpha-particle dose of 0.6 Gy reduced the clonogenic survival to approximately 10% and produced a MN/BN ratio of 60%. The cytochalasin-B block procedure (20) resulted in 82 ± 0.1% of the control cell population arrested in the binucleated state (%BN). Analysis of the %BN in the targeted cells exposed to direct alpha particle doses of 0.1, 0.2, and 0.3 Gy (see figure 3-19) indicated that 78 ± 1.2%, 74 ± 0.6%, and 70 ± 0.7%

of the cells were binucleated. These data suggest that the alpha particle doses may be causing a growth delay or interfering with the ability of the cells to progress through the cell cycle.

3.4 Discussion

In this chapter, three endpoints were used to measure the responses of DU-145 cells to the alpha-particle irradiation. The clonogenic assay was used to measure the cell survival rate at the population level; the comet assay was used to measure DNA strand breaks in individual cells; Micronucleus formation was used to measure the presence of micronuclei (MN) in binucleated cells. In the clonogenic assay, the DU-145 cells showed a linear dose response on log-scale for alpha-particle dose range 0 - 1.8 Gy, which is a typical shape for cell dose-response curves after alpha-particle irradiations (figure 3-11). Micronucleus formation showed a linear dose response for alpha-particle dose range 0 – 0.6 Gy (figure 3-19).

The comet assay has many advantages and has been frequently used by research groups from all over the world in the past few years. Its ability to detect DNA strand breaks or other DNA lesions that could be transformed into DNA strand breaks (such as alkali-labile sites) at the cellular level as well as its ability to distinguish single strand breaks (alkaline condition) and double strand breaks (neutral condition) make it a popular tool in areas such as radiation biology, oxidative damage and genetic toxicology (11, 15, 21).

In the comet assay studies, the electric field uniformity in the electrophoresis tank was tested first. The results suggested uniform responses from the slides along the edge of

the tank, more specifically from position '2' to '7' (see figure 3-7). These positions were used for further experiments. Then different electrophoresis times (20 mins, 40 mins, 60 mins, and 80 mins) were tested in both control groups and H_2O_2 treated groups. 40 mins was chosen to be used in further experiments because it differentiated the H_2O_2-treated groups from the control groups in a relatively short period of time.

The results of the alkaline comet assay for DU-145 cells after alpha-particle irradiation were shown in histogram and box plot. Due to the heterogeneous property of alpha-particle irradiation, the exposed cells received different numbers of alpha-particle traversals, as defined by a Poisson distribution. So the mean and standard deviation are not ideal statistical tools for results interpretation. The tail length and tail moment were chosen for their sensitivities. From the histograms, alpha-particle irradiation generated a distribution of tail length and tail moment, which shifted to higher level of damage indication as the alpha-particle dose increased. From the box plots, an increasing trend can be observed with increasing alpha particle doses. Comparing the two groups of results, tail length shows better sensitivity and linearity in dose response. Even in the control groups, some cells with long tail and large tail moment were observed. The damage of those control cells may come from the environmental factors, the handling processes, or the cells themselves, just like the concept of plating efficiency for the control cells in the clonogenic assay. Control slides were included in all experiments for background monitoring.

Although our histogram results showed a shift of tail length and tail moment as a function of average alpha-particle doses, we did not observe the bimodal distribution shown by Jostes *et al.* (16) (see figure 3-2). They used the alkaline single-cell gel technique to provide a biological estimate of the percentage of cell nuclei "hit" by alpha

particles during *in vitro* radon exposure and pointed out that the comet assay technique could be used to detect alpha-particle "hits" to cell nuclei (16) and to show both the hit and the non-hit cells in the population after a low fluence of alpha particles. One possible explanation is that they used length-width ratio as an endpoint but we used tail length and tail moment as endpoints. Different endpoint parameters could generate different results. Ideally, we should use the same "length-width ratio" parameter to compare our results to Jostes's results. However, the LACAAS Comet Assay software used in our studies did not include the "length-width ratio" as one of its eight measurement parameters (Table 3-2), which made it impractical for us to use it. In addition, the "length-width ratio" is not a commonly used parameter in the majority of the comet assay studies. The most commonly used and highly recommended parameters are tail length, tail moment and percentage DNA in tail (11, 18, 21). Another reason might come from the different cell lines used in different studies. They used the A_L cell line (figure 3-2) as well as the CHO cell line (not shown here) but we used a human prostate tumor cell line DU-145.

Meanwhile, variations were reported in the comet assay results among different research groups (11). The timing and voltage used for electrophoresis were largely empirical. Much of the variation in the reported comet assay protocols was found during electrophoresis. The desired voltage and time of electrophoresis was related to the levels of DNA damage expressed in the cells and the salt concentration of the buffer (11). A variety of fluorescent dyes such as propidium iodide, acridine orange, SYBR, YOYO, etc, different fluorescent microscopes and different image analysis systems used by different comet assay groups could all contribute to the variations. Lack of consistency among research groups is still a problem in this field.

In our come assay studies, variations among experiments conducted at different time were also observed (data not shown here). Those differences might come from slide preparation, cell sample preparation, reagent preparation, as well as the actual experimental handling and processing. Factors like the salt concentration and the volume of the electrophoresis buffer, the stability of the input voltage and the current could all affect the results. Fading of the fluorescent dye was another factor contributing to the variations. Scoring the same sample slide twice at different times could produce different results, even when the anti-fade solution was used. Lack of consistency was a problem we encountered in our comet assay experiments.

As a conclusion, the lack of standardization and automation of the procedure, the lack of sensitivity and consistency in the results, especially the fact that we could not reproduce the bimodal distribution shown by Jostes et al (figure 3-2) to differentiate the hit cells from the non-hit cells in a mixed cell population, which we based our hypothesis on, discouraged us from using the comet assay in the bystander studies described in next chapter.

References:

1. Hall, E. J. Radiobiology for the radiologist, 5th edition, p. 553. Philadelphia: Lippincott Williams & Wilkins, 2000.
2. Munro, T. R. The relative radiosensitivity of the nucleus and cytoplasm of Chinese hamster fibroblasts. Radiation Research, *42:* 451-470, 1970.
3. Hofer KG, H. C., Smith JM. Rdiotoxicity of intracellular 67Ga, 125I and 3H. Nuclear versus cytoplasmic radiation effects in murine L1210 leukaemia. Int J Radiat Biol Relat Stud Phys Chem Med, *28:* 225-241, 1975.
4. Warters RL, H. K., Harris CR, Smith JM. Radionuclide toxicity in cultured mammalian cells: elucidation of the primary site of radiation damage. Curr Top Radiat Res Q., *12:* 389-407, 1978.
5. Raju, M. R., Eisen, Y., Carpenter, S., and Inkret, W. C. Radiobiology of alpha particles. III. Cell inactivation by alpha-particle traversals of the cell nucleus. Radiat Res, *128:* 204-209, 1991.
6. Miller RC, R.-P. G., Geard CR, Hall EJ, Brenner DJ. The oncogenic transforming potential of the passage of single alpha particles through mammalian cell nuclei. Proc Natl Acad Sci U S A., *96:* 19-22, 1999.
7. Hei TK, W. L., Liu SX, Vannais D, Waldren CA, Randers-Pehrson G. Mutagenic effects of a single and an exact number of alpha particles in mammalian cells. Proc Natl Acad Sci U S A., *94:* 3765-3770, 1997.
8. Johanson, O. O. a. K. J. Microelectrophoretic study of radiation-induced DNA damages in individual mammalian cells. Biochem. Biophys. Res. Commun., *123:* 291-298, 1984.
9. N. P. Singh, M. T. M., R. R. Tice, E. L. Schneider A simple technique for quantitation of low levels of DNA damage in individual cells. Exp. Cell Res., *175:* 184-191, 1988.
10. Olive, P. L. Cell Proliferation as a requirement for development of the contact effect in the Chinese Hamster V79 spheroids. Radiation Research, *117:* 79-92, 1989.
11. Olive, P. L. DNA damage and repair in individual cells: application of the comet assay in radiobiology. INT. J. RADIAT. BIOL, *75:* 395-405, 1999.
12. Angelis, K. J., M. Dusinska and A.R. Collins Single cell gel electrophoresis: Detection of DNA damage at different levels of sensitivity. Electrophoresis, *20:* 2133-2138, 1999.
13. Wood, M. L. a. K. A. Detection of DNA Damage and Identification of UV-Induced Photoproducts Using the CometAssay Kit. BioTechniques, *27:* 846-851, 1999.
14. Morris, E. J., J.C. Dreixler, K-Y. Cheng, P.M. Wilson, R.M. Gin and H.M. Geller Optimization of single-cell gel electrophoresis (SCGE) for quantitative analysis of neuronal DNA damage. BioTechniques, *26:* 282-289, 1999.
15. Malyapa, R. S., C. Bi, E.W. Ahern, and J.L. Roti Roti Detection of DNA damage by the alkali comet assay after exposure to low dose gamma radiation. Radiation Research, *149:* 396-400, 1998.
16. R.F. Jostes, T. E. H. a. F. T. C. Single-cell gel technique supports hit probability calculations. Health Phys., *64:* 675-679, 1993.

17. Singh NP, S. R., Singh H, Lai H. Visual quantification of DNA double-strand breaks in bacteria. Mutat Res., *429:* 159-168, 1999.
18. Fairbairn, D. W., P.L. Olive, K.L. O'Neill The comet assay: a comprehensive review. Mutation Res., *339:* 37-59, 1995.
19. Fenech, M. The cytokinesis-block micronucleus technique: a detailed description of the method and its application to genotoxicity studies in human populations. Mutat Res, *285:* 35-44, 1993.
20. Shao, C., Aoki, M., and Furusawa, Y. Bystander effect in lymphoma cells vicinal to irradiated neoplastic epithelial cells: nitric oxide is involved. J Radiat Res (Tokyo), *45:* 97-103, 2004.
21. Collins, A. The comet assay for DNA damage and repair: principles, applications, and limitations. Mol Biotechnol, *26:* 249-261, 2004.

Chapter 4 Bystander Effect Studies

4.1 Introduction

It has been long accepted that the important biological effects of ionizing radiation of cells resulted from unrepaired or misrepaired DNA damage in the irradiated cells and the nucleus of a cell is the critical target of radiation. It was presumed that no biological effects would be expected in cells that receive no direct radiation. However, accumulated experimental evidence in the recent decade or so indicate that cells receiving no direct radiation can also show biological consequences from their neighboring irradiated cells. This phenomenon is called the radiation-induced bystander effect or simply the bystander effect in appropriate context and in this thesis. The bystander effect was first described by Nagasawa and Little using low doses of alpha particles and a chromosome aberration endpoint (1). Over 30% of Chinese Hamster Ovary (CHO) cells showed sister chromatid exchanges (SCE) when less than 1% of cell nuclei were actually traversed by an alpha particle. These results suggested that the "effective target" for genetic damage by alpha-particle irradiation is much larger than the nucleus or even the cell itself. Since then, the literature on the bystander effect has expanded enormously. Four years later, the phenomenon was confirmed by another group using the same endpoint (SCE) in normal human lung fibroblasts (2). Enhanced frequencies of gene mutation, micronucleus formation and apoptosis were subsequently observed in the bystander cells after alpha-particle irradiation (3-6). The bystander effect is a class of effects that differs with cell type, endpoint and in actual mechanism: reviewed in (7-9). There are at least two separate mechanisms for the promulgation of damage from irradiated cells to unirradiated neighbors. One line of evidence indicates that some bystander effects are dependent on

cell-cell contact and gap junction intercellular communication (GJIC) (6, 10). Other reports have demonstrated that irradiated cells can release a soluble factor into the medium that can cause damage in un-irradiated cells subsequently exposed to the same medium (11-15). Normal cells or tissues were used in all of these studies. There have been only a few reports of bystander effects in tumor cells. Human salivary gland tumor cells have been reported to release nitric oxide following heavy ion irradiation and that the medium from these irradiated cells can inhibit cell growth and increase micronucleus formation in an unirradiated tumor cell population (16). Using a microbeam to target helium ions to either the nucleus or the cytoplasm of individual glioma cells *in vitro*, Shao *et al.* showed that micronucleus formation in the entire population greatly exceeded the number of cells individually targeted (17, 18). Xue *et al.*, labeled the DNA of human colon adenocarcinoma cells with 5-[^{125}I]iodo-2′-deoxyuridine, and showed that the growth suppression in xenografted tumors in nude mice produced by mixing labeled and unlabeled tumor cells was much greater than could be accounted for by a direct radiation effect from the incorporated ^{125}I. The authors attributed this to an *in vivo* bystander effect (19).

These reports of bystander effects in tumor cells raise the possibility that the effect can be manipulated or exploited to increase the level of tumor cell kill during tumor radiotherapy. Two types of therapy for which the bystander effects may be of particular relevance are boron neutron capture therapy (BNCT) and Radioimmunotherapy. BNCT is a targeted radiation therapy that significantly increases the therapeutic ratio relative to conventional radiotherapeutic modalities. BNCT is a binary approach: A boron-10 (^{10}B)-labeled compound is administered that delivers high concentrations of ^{10}B to the target tumor relative to surrounding normal tissues. This is followed by irradiation with thermal

neutrons or epithermal neutrons which become thermalized at depth in tissue. The thermalized neutrons are used to "activate" the ^{10}B, with the resultant production of highly localized, high-linear energy transfer (LET) radiation. This is due to the capture of thermal neutrons by ^{10}B with the resultant fission reaction [$^{10}B + {}^{1}n \rightarrow {}^{11}B \rightarrow {}^{7}Li + {}^{4}He$ (α) + 2.79 MeV] giving rise to high-energy charged particles with short range in tissue (5–9 μm). The micro-location and differential accumulation of ^{10}B have a critical bearing on the therapeutic effectiveness of BNCT (20). Non-uniform distribution of ^{10}B and the short ranges of emitted charged particles (^{4}He and ^{7}Li) result in non-uniform irradiation. In radioimmunotherapy, the radionuclides are attached to tumor specific monoclonal antibodies and delivered to the tumor sites. Radioimmunotherapy has been most effective in blood-borne tumors where access of the antibody to the tumor cells is unimpeded (21). In solid tumors, however, radioimmunotherapy has had only limited success due largely to the problems associated with non-uniform binding of the radioimmunoconjugate to the tumor (22) and/or poor penetration of the antibody into tumor sites (23, 24). By definition, both cases create bystander cells: cells that are not directly targeted by the radiation within the solid tumor or the micrometastatic site, but are in the vicinity of the irradiated cells. Metastatic prostate cancer is refractory to conventional chemotherapy due to systemic toxicity (25). Radioimmunotherapy for metastatic prostate cancer is an area of active investigation (26-30). Promising results for alpha-emitting actinium-antibody conjugates have been reported in a human prostate carcinoma mouse xenograft model (31). A human prostate carcinoma cell line (DU-145) has been chosen for the bystander effect studies.

Two different experimental models were designed to create bystander cells for studying the bystander effect in DU-145 cells: a model that used grids to partially shield

the monolayer of cells from alpha-particle irradiation and a model that used a co-culture approach to create two separated populations of cells (hit and non-hit) in the same medium.

4.2 GRIDS MODEL

4.2.1 Materials and Methods

The grid method was first used by a group in the United Kingdom to study the unexpected increase in number of clonogenic hemopoietic stem cells transmitting chromosomal instability after alpha-particle irradiation (32). The grid used in that study was composed of interwoven brass wires with a rectangular pitch of 1.2 mm and was placed immediately below, but not touching, the dish base. In the model described here, the grid was interposed between the alpha source and the Mylar bottom to shield part of the monolayer of cells from alpha-particle irradiation. By doing so, the monolayer of cells was divided into two subpopulations: the directly irradiated cells above the opening area and the non-irradiated cells above the blocked area (see figure 4-1). When the culture was grown to confluence, the two subpopulations of cells were grown in the same medium, surrounded and touched by each other in monolayer. The non-irradiated cells worked as bystander signal recipients and were called the bystander cells in this paper. In theory, this model system could be used to study both cell-cell contact/GJIC and soluble factor mechanisms.

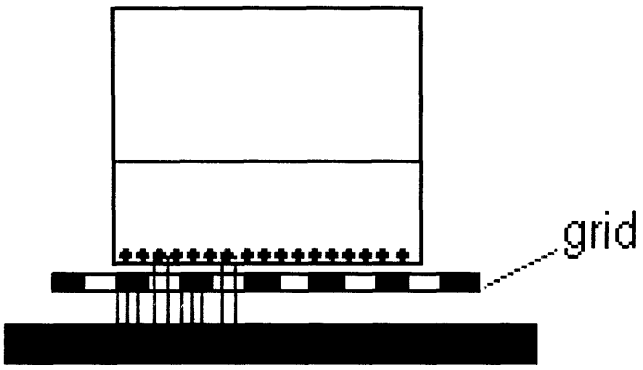

Figure 4-1. Schematic view of the grids model for the bystander effect study. A grid was used to shield part of the monolayer of cells from alpha-particle irradiation, creating hit and non-hit cells in a mixed population.

4.2.1.1 Grids design

There are two questions that need to be answered in this study: was there a bystander effect in the DU-145 human prostate tumor cells after alpha-particle irradiation? If yes, was it related to the amount of contact between the hit and non-hit cells? The answer to the second question would probably help us understand the mechanism of the bystander effect. The idea was to design and make a series of grids with different opening patterns but the same opening ratio. The same opening ratio would create the same percentage of hit cells. Different opening patterns would allow different chances of contact between the hit and non-hit cells. Since the two subpopulations of cells could only touch each other at the peripheries of the opening areas, the contact chance was proportional to the total perimeters of all the opening areas. For simplicity, the opening ratio was set to 50%. Therefore, half of the cells was subject to direct alpha-particle irradiation and would be killed if the irradiation dose was high enough. The resulting cell surviving fractions could tell if there was a bystander effect or not. In addition, the cell survival results from

grids with different opening patterns could help one understand whether or not the bystander effect was related to cell-cell contact.

The next step was to construct the grids. Commercially available woven mesh was first considered, as described in (32). But it was soon rejected because of the uneven surfaces. The alpha-particle source used in this study was an un-collimated source. Alpha particles hit the cells from all directions. The uneven surface of the mesh would introduce a discrepancy between the percentage of mesh openings and the actual percentage of hit cells. It was decided that a flat surface was essential for exposure pattern control. Due to the limitation of commercially available products, it was decided to customize the grids. Two materials were considered: stainless steel and plastics. Since there was no other requirement for the grid than shielding short range alpha particles and supporting the Mylar dish, plastic was chosen for its ease of machining.

The pattern of the openings should be homogeneous in order to produce a homogeneous response in the entire population. Two shapes of openings were considered: square and round. Since the Mylar dish had a round growing surface, the opening should also be round and radially symmetric. In addition, round openings were easier to machine than square ones. Therefore a round shape was chosen for the opening pattern.

To interpose the grid between the alpha source and the Mylar dish, a new adaptor was needed to hold the grid as close to the blades of the shutter as possible. Another stainless steel adaptor was designed and made for this purpose. There was a fringe around the working area on the grids for handling. An aluminum piece of o-ring shape of collimator was used to center the Mylar dish on the grid surface to ensure 50% opening. During the experiments, the adaptor was placed on the shutter; the grid was placed on the

adaptor; the collimator was placed around the adaptor; the Mylar dish was placed on the grid and in the middle of the collimator. There was a 1.4-μm-thick Mylar film between the top surface of the grid and the monolayer of cells.

4.2.1.2 Alpha-particle hit-pattern visualization by CR-39

The CR-39 track-etch detector was used to visualize the alpha-particle hit patterns at the cells position with the three grids. This was for the purpose of visualizing the hit pattern instead of alpha-particle flux measurement. The irradiation time was long enough to produce a clear hit pattern on CR-39. In the experiment, one of the grids was placed on the specially designed adaptor; the Mylar dish containing a piece of custom-cut CR-39 was placed on the grid and the CR-39 was irradiated at the cell position. The irradiation time was 0.5 s with grid A, 5 s with grid B and 30 s with grid C. After the irradiation, the CR-39 was processed by chemical etching in 7 N NaOH at 90 °C for 50 minutes to visualize the alpha-particle tracks.

4.2.1.3 Dosimetry

In order to determine the dose rate delivered to the cells above the opening areas of the three grids, dosimetry was carried out using the same methods described in Chapter 2. Briefly, the energy spectra were measured at the exposed cell position. The LET spectra were generated from the energy spectra by converting the energy in each channel of the energy spectrum into a corresponding LET value using the ASTAR program. The weighted-average LET was calculated from the LET spectrum using the alpha-particle counts per channel as the weighting factor. The alpha-particle flux at the exposed cell position was measured using the "track-etch" technique. The CR-39 was irradiated for 0.5 seconds with grid A, 5 seconds with grid B and 30 seconds with grid C. The irradiation

time was chosen to generate a countable number of tracks in the exposed areas with statistical significance. Images of the etched tracks were recorded in a square area of 1.03 mm^2 using a CCD camera at 50× magnification. The image area was calibrated by using a stage micrometer at the same magnification. The track images were printed and the track numbers were scored in 20 random fields for grid A and grid B, and in 10 random fields for grid C due to the large number of tracks per field (more than 1300 tracks). The PIPS detector was also used to measure the alpha-particle flux in the exposed areas with the pinhole method described in Chapter 2. The results from the two different methods were compared.

The average absorbed dose rate to the exposed cells on the Mylar surface was calculated by multiplying the alpha-particle fluence N by the average LET in the cells, and by the appropriate conversion factors: Dose (Gy) = N×S×0.016. The alpha-particle dose to the non-hit cells was zero.

4.2.1.4 Cell irradiation with grids

The clonogenic assay, as described in Chapter 3, was used to determine the cell surviving fraction after alpha-particle irradiation with different grids. Briefly, about 5×10^5 DU-145 cells were plated into pre-coated Mylar dishes and grown to confluence. The medium was changed half an hour before the irradiation. The cells in the Mylar dishes were irradiated with alpha particles using one of the three grids for graded periods of time. The irradiation dose to the exposed cells was calculated by multiplying the irradiation time by the corresponding dose rate for each case. Following the irradiation, the cells were trypsinized (0.25% trypsin with 0.1% EDTA at 37 °C for 3 min), re-suspended with full growth medium and plated into 100 mm Petri dishes for colony formation assay. The

medium was changed once after 5 days of growth. After 10 days of growth, the colonies were washed with phosphate buffered saline (PBS), fixed with 95% ethanol, and stained with 1% methylene blue aqueous solution. The colonies that contained 50 or more cells were counted. Five replicate dishes were scored per dose point in each experiment. The surviving fractions were normalized to the corresponding plating efficiencies. The data from four independent experiments were combined and plotted as mean ± standard deviation in log scale.

4.2.2 Results

4.2.2.1 Grids design

Three grids were designed. Grid A had only one hole, which provided the minimum amount of contact between the hit and the non-hit cells. Grid C had as many holes as practically possible (555) in order to provide the maximum amount of contact. Grid B was designed with the number of holes between grid A and grid C (211), to provide the amount of contact somewhere in the middle (see figure 4-2). The grids were manufactured by QC Drilling Inc. (Salem, NH). The material was clear Lexan. The thickness of the grids was 2.36 mm. The detail information for the three grids is shown in table 4-1.

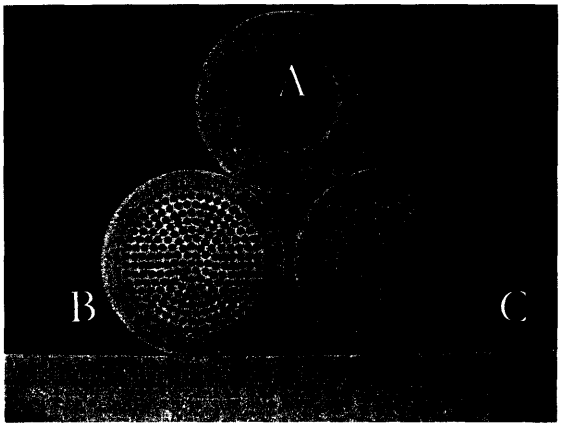

Figure 4-2. The three grids designed for the bystander study. They had different numbers of homogeneously distributed holes, giving 50% opening ratios in the 11.4 cm^2 round area. There is a milled groove with 4.13 cm diameter around the opening area, to define the periphery of the Mylar dish bottom.

Grid No.	Number of holes	Diameter of holes (cm)	Total perimeters (cm)	Total opening area (cm^2)	Percentage of open area
A	1	2.6924	8.4582	5.7	50%
B	211	0.1854	122.9106	5.7	50%
C	555	0.1143	199.2884	5.7	50%

Table 4-1. Detailed information of the three grids designed for the bystander study.

4.2.2.2 CR-39 track-etch detection

The picture of the three etched CR-39 detectors exposed to the alpha-particle irradiation with grids A, B and C and the picture of the etched dots above one hole of grid C are shown in figure 4-3. The etched patterns on the CR-39s (left) replicated the opening patterns of the three grids.

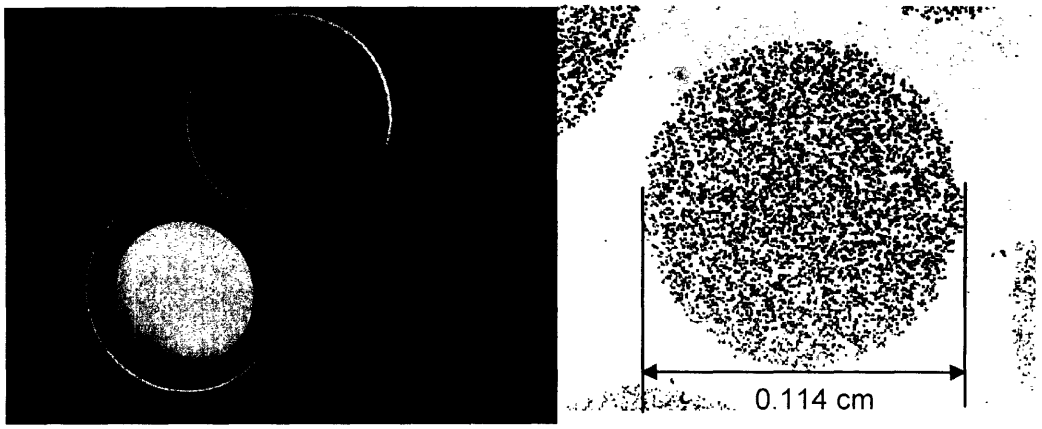

Figure 4-3. Left: the CR-39 track etching results for grid A, B and C after alpha-particle irradiation. Right: the image of the etched tracks above one hole of grid C. The images of the etched tracks were recorded in a square area of 1.03 mm^2 using a CCD camera at 50× magnification. The sparse dots in the blocked area were believed to come from environmental radiation during the processing of the CR-39. A control CR-39 was used to detect the background and showed sparse dots on it. The image is not shown here.

4.2.2.3 Dosimetry

The energy spectra with and without the grids measured by the PIPS detector are shown in figure 4-4. The converted LET spectra are shown in figure 4-5. The energy and LET spectra with the grids in place were narrower and more symmetric due to the collimation effect of the grids (figure 4-6). Table 4-2 compares the alpha-particle flux results from the PIPS detector and the CR-39 track-etch detector with and without the grids. The reasons for the significant discrepancy for the #4 source without grid were explained in Chapter 2 (2.3.2.2). Consistent results between the PIPS detector and the CR-39 detector were observed from the #4 source with grids A, B and C due to the collimation effects and longer exposure time (0.5 s, 5 s, and 30 s). Meanwhile, different extents of collimation effects reduced the alpha-particle flux significantly from grid A to grid C. The

alpha-particle fluxes measured with the PIPS detector were used for dose rate calculation in all cases. All dosimetry results are shown in table 4-3.

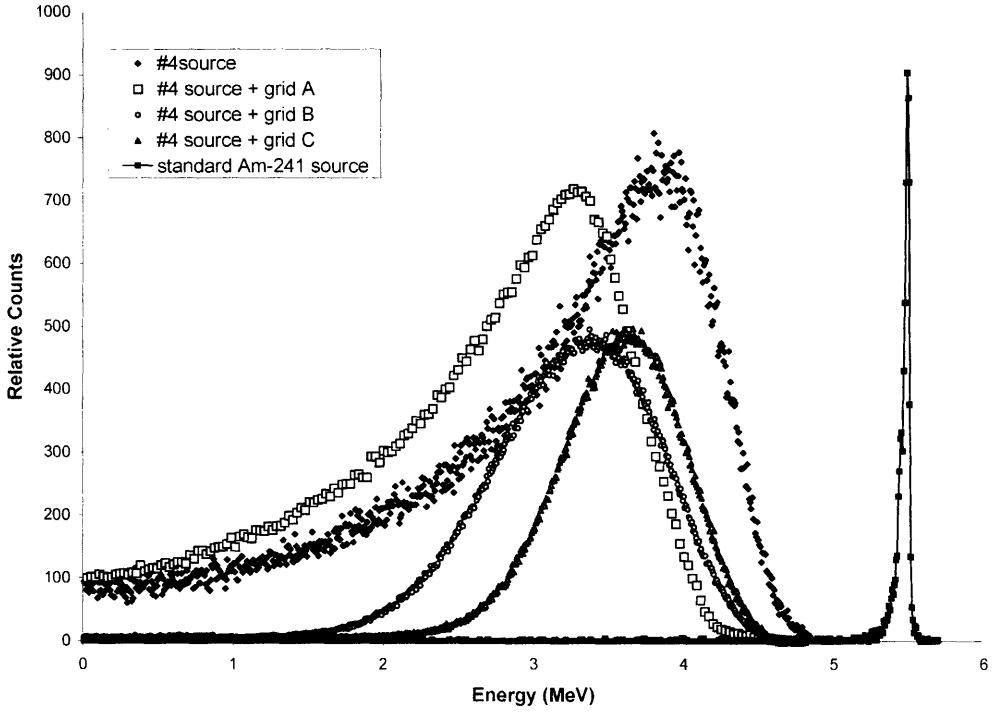

Figure 4-4. The energy spectra at the cell position for the #4 source with and without grids. The energy spectrum of a standard Am-241 alpha source in a vacuum was used to calibrate the energy scale on the x-axis, as described in Chapter 2. The different extents of narrowed shapes for grid A, B and C came from the collimation effects of different sizes of holes (figure 4-6), which cut off the low energy tails of the spectra. The y-axis represents relative counts of alpha particles in different energy channels.

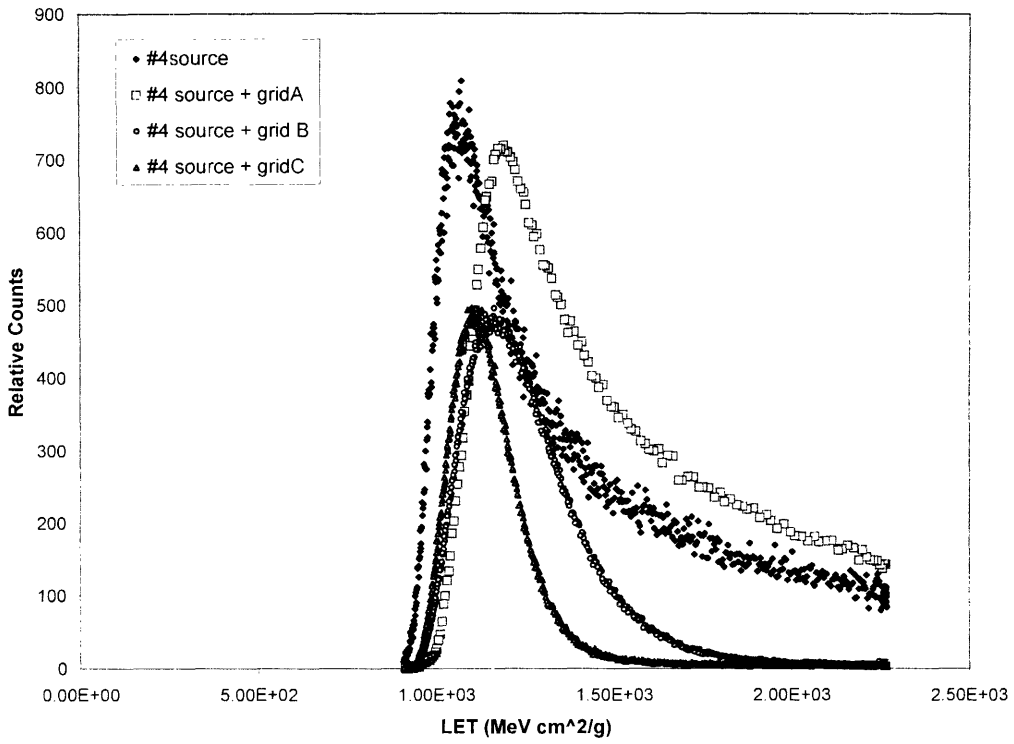

Figure 4-5. The LET spectra at the cell position for the #4 source with and without grids. The collimations effects from different sizes of holes are also reflected in the narrowed shapes of the LET spectra, resulting in more symmetric peaks and reduced high-LET tails.

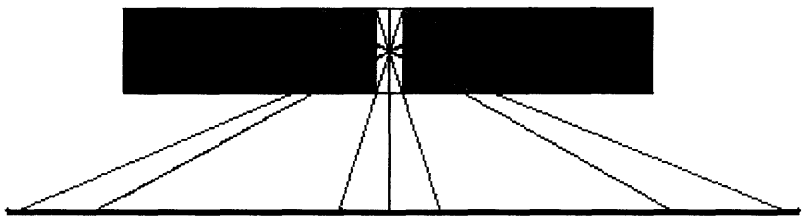

Figure 4-6. Schematic view of the collimation effects from different sizes of holes in the three grids. Smaller holes would block more alpha particles with large incident angles and therefore reduce the low energy and high LET tails in the spectra, resulting in a narrower and more symmetric spectrum, as well as reduced alpha-particle flux.

	#4 source	#4 source + grid A	#4 source + grid B	#4 source + grid C
Exposure time for CR-39	0.2	0.5	5	30
Alpha-particle flux (CR-39)	1440.3 ± 70.2	1047 ± 102	100.4 ± 4.6	43.8 ± 0.6
Alpha-particle flux (PIPS)	998 ± 20	900 ± 18	94 ± 1.9	45 ± 0.9

Table 4-2. Comparison of the alpha-particle flux results between CR-39 track-etch detector and PIPS detector. The errors of the CR-39 results are the standard deviation from counts in 20 fields. The errors of the PIPS results came from the reproducibility of the measuring system. For the #4 source without grid, the PIPS result is significantly smaller than the CR-39 result. For the #4 source with grids A, B, and C, the results from the two detectors are consistent.

	#4 source	#4 source + grid A	#4 source + grid B	#4 source + grid C
Media that alpha particles pass through	5 mm air 1.4 μm Mylar	7.66 mm air 1.4 μm Mylar	7.66 mm air 1.4 μm Mylar	7.66 mm air 1.4 μm Mylar
Alpha-particle flux (counts/mm^2 · s)	998 ± 20	900 ± 18	94 ± 1.9	45 ± 0.9
Average energy (MeV)	3.14 ± 0.06	2.81 ± 0.06	3.71 ± 0.07	3.76 ± 0.07
Average LET (MeV· cm^2/g)	1266.1 ± 63.3	1353.5 ± 67.7	1098.4 ± 54.9	1089.1 ± 54.5
Average dose rate to cells at open areas (Gy/min)	1.21 ± 0.07	1.17 ± 0.06	0.094 ± 0.005	0.047 ± 0.003

Table 4-3. Dosimetry results for the #4 source and the #4 source with and without the grids. The media that alpha particles passed through were different for the #4 source alone and the #4 source with grids due to the thickness of the grids and the different designs of the adaptors. The alpha-particle flux results came from the PIPS detector. The weighted average energy was calculated from the energy spectra in figure 4-4. The weighted average LET was calculated from the LET spectra in figure 4-5. The average dose rate was calculated from the equation: Dose rate = (average LET) × (alpha-particle flux) × 0.016.

4.2.2.4 Cell irradiation with grids

The cell survival curves for the #4 source with and without grids are shown in figure 4-7. The survival curve for the #4 source itself is a straight line from the origin on a log scale. The surviving fractions for the #4 source with grid A and grid B decline at lower doses and flatten at 50% SF at higher doses. The surviving fractions with grid C decline at lower doses and the means of the SF fall below 50% at higher doses (44 ± 1.7 % at 2.8 Gy and 43 ± 6.1 % at 3.3 Gy).

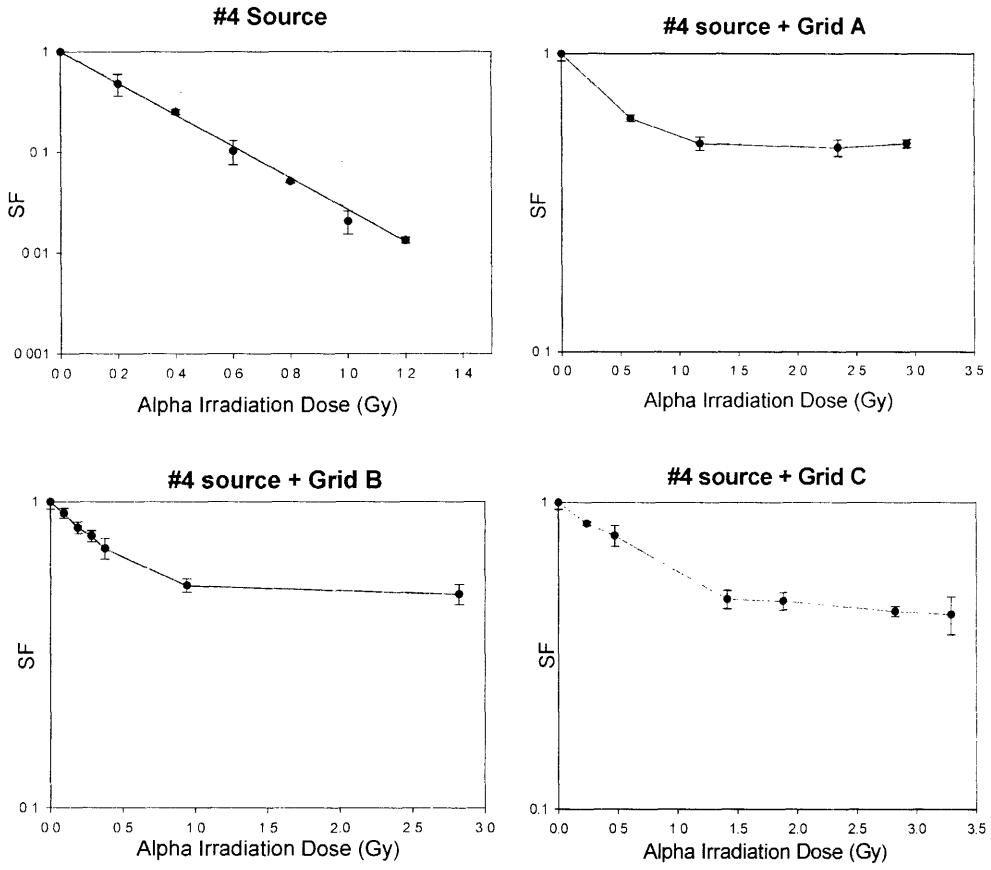

Figure 4-7. The survival curves of the DU-145 cells after alpha-particle irradiations using the #4 source with and without grids. The measurements were done on the mixed populations of hit cells and non-hit cells. The x-axis represents the alpha dose to the hit cells. The y-axis is on a log scale and represents the surviving fraction of the mixed cells in the Mylar dish.

4.2.3 Discussion

For grid A and grid B, the cell survival curves reached plateaus at about 50% survival fractions when the doses were high enough to kill essentially all the hit cells. It means that all the non-hit cells survived and no bystander effect was detected. In the case of grid C, some cell survivals fell below 50% at high doses, suggesting that some of the non-hit cells were killed. In other words, some of the cells receiving no direct alpha-particle irradiation died from a bystander effect. However, due to the large error bar at 3.3 Gy (43 ± 6 %), the effect was not statistically significant.

The advantage of this method is that the hit cells and the non-hit cells touched and mixed with each other in the same medium, which is a two-dimensional model for the real situation in radioimmunotherapy. Another advantage is that it allowed the detection of the effects of both GJIC and soluble factors.

But there are also some problems associated with this method. In the original plan, the comet assay would be used for the grid results analysis. The hypothesis was that if the histogram of comet assay results could separate the hit cells from the non-hit cells as demonstrated by Jostes *et al.* (33), then it might be able to distinguish the bystander cells as well. But our trial of the comet assay in the direct alpha-particle irradiation failed to reproduce the histogram showed by Jostes *et al.* Because the comet assay did not give us the expected high resolution, as required for the bystander study, the clonogenic assay was used instead. The resolution of the clonogenic assay was still not good enough to detect the bystander effect; the large error bar at 3.3 Gy makes it hard to draw any conclusion regarding the bystander effect although there is a trend that surviving fraction at high doses falls below 50%. Another issue is that even though there were 50% open areas in the three

grids, the proportion of cells that was exposed to the alpha-particle irradiation was not exactly 50%. The reason is that for those cells lying on the circumference of the openings, half of their nuclear areas were exposed to alpha-particle irradiation and half were blocked on average. But a cell is considered to be irradiated no matter what percentage of the cell body or cell nucleus is exposed to irradiation. So, all the cells lying on the circumference of the openings were actually irradiated. In other words, the 50% opening actually resulted in more than 50% of cells exposed to the alpha particles. For grid A, the effect was negligible. The longer the total circumference is, the more extra cells were exposed than the theoretical 50%. Therefore, the increased cell killing with grid C might result from the increased cell exposure at the edges of the openings.

4.3 CO-CULTURE MODEL

4.3.1 Materials and Methods

4.3.1.1 The co-culture system

While the grids model mixed the hit and non-hit cells together, allowing for both GJIC and soluble factor detection, a co-culture system was designed to create a separate population of non-irradiated DU-145 cells that shared the same medium as the directly irradiated cells on the Mylar membrane, but were well beyond the range of the alpha particles coming from the ^{241}Am foil (figure 4-8). The non-irradiated cells were grown on a Snapwell insert (item # 3407, Corning Life Sciences, Corning, NY). The Snapwell insert contains a 12 mm diameter tissue culture-treated polycarbonate membrane with 0.4 μm pores to allow passage of small diffusible molecules, supported by a detachable ring (figure 4-9). The detached insert was placed in the Mylar dish facing down, creating ~ 4

mm distance between the polycarbonate membrane bottom of the insert and the Mylar bottom of the dish, well beyond the maximum range of the alpha particles in the medium (< 80 μm). At least 6 ml medium was needed to cover the bottom of the insert. We define the directly-irradiated cells growing on the Mylar membrane as the "targeted cells", and the non-irradiated cells growing on the Snapwell insert as the "co-cultured cells". The co-culture system excluded the cell-cell contact or GJIC factors and only allowed for effects caused by soluble factors. Similar systems were also used by several other groups for soluble factor focused bystander studies (15, 34-36).

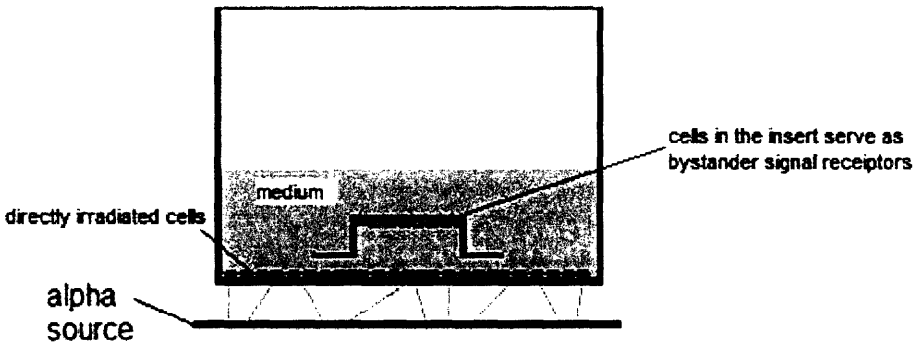

Figure 4-8. The co-culture system for the bystander effect study. The cells growing on the Mylar bottom were defined as the "targeted cells"; the cells growing on the Snapwell insert were defined as the "co-cultured cells", which were 4 mm above the targeted cells and worked as the receptor of the soluble bystander signal from the targeted cells.

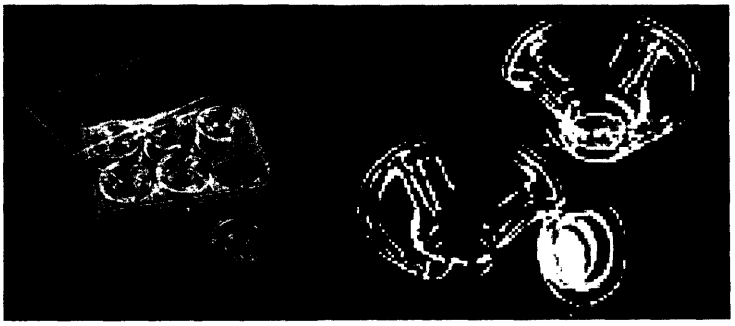

Figure 4-9. The Snapwell insert used in the co-culture system from Corning Life Sciences.

4.3.1.2 Co-culture experiments

For the co-culture experiments, ~ 5×10^5 DU-145 cells were seeded in the Mylar dish (3.81 cm diameter, 11.4 cm^2 growth area) and ~ 5×10^4 cells were seeded in the Snapwell insert (12 mm diameter; 1.13 cm^2 growth area). The cells were allowed to attach overnight. On the day of the irradiation experiment, 6 ml of fresh medium was replaced in each Mylar dish. The Snapwell inserts were detached from the support rings with a sterile tweezers and placed upside down in the medium inside the Mylar dishes. The Mylar dishes were then placed on the alpha-particle irradiator and the bottom layer of cells was irradiated with graded alpha-particle doses at room temperature. After the irradiation, the Mylar dish together with the insert was put back into the incubator and co-incubated at 37 °C for 2 hrs (24 hrs in some case). After the co-incubation, the insert was taken out of the Mylar dishes and the cells in the insert were collected by trypsinization and processed for the micronucleus assay as described in Chapter 3 (3.2.4 Micronucleus assay). The control was handled in the same way except that the Mylar dish with the insert was not placed in the alpha-particle irradiator for the irradiation.

4.3.1.3 Medium only irradiation

To check the effect of medium only irradiation on the co-cultured cells, the insert with cells was placed into the Mylar dish without cells growing on the bottom. The Mylar dish together with insert was placed on the irradiator and the full growth medium containing 14% serum was irradiated for 1 min. The cells on the insert were then processed in the same way as the co-culture experiments described above.

4.3.1.4 Medium transfer experiments

For the medium transfer experiments, DU-145 cells growing on the Mylar membrane in the Mylar dish were irradiated for 1 min. Medium from the irradiated cells (0.8 ml) was transferred to a centrifuge tube with filter (Costar-8160, Spin-x centrifuge tube filter, 0.22 μm cellulose acetate in 2.0 ml polypropylene tube). The tube was centrifuged at 2000 rpm for 1 min to remove any cells and debris from the medium. The filtered medium was then used to replace the medium in an insert with unirradiated DU-145 cells. The whole filtration and medium transfer procedure took 2-3 min. The cells in the insert were incubated in the filtered medium for 2 hrs before they were trypsinized and processed for the micronucleus assay.

4.3.1.5 Co-culture after irradiation experiments

For the co-culture after irradiation experiments, DU-145 cells growing on the Mylar membrane were irradiated for 1 min without the presence of the insert. The Snapwell insert with cells was placed upside down into the growth medium above the irradiated cells immediately (~ 1 min) after the irradiation. Then the cells in the insert were incubated in the irradiated medium above the irradiated cells at 37 °C for 2 hrs before they were trypsinized and processed for the micronucleus assay.

4.3.1.6 Scavenger experiments

Two chemical radical scavengers were tested in the scavenger experiments. Dimethyl sulfoxide (DMSO, Sigma-Aldrich, St Louis, MO) is a hydroxyl radical (OH·) scavenger. It was added to the medium in the Mylar dish at a final concentration of 1% 10 minutes before the irradiation. PTIO (2-phenyl-4,4,5,5-tetramethylimidazoline-1-oxyl 3-

oxide; Sigma-Aldrich, P5084) is a nitric oxide radical (NO·) scavenger. It was added to the medium in the Mylar dish at a final concentration of 100 μM 10 minutes before the irradiation. Other procedures were the same as the co-culture experiments. The scavengers were present in the medium during the irradiation and the subsequent 2-hr incubation. The co-cultured cells were then harvested and processed for the micronucleus assay.

4.3.2 Results

4.3.2.1 Dose response results

Alpha-particle irradiation of the cells on the Mylar membrane produced a significant increase in the MN/BN ratio in the co-cultured cells on the Snapwell insert. Figure 4-10 shows the MN/BN ratios for these co-cultured cells as the alpha-particle dose delivered to the cells on the Mylar membrane was increased from 0 to 6.0 Gy. The baseline MN/BN ratio in control DU-145 cells was 10.0 ± 1.0% (figure 4-10). The increased incidence of MN formation in the co-cultured cells was statistically significant relative to the control cells ($p < 0.0001$) at all alpha-particle doses delivered to the targeted cells. Though the differences in the magnitude of the bystander effect as a function of the alpha-particle dose to the targeted cells are only marginally significant, there is a trend for the bystander effect to increase rapidly, level off, and then decrease at the highest dose delivered to the targeted cells (see figure 4-10). The MN/BN ratio in the co-cultured cells was greater at 0.6 Gy than at 0.1 Gy ($p = 0.041$). The effects at 0.6 Gy and 1.2 Gy were not different. The effect at 6.0 Gy was less than the effect at 1.2 Gy ($p = 0.028$). The percentage of bi-nulceated cells (%BN) observed in the co-cultured cells, after a 1.2 Gy alpha-particle exposure to the targeted cells (figure 4-10, "1.2 Gy"), was 81 ± 3.7%, which is essentially the same as the %BN observed in the control population 82 ± 0.1%. These

data for the %BN cells present after the cytochalasin-B block procedure were derived from two independent samples from each population and suggest that there was no significant change in cell cycle time in the co-cultured cells, or in the ability of the co-cultured cells to progress through the cell cycle, relative to the control cells.

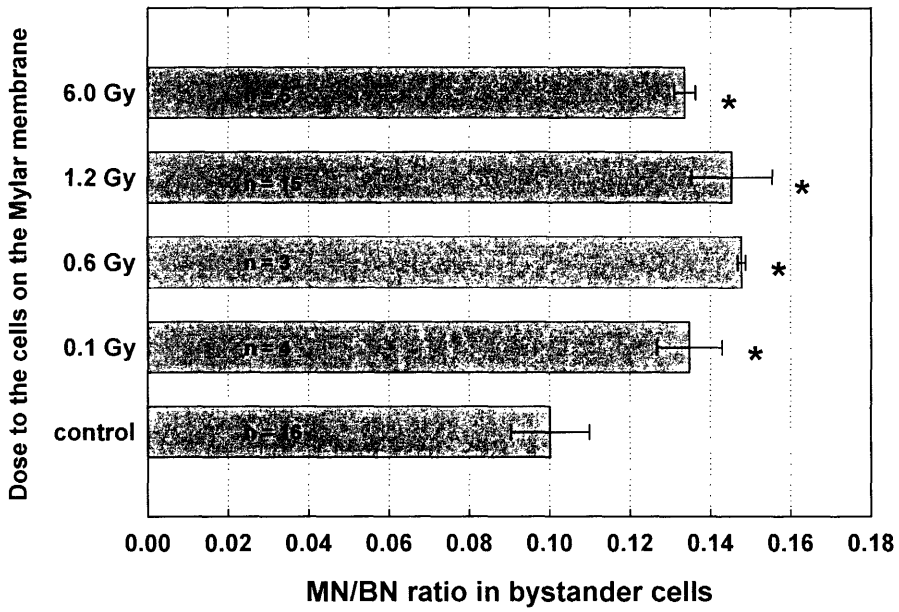

Figure 4-10. Micronucleus formation in the co-cultured DU-145 cells as a function of direct alpha-particle doses. The co-cultured cells were incubated in the medium above the irradiated cells for 2 hrs after the irradiation. The control produced 10.0 ± 1.0% MN/BN ratio; 0.1 Gy produced 13.5 ± 0.8% MN/BN ratio; 0.6 Gy produced 14.8 ± 0.1% MN/BN ratio; 1.2 Gy produced 14.5 ± 1.0% MN/BN ratio; 6.0 Gy produced 13.4 ± 0.3% MN/BN ratio. The numbers within the shaded bars indicate the number of replicate experiments; 1000-2000 BN cells were scored for each experiment. (*) $p < 0.0001$ relative to controls.

4.3.2.2 Medium-irradiation, medium-transfer experiments and other experiments

To further examine the nature of the soluble factor released into the medium and affecting the co-cultured cells, a series of medium-transfer, medium-irradiation and other experiments were carried out. Figure 4-11 shows the MN/BN ratio in the co-cultured cells

as a function of these various treatments. As a reference, the baseline MN/BN ratio in the control cells and the MN/BN ratio in the co-cultured cells from the experiments where the targeted cells received 1.2 Gy are both reproduced from figure 4-10 and labeled as "Control" and "1.2 Gy to targeted cells, co-cultured cells present, then co-incubate for 2 hr " in figure 4-11.

For the experiments shown in figure 4-10, the co-cultured cells on the insert were present during the irradiation of the targeted cells, and were then co-incubated in the same medium above the irradiated cells for an additional 2 hrs before trypsinization and processing for MN analysis. Co-incubation of the cells on the insert for 24 hrs after the exposure of the targeted cells to 1.2 Gy of alpha particles produced a similar bystander effect. The MN/BN ratio in the co-cultured cells was 15.2 ± 2.2% (n=6) with the 24-hr co-incubation compared to 14.5 ± 1.0% (n = 15) in the cells with the 2-hr co-incubation.

For the experiments shown in figure 4-10, the co-cultured cells on the insert were *present* in the medium above the targeted cells *during the irradiation.* When the insert with the co-cultured cells was placed into the medium above the targeted cells on the Mylar membrane immediately (within 1 min) *after the irradiation*, and then co-incubated at 37 °C for 2 hrs, there was no significant increase in the MN/BN ratio in these co-cultured cells relative to the controls. Delivery of 1.2 Gy to medium-alone (no cells on the bottom Mylar membrane) produced no significant increase in the MN/BN ratio in the co-cultured cells. In a separate medium-transfer experiment, the targeted cells received 1.2 Gy and, within ~ 3 min, the medium above these cells was removed, filtered, and added to a well with unexposed DU-145 cells on a Snapwell insert. These cells on the insert were then

incubated at 37 °C for 2 hrs in this filtered medium. The MN/BN ratio in these cells exposed to the irradiated medium was 11.0 ± 0.6%.

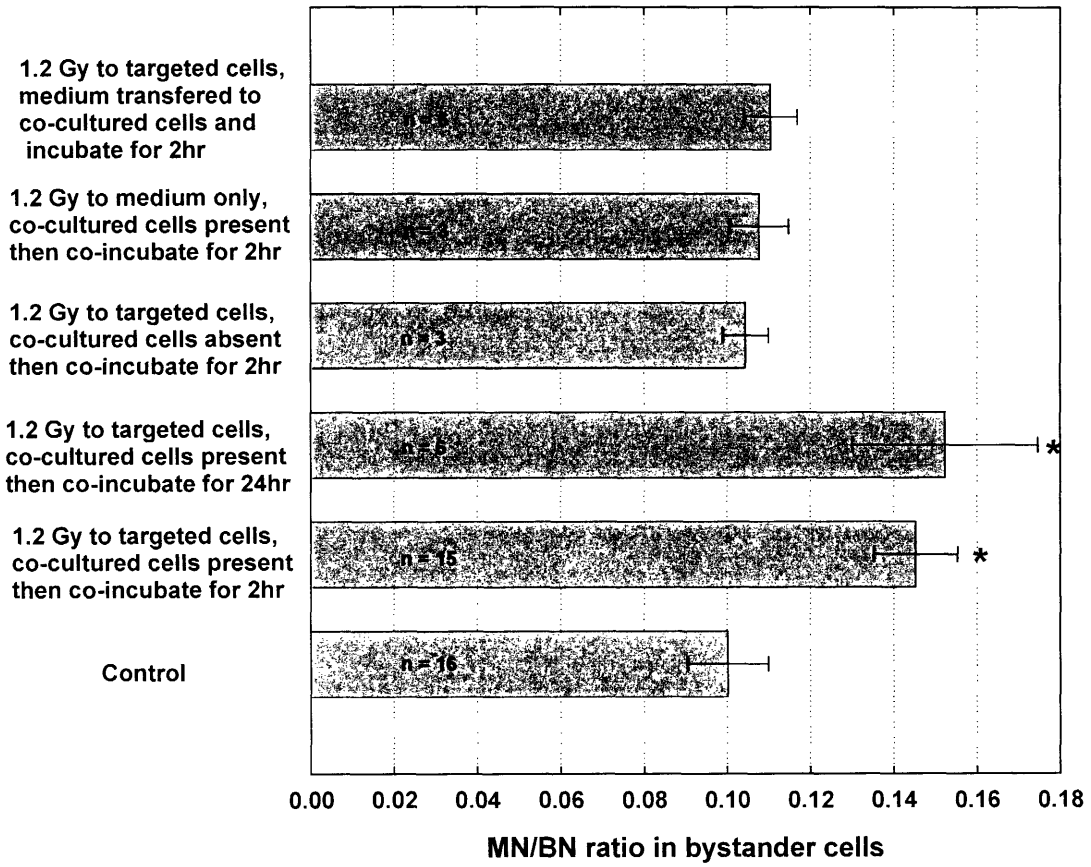

Figure 4-11. Micronucleus formation in the co-cultured cells following various treatments: "1.2 Gy to targeted cells, co-cultured cells present, then co-incubate for 2hr" is the core experiment replicated from figure 4-10 and produced 14.5 ± 1.0% MN/BN ratio; 24 hr co-incubation after irradiation instead of 2hr co-incubation produced 15.2 ± 2.2% MN/BN ratio in the co-cultured cells; When the co-cultured cells were absent during the 1.2 Gy irradiation of the targeted cells but added to the medium after the irradiation and then co-incubate for 2hr, the MN/BN ratio was 10.4 ± 0.6% in the co-cultured cells; 1.2 Gy to medium alone irradiation produced 10.8 ± 0.7% MN/BN ratio in the co-cultured cells; the filtered medium from irradiated cells produced 11.1 ± 0.6% MN/BN ratios in the co-cultured cells. In all experiments the co-cultured cells were incubated for 2 hrs after the irradiation. (*) $p < 0.0001$.

4.3.2.3 Scavenger experiments

The experimental design, with the co-cultured cells beyond the range of the alpha particles, measures a bystander effect mediated by a soluble factor(s) released into the medium by the irradiated cells. Experiments were carried out with added radical scavengers in an effort to provide more information on the nature of this medium-mediated bystander effect. Figure 4-12 shows the MN/BN ratio for the co-cultured cells in the radical scavenger experiments. As a reference, the background MN/BN ratio in the co-cultured cells and the MN/BN ratio in the co-cultured cells when the targeted cells received 1.2 Gy are also reproduced from figure 4-10. When the targeted cells received 1.2 Gy of alpha-particle irradiation in the presence of DMSO (1% vol/vol), the MN/BN ratio in the co-cultured cells dropped from 14.5 ± 1.0% to 10.5 ± 1.2% (n = 6), a level not different than the controls. The presence of 100 μM PTIO did not decrease the MN/BN ratio significantly in the co-cultured cells when the targeted cells received 1.2 Gy of alpha-particle irradiation. Neither DMSO alone nor PTIO alone had any effect on the MN/BN ratio compared to the controls (figure 4-12).

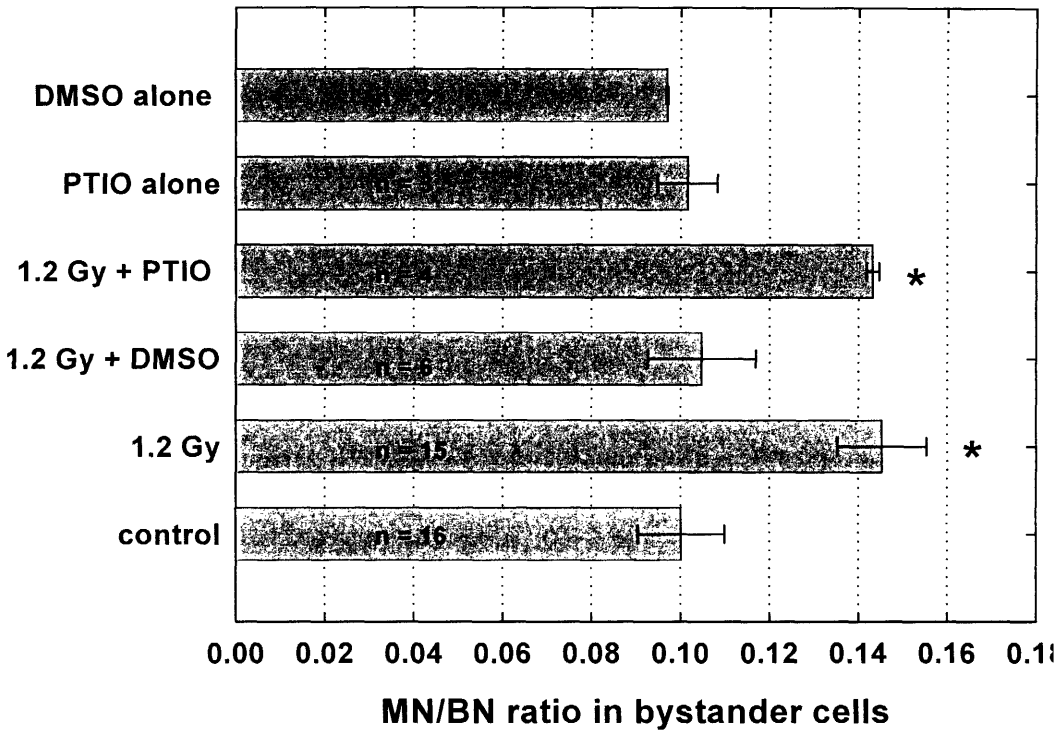

Figure 4-12. The effect of radical scavengers on the bystander effect. MN/BN ratio in the co-cultured cells following irradiation of the targeted cells in the presence of radical scavengers added to the medium 10 min before the irradiation and maintained in the medium during the 2-hr incubation after the irradiation. DMSO was used at a concentration of 1% (vol/vol). PTIO was present at a concentration of 100 μM. DMSO alone produced 9.7 ± 0.02% MN/BN ratio; PTIO alone produced 10.2 ± 0.7% MN/BN ratio; DMSO plus 1.2 Gy produced 10.5 ± 0.1% MN/BN ratio; PTIO plus 1.2 Gy produced 14.3 ± 0.1% MN/BN ratio. (*) $p < 0.0001$ relative to controls.

4.3.3 Discussion

Experimental approaches for the study of bystander effects fall into three main categories: 1) irradiation of cells with very low fluences of broad beams of ions where Poisson statistics predict the fraction likely to sustain a direct hit; 2) the use of accelerator-based microbeams for targeting individual cells or a fixed percentage of cells in a

population; and 3) co-culture or medium transfer experiments where two populations of cells share the same medium, either simultaneously or at different times, but only one population is directly irradiated. The results reported here fall into the third category and the discussion will focus primarily on this class of bystander effect studies. For each of these experimental approaches, the use of different endpoints, the use of different cell lines, the use of different types of radiation, and variations in the experimental procedures, have produced a wide variety of, sometimes conflicting, bystander effect results. The use of normal cell lines in the majority of the alpha-particle-based bystander effect studies is relevant to the radiation protection and risk assessment scenario, in light of the fact that >50% of average annual effective dose to the US population is delivered by alpha particles from the decay of radon daughter products in the lung (polonium, bismuth and lead). For average residential radon exposures, the alpha-particle fluence in the lung is extremely low. With the reports of *in vitro* bystander effects at low alpha-particle fluence, many investigations have focused on the question of whether risks associated with radon exposures are underestimated (37-39). The focus of the study here is somewhat different than the majority of the bystander effect literature: it studied the bystander effects in tumor cells and modeled the use of alpha particles for tumor therapy. With targeted alpha-particle therapies for solid tumors or micrometastatic disease, such as the use of monoclonal antibodies bearing alpha-emitting radionuclides, or of ^{10}B-containing drugs used for boron neutron capture therapy *(40)*, a non-uniform delivery of the targeting agent results in a heterogeneous delivery of alpha particles at the cellular level, with the bystander cells being the ones that escape direct alpha-particle traversals. A 3-D tumor site will be exposed to alpha particles of all energies and residual ranges during targeted alpha-particle

therapy. The spectrum of different energies will generate a corresponding distribution of LET values as the alpha particles slow down. The uncollimated alpha-particle irradiator described here has been simplified considerably compared to other isotopic alpha-particle sources described in the literature, e.g., (41-43). This is in keeping with the experimental objective of these studies: the focus is on the non-hit, co-cultured cells growing on an insert, the targeted cells receive distributions of alpha-particle energies and LETs that are more reflective of the actual situation during targeted alpha-particle therapy of solid tumors or micrometastases.

It is reported here the use of an experimental system that creates two populations of cells co-cultured in the same medium, only one of which is directly exposed to alpha-particle irradiation. The experimental results suggest that DU-145 human prostate carcinoma cells irradiated with alpha particles release a medium-soluble factor that is capable of causing micronucleus formation in the non-irradiated co-cultured cells. Scavenger experiments indicated that the bystander signal was not nitric oxide: the nitric oxide scavenger PTIO did not decrease the effect. The signaling factor has an effective life-time of less than 1 minute: the co-cultured cells had to be present during the irradiation to exhibit the increase in micronucleus formation. The signal is derived from irradiated cells: irradiation of medium-alone had no effect on the co-cultured cells. The approach of using a co-culture system described in this chapter is similar to that used by others (14, 15, 34, 44), and is designed to detect a bystander effect mediated by soluble factors transmitted through the medium, without the possible added complication of gap-junction intercellular communication (GJIC). Although GJIC, which plays an important role in the regulation of growth, differentiation and apoptosis in normal cells, has been shown to be required for

expression of bystander effects in fibroblasts (45) and in V79 cells (10), the role of GJIC in tumor cells is quite different. Most tumor cells have dysfunctional GJIC; some tumor promoters and oncogenes inhibit GJIC; and therapeutic approaches are being investigated to reverse the down regulation of GJIC in tumor cells (46).

Two common features of many bystander effect reports are that the magnitude of the effect is limited and that the bystander effect in the non-targeted cells either increases rapidly at low doses but saturates with increasing dose to the targeted cells or is independent of the dose administered to the targeted cells (2, 15, 35, 47). In this study, the maximum incidence of MN formation in the co-cultured DU-145 cells reached a level that was ~50% greater than the baseline incidence seen in control cells. This same level of MN formation could be produced in the targeted cells by a direct alpha-particle dose of 0.06 Gy (figure 3-18). Similar results have been reported for AGO1522 human fibroblasts co-cultured above cells irradiated with 250 kVp X rays (15). These authors reported that MN incidence, $p21^{Waf1}$ induction, and γ-H_2AX foci formation, were all increased approximately two-fold in the co-cultured cells, and that the increase was independent of the dose delivered to the targeted cells. The magnitude of the bystander effect was approximately equivalent to 0.1 Gy of direct X-irradiation (15). Using sister chromatid exchange (SCE) in a normal human lung fibroblast cell line, and alpha particles from a planar ^{238}Pu source, Lehnert *et al.* reported that the magnitude of a medium-transfer bystander effect was about the same as that observed in cells directly irradiated with an alpha-particle dose of 0.084 Gy (11). Damage in bystander cells may not always be directly comparable to the damage in the directly-irradiated cells with the use of a more discriminating endpoint. For example, Huo *et al.* analyzed the molecular structure of HPRT mutations observed in CHO cells

exposed to low fluences of ^{238}Pu alpha particles and reported that the DNA damage in bystander cells consisted primarily of point mutations, whereas, in the directly-hit cells, there was a significantly greater fraction of partial or total gene deletions. These authors suggested that the different effects observed in bystander cells compared to the cells directly traversed by an alpha particle may be caused by different agents or by different mechanisms (48).

It is reported here that alpha-particle irradiation of complete, serum-containing medium alone (no cells irradiated on the Mylar membrane) produced no bystander effect in the co-cultured cells. The role of irradiated medium has been the subject of a number of studies: the results are contradictory, but the use of different cell lines and different endpoints make direct comparisons difficult. Lehnert *et al.* have demonstrated that alpha-particle irradiation of complete medium did cause a bystander effect (SCE) in normal human diploid lung fibroblasts when transferred to unirradiated cells, and that the serum component of the medium was an absolute requirement for a positive bystander effect (2, 11, 49, 50). Suzuki *et al.* reported that alpha-particle irradiation of medium-only caused no increase in chromosome aberrations in co-cultured human-hamster hybrid (AL) cells (14). Using a co-culture system with bystander cells on an insert, Yang *et al.*, reported that X-irradiation of complete medium alone caused no bystander effects (MN formation, p21^{Waf1} induction) in a normal human fibroblast line (15). Similarly, Mothersill and Seymour reported that complete medium irradiated in the absence of cells with 5.0 Gy of ^{60}Co gamma rays had no effect on survival when transferred to unirradiated cultures (12).

The observation that DMSO could completely prevent the bystander effect in co-cultured DU-145 prostate carcinoma cells can be explained by two possible mechanisms:

1, since the DMSO was present at the time of irradiation, it might enter the targeted cells to protect them from producing the bystander signal(s) or it might enter the co-cultured cells to protect them from responding to the bystander signal(s); 2, since the DMSO is a known hydroxyl radical scavenger and it can react with other ROS like H_2O_2, it might react with the medium-soluble factor that elicits, or at least initiates, this bystander response. There is considerable experimental support in the literature for the involvement of reactive oxygen species (ROS) as the signaling agent in medium-transfer bystander effects. Lehnert *et al.* showed that addition of the enzyme superoxide dismutase (SOD) to alpha-particle-irradiated medium, or to conditioned medium harvested from above irradiated cells, blocked the ability of the medium to cause bystander effects in unirradiated cells. These authors suggested that superoxide played a central role in mediation of the bystander effect (11). Yang *et al.*, have provided evidence for the role of ROS in medium mediated bystander damage after low-LET irradiation (15). These authors showed that addition of SOD or catalase reduced the incidence of micronucleus formation, reduced the induction of $p21^{Waf1}$, and reduced the number of γ-H_2AX foci in co-cultured bystander cells. Interestingly, SOD or catalase did not have any effect on the decrease in clonogenic survival of the co-cultured cells, suggesting that an additional factor may be involved (15). The presence of ROS in irradiated cells and in bystander cells in medium-transfer experiments has been detected by prelabeling the cells with fluorescent dyes (15, 50) . The antioxidant, N-acetylcysteine was shown to suppress bystander effects (decreased survival, an increase in mitochondrial mass, and increased Bcl-2 expression) caused by medium from gamma-irradiated human keratinocytes (51) and provides additional evidence that directly-irradiated cells undergo oxidative stress and release a signal into the medium that

is capable of causing oxidative stress in bystander cells. The nature of the signal remains unclear.

One interesting and unique aspect of the data presented here is the very short effective lifetime of the medium-borne bystander signal. The co-cultured DU-145 cells had to be present in the medium above the targeted cells *during the irradiation* in order to sustain the damage leading to increased MN formation. When the co-cultured cells were placed into the medium above the targeted cells *immediately (< 1 minute) after the irradiation*, there was no bystander effect. The only difference between full expression of the bystander effect (~ 50% increase in MN) and no bystander effect was the ~1-minute delay between irradiation of the targeted cells and placing the insert containing the co-cultured cells into the medium. Otherwise, the dose to the targeted cells was the same and the 2-hr post-irradiation co-incubation was the same. It is the use of a co-culture experimental approach that has allowed us to make this observation. The presence of the co-cultured cells during the irradiation enables the detection of the effects of very short-lived factors.

This issue of the stability of the bystander signal has been addressed by others but if directly-irradiated cells are still present in the medium during the incubation period that produces the conditioned medium, which is then transferred to unirradiated cells, it is difficult to distinguish between the lifetime of the signal and continuous production of a short-lived signal by the irradiated cells. For example, Suzuki *et al.*, irradiated AL cells with broad-beam alpha particles, incubated these irradiated cells for 24 hours, and then transferred the medium to unirradiated cells (14). The unirradiated cells that received the conditioned medium were incubated for an additional 24 hrs and showed an increased

incidence of chromosome damage. These authors stated that the unknown soluble factor responsible for this medium-transfer bystander effect must have a lifespan of at least 24 hrs (14). It is possible, however, that the lifespan of the signal is short, but that it is produced continuously by the irradiated cells during the 24-hr incubation period. Lehnert *et al.* addressed the issue of the lifetime of the medium soluble agent directly by removing the medium from above the directly-irradiated cells and storing it for periods up to 24 hours in an incubator at 37 °C (11). A parallel study was included for medium that had been irradiated in the absence of cells. The conditioned medium harvested from above irradiated cells retained the ability to induce SCE in recipient cells for up to 24 hrs. Interestingly, when irradiated medium-alone (no cells were irradiated to condition the medium) was immediately transferred to non-irradiated cells, there was an increase in SCE in the recipient cells, but at the next time point, 30 minutes, the medium had no effect; i.e., the lifetime of the signal was < 30 min. Thus, these authors have reported the presence of soluble factors with different apparent lifetimes when stored at 37 °C. SOD was shown to inactivate both the short-lived factor from irradiated medium and the long-lived factor from irradiated cells (11). The short lifetime of the factor produced by irradiation of serum-containing medium is reminiscent of the short-lifetime factor reported here. But, in the case of the Lehnert study, the factor was produced by alpha-particle irradiation of serum-containing medium alone and in this study the factor was produced by irradiation of the DU-145 cells. These are the only two reports of very short-lived soluble clastogenic factors involved in medium-transfer bystander effect studies. Thus, we propose that some of the variation in the bystander effect literature could be the result of short-lived signaling factors that are not detected by some medium-transfer experimental protocols.

There are only a few literature reports of bystander effects in tumor cells. The role of nitric oxide (NO) as a mediator of the bystander effect has been clearly established in two human tumor cell lines (16, 17). Irradiation of human salivary gland tumor cells with 100 keV/μm carbon ions, followed by co-incubation for 24 hrs with unirradiated cells on an insert resulted in an increased incidence of MN in the unirradiated, co-cultured tumor cells (16). The bystander effect was blocked by the NO scavenger PTIO. Microbeam irradiations of T98G human glioblastoma cells with helium-3 ions ($^{3}He^{2+}$) have shown that irradiating only one cell in a population of ~1200 increased the MN yield in the entire population (17). Conditioned medium, produced by $^{3}He^{2+}$- irradiation of T98G glioma cells and incubation for 1 hr, induced an increase in MN formation when transferred to unirradiated T98G cells, and the NO inhibitor c-PTIO eliminated this medium-transfer bystander effect (17). NO serves as a signaling agent in a wide variety of pathways, and the induction of inducible nitric oxide synthase has been shown to be an early signaling event in response to ionizing radiation (52). The results in the DU-145 human prostate carcinoma cells differ in that the NO scavenger PTIO had no effect on the observed increase in MN formation in the co-cultured DU-145 cells. The difference between these reports could be the result of the different cell lines used, which could respond differently to irradiation and bystander signals. A medium-mediated bystander effect has also been reported in human malignant melanoma cells (53). These authors used a co-culture technique that involved plating cells such that individual large "megacolonies" of ~ 1 cm diameter were present in the same flask. Selective irradiation of the flask with 5 Gy ^{60}Co gamma rays allowed some colonies to serve as the irradiated population and the others as the non-irradiated

bystanders. These authors observed an increased incidence of micronuclei in cells from the shielded colonies at 24, 48 and 72 hours after irradiation (53).

The *in vitro* bystander effects in tumor cells reported here and in the literature have demonstrated that there is an effect, mediated by a soluble factor transferred through the medium, that can lead to increased MN formation. These lesions are believed to be the result of non-rejoined double strand breaks, providing support for the proposition that a bystander effect can be of benefit in a clinical situation. There have been very few studies of the radiation induced bystander effect in three dimensional cell systems. Irradiations of human or porcine ureter explants have shown that irradiation of individual cells in the explant can cause damage (apoptosis or micronuclei) in non-irradiated areas of the explant (54). The overlying medium from irradiated human urothelium explants was shown to cause effects in unirradiated urothelium explants or cells in culture (55). Pelleted mixtures of V79 hamster fibroblasts, some with ^{125}I incorporated into the DNA, have been used to show cell killing in a greater fraction of cells than was labeled; interpreted as evidence of a bystander effect in the cell pellet (10, 56).

Will this effect hold *in vivo*? There is a recent report of a bystander effect in tumors, i*n vivo*, which suggests that it may. Kassis *et al.*, incorporated 5-[^{125}I]iodo-2'-deoxyuridine into tumor cell DNA, mixed the labeled tumor cells with unlabeled tumor cells in various proportions, and used these mixtures to inoculate subcutaneous tumors in mice (19). The Auger electrons released from ^{125}I decay have subcellular ranges (<5 μm). The suppression of tumor growth was much greater than could be attributed to the radiation dose coming from ^{125}I decay in the labeled tumor cells and was attributed to a

bystander effect produced by the irradiated cells within the growing tumor nodule. The mode of signaling is unknown.

In summary, both *in vitro* and *in vivo* reports have demonstrated that the biologic effects of irradiation in tumor cells are not limited to directly-irradiated cells. Bystander effects in tumors remain an area with a largely unexplored potential for contributing to the overall therapeutic goal of elimination of all clonogenic tumor cells (57). The nature of the signal released by tumor cells needs further study. Nitric oxide is involved in some tumor cell lines, as well as the short-lived factor described in this report. As with the numerous bystander effect studies in normal cells, the bystander effect in tumors will most likely be a class of effects that differs in extent and mechanism depending on the type and dose of radiation used, the cell type involved and the particular endpoint studied. If the radiation-induced signaling factors involved in these tumor bystander effects can be identified and mechanisms of action elucidated, there may be an opportunity to manipulate these effects to improve the effectiveness of radiation therapy. The model system described here is well suited for further studies of whether the bystander effect in tumor cells can be exploited to increase tumor cell kill during alpha-particle based therapies.

References:

1. Nagasawa, H. and Little, J. B. Induction of sister chromatid exchanges by extremely low doses of alpha-particles. Cancer Res, *52:* 6394-6396., 1992.
2. Deshpande, A., Goodwin, E. H., Bailey, S. M., Marrone, B. L., and Lehnert, B. E. Alphaparticle-induced sister chromatid exchange in normal human lung fibroblasts: evidence for an extranuclear target. Radiat Res, *145:* 260-267, 1996.
3. Nagasawa, H. and Little, J. B. Unexpected sensitivity to the induction of mutations by very low doses of alpha-particle radiation: evidence for a bystander effect. Radiat Res, *152:* 552-557., 1999.
4. Prise, K. M., Belyakov, O. V., Folkard, M., and Michael, B. D. Studies of bystander effects in human fibroblasts using a charged particle microbeam. Int J Radiat Biol, *74:* 793-798., 1998.
5. Zhou, H., Randers-Pehrson, G., Waldren, C. A., Vannais, D., Hall, E. J., and Hei, T. K. Induction of a bystander mutagenic effect of alpha particles in mammalian cells. Proc Natl Acad Sci U S A, *97:* 2099-2104., 2000.
6. Azzam, E. I., de Toledo, S. M., and Little, J. B. Oxidative metabolism, gap junctions and the ionizing radiation-induced bystander effect. Oncogene, *22:* 7050-7057., 2003.
7. Mothersill, C. and Seymour, C. Radiation-induced bystander effects: past history and future directions. Radiat Res, *155:* 759-767., 2001.
8. Prise, K. M., Folkard, M., and Michael, B. D. A review of the bystander effect and its implications for low-dose exposure. Radiat Prot Dosimetry, *104:* 347-355, 2003.
9. McBride, W. H., Chiang, C. S., Olson, J. L., Wang, C. C., Hong, J. H., Pajonk, F., Dougherty, G. J., Iwamoto, K. S., Pervan, M., and Liao, Y. P. A sense of danger from radiation. Radiat Res, *162:* 1-19., 2004.
10. Bishayee, A., Hill, H. Z., Stein, D., Rao, D. V., and Howell, R. W. Free radical-initiated and gap junction-mediated bystander effect due to nonuniform distribution of incorporated radioactivity in a three-dimensional tissue culture model. Radiat Res, *155:* 335-344., 2001.
11. Lehnert, B. E., Goodwin, E. H., and Deshpande, A. Extracellular factor(s) following exposure to alpha particles can cause sister chromatid exchanges in normal human cells. Cancer Res, *57:* 2164-2171., 1997.
12. Mothersill, C. and Seymour, C. Medium from irradiated human epithelial cells but not human fibroblasts reduces the clonogenic survival of unirradiated cells. Int J Radiat Biol, *71:* 421-427., 1997.
13. Mothersill, C. and Seymour, C. B. Cell-cell contact during gamma irradiation is not required to induce a bystander effect in normal human keratinocytes: evidence for release during irradiation of a signal controlling survival into the medium. Radiat Res, *149:* 256-262., 1998.
14. Suzuki, M., Zhou, H., Geard, C. R., and Hei, T. K. Effect of medium on chromatin damage in bystander mammalian cells. Radiat Res, *162:* 264-269., 2004.
15. H. Yang, N. A. a. K. D. H. Medium-mediated intercellular communication is involved in bystander responses of X-ray-irradiated normal human fibroblasts. Oncogene, *24:* 2096-2103, 2005.

16. Shao, C., Furusawa, Y., Aoki, M., Matsumoto, H., and Ando, K. Nitric oxide-mediated bystander effect induced by heavy-ions in human salivary gland tumour cells. Int J Radiat Biol, *78:* 837-844., 2002.
17. Shao, C., Stewart, V., Folkard, M., Michael, B. D., and Prise, K. M. Nitric oxide-mediated signaling in the bystander response of individually targeted glioma cells. Cancer Res, *63:* 8437-8442., 2003.
18. Shao, C., Folkard, M., Michael, B. D., and Prise, K. M. Targeted cytoplasmic irradiation induces bystander responses. Proc Natl Acad Sci U S A, *101:* 13495-13500. Epub 12004 Sep 13402., 2004.
19. Xue, L. Y., Butler, N. J., Makrigiorgos, G. M., Adelstein, S. J., and Kassis, A. I. Bystander effect produced by radiolabeled tumor cells in vivo. Proc Natl Acad Sci U S A, *99:* 13765-13770. Epub 12002 Oct 13704., 2002.
20. Coderre, J. and Morris, G. The radiation biology of boron neutron capture therapy. Radiat Res, *151:* 1-18, 1999.
21. Harris, M. Monoclonal antibodies as therapeutic agents for cancer. Lancet Oncol, *5:* 292-302., 2004.
22. Knox, S. J. and Meredith, R. F. Clinical radioimmunotherapy. Semin Radiat Oncol, *10:* 73-93., 2000.
23. Goldenberg, D. M. Targeted therapy of cancer with radiolabeled antibodies. J Nucl Med, *43:* 693-713., 2002.
24. Murray, J. L. Monoclonal antibody treatment of solid tumors: a coming of age. Semin Oncol, *27:* 64-70; discussion 92-100., 2000.
25. Smith, D. C. Chemotherapy for hormone refractory prostate cancer. Urol Clin North Am, *26:* 323-331., 1999.
26. Meredith, R. F., Khazaeli, M. B., Macey, D. J., Grizzle, W. E., Mayo, M., Schlom, J., Russell, C. D., and LoBuglio, A. F. Phase II study of interferon-enhanced 131I-labeled high affinity CC49 monoclonal antibody therapy in patients with metastatic prostate cancer. Clin Cancer Res, *5:* 3254s-3258s., 1999.
27. McDevitt, M. R., Barendswaard, E., Ma, D., Lai, L., Curcio, M. J., Sgouros, G., Ballangrud, A. M., Yang, W. H., Finn, R. D., Pellegrini, V., Geerlings, M. W., Jr., Lee, M., Brechbiel, M. W., Bander, N. H., Cordon-Cardo, C., and Scheinberg, D. A. An alpha-particle emitting antibody ([213Bi]J591) for radioimmunotherapy of prostate cancer. Cancer Res, *60:* 6095-6100., 2000.
28. Li, Y., Russell, P. J., and Allen, B. J. Targeted alpha-therapy for control of micrometastatic prostate cancer. Expert Rev Anticancer Ther, *4:* 459-468., 2004.
29. Vallabhajosula, S., Smith-Jones, P. M., Navarro, V., Goldsmith, S. J., and Bander, N. H. Radioimmunotherapy of prostate cancer in human xenografts using monoclonal antibodies specific to prostate specific membrane antigen (PSMA): studies in nude mice. Prostate, *58:* 145-155., 2004.
30. DeNardo, S. J., DeNardo, G. L., Yuan, A., Richman, C. M., O'Donnell, R. T., Lara, P. N., Kukis, D. L., Natarajan, A., Lamborn, K. R., Jacobs, F., and Siantar, C. L. Enhanced therapeutic index of radioimmunotherapy (RIT) in prostate cancer patients: comparison of radiation dosimetry for 1,4,7,10-tetraazacyclododecane-N,N',N",N"'-tetraacetic acid (DOTA)-peptide versus 2IT-DOTA monoclonal antibody linkage for RIT. Clin Cancer Res, *9:* 3938S-3944S., 2003.

31. McDevitt, M. R., Ma, D., Lai, L. T., Simon, J., Borchardt, P., Frank, R. K., Wu, K., Pellegrini, V., Curcio, M. J., Miederer, M., Bander, N. H., and Scheinberg, D. A. Tumor therapy with targeted atomic nanogenerators. Science, *294:* 1537-1540., 2001.
32. Lorimore, S. A., Kadhim, M. A., Pocock, D. A., Papworth, D., Stevens, D. L., Goodhead, D. T., and Wright, E. G. Chromosomal instability in the descendants of unirradiated surviving cells after a-particle irradiation. Proc. Natl. Acad. Sci. USA, *95:* 5730-5733, 1998.
33. Jostes RF, H. T., James AC, Cross FT, Schwartz JL, Rotmensch J, Atcher RW, Evans HH, Mencl J, Bakale G, et al. In vitro exposure of mammalian cells to radon: dosimetric considerations. Radiat Res., *127:* 211-219, 1991.
34. Geard, C. R., Jenkins-Baker, G., Marino, S. A., and Ponnaiya, B. Novel approaches with track segment alpha particles and cell co-cultures in studies of bystander effects. Radiat Prot Dosimetry, *99:* 233-236, 2002.
35. Ponnaiya, B., Jenkins-Baker, G., Brenner, D. J., Hall, E. J., Randers-Pehrson, G., and Geard, C. R. Biological responses in known bystander cells relative to known microbeam-irradiated cells. Radiat Res, *162:* 426-432., 2004.
36. Shao, C., Aoki, M., and Furusawa, Y. Bystander effect in lymphoma cells vicinal to irradiated neoplastic epithelial cells: nitric oxide is involved. J Radiat Res (Tokyo), *45:* 97-103., 2004.
37. Sachs, D. J. B. a. R. K. Do low dose-rate bystander effects influence domestic radon risks? Int J Radiat Biol, *78:* 593-604, 2002.
38. Sachs, D. J. B. a. R. K. Domestic radon risks may be dominated by bystander effects--but the risks are unlikely to be greater than we thought. Health Physics, *85:* 103-108, 2003.
39. Little, M. P. and Wakeford, R. The bystander effect in C3H 10T cells and radon-induced lung cancer. Radiat Res, *156:* 695-699., 2001.
40. Coderre, J. A. and Morris, G. M. The radiation biology of boron neutron capture therapy. Radiat. Res., *151:* 1-18, 1999.
41. Metting, N. F., Koehler, A. M., Nagasawa, H., Nelson, J. M., and Little, J. B. Design of a benchtop alpha particle irradiator. Health Phys, *68:* 710-715., 1995.
42. Neti, P. V., de Toledo, S. M., Perumal, V., Azzam, E. I., and Howell, R. W. A multi-port low-fluence alpha-particle irradiator: fabrication, testing and benchmark radiobiological studies. Radiat Res, *161:* 732-738., 2004.
43. Raju, M. R., Eisen, Y., Carpenter, S., and Inkret, W. C. Radiobiology of alpha particles. III. Cell inactivation by alpha-particle traversals of the cell nucleus. Radiat Res, *128:* 204-209., 1991.
44. Zhou, H., Suzuki, M., Geard, C. R., and Hei, T. K. Effects of irradiated medium with or without cells on bystander cell responses. Mutat Res, *499:* 135-141., 2002.
45. E. I. Azzam, S. M. d. T. a. J. B. L. Direct evidence for the participation of gap junction-mediated intercellular communication in the transmission of damage signals from alpha -particle irradiated to nonirradiated cells. Proc Natl Acad Sci U S A, *98:* 473-478, 2001.
46. Ruch, J. E. T. a. R. J. Gap junctions as targets for cancer chemoprevention and chemotherapy. Curr Drug Targets, *3:* 465-482, 2002.

47. Seymour, C. B. and Mothersill, C. Relative contribution of bystander and targeted cell killing to the low-dose region of the radiation dose-response curve. Radiat Res, *153:* 508-511., 2000.
48. Huo, L., Nagasawa, H., and Little, J. B. HPRT mutants induced in bystander cells by very low fluences of alpha particles result primarily from point mutations. Radiat Res, *156:* 521-525., 2001.
49. Narayanan, P. K., Goodwin, E. H., and B. E. Lehnert Alpha particles initiate biological
production of superoxide anions and hydrogen peroxide in human cells. Cancer Res, *57:* 3963-3971, 1997.
50. Narayanan, P. K., Goodwin, E. H., and Lehnert, B. E. Alpha particles initiate biological production of superoxide anions and hydrogen peroxide in human cells. Cancer Res, *57:* 3963-3971., 1997.
51. Maguire, P., Mothersill, C., Seymour, C., and Lyng, F. M. Medium from irradiated cells induces dose-dependent mitochondrial changes and BCL2 responses in unirradiated human keratinocytes. Radiat Res, *163:* 384-390, 2005.
52. Leach, J. K., Black, S. M., Schmidt-Ullrich, R. K., and Mikkelsen, R. B. Activation of constitutive nitric-oxide synthase activity is an early signaling event induced by ionizing radiation. J Biol Chem, *277:* 15400-15406. Epub 12002 Feb 15420., 2002.
53. Przybyszewski, W. M., Widel, M., Szurko, A., Lubecka, B., Matulewicz, L., Maniakowski, Z., Polaniak, R., Birkner, E., and Rzeszowska-Wolny, J. Multiple bystander effect of irradiated megacolonies of melanoma cells on non-irradiated neighbours. Cancer Lett, *214:* 91-102., 2004.
54. Belyakov, O. V., Folkard, M., Mothersill, C., Prise, K. M., and Michael, B. D. A proliferation-dependent bystander effect in primary porcine and human urothelial explants in response to targeted irradiation. Br J Cancer, *88:* 767-774., 2003.
55. Mothersill, C., Rea, D., Wright, E. G., Lorimore, S. A., Murphy, D., Seymour, C. B., and O'Malley, K. Individual variation in the production of a 'bystander signal' following irradiation of primary cultures of normal human urothelium. Carcinogenesis, *22:* 1465-1471., 2001.
56. Howell, R. W. and Bishayee, A. Bystander effects caused by nonuniform distributions of DNA-incorporated (125)I. Micron, *33:* 127-132, 2002.
57. Mothersill, C. E., Moriarty, M. J., and Seymour, C. B. Radiotherapy and the potential exploitation of bystander effects. Int J Radiat Oncol Biol Phys, *58:* 575-579., 2004.

Chapter 5 Anti-Cancer Drug Studies

5.1 Introduction

5.1.1 Paclitaxel

Paclitaxel (trade name Taxol) (figure 5-1) belongs to a group of anti-cancer drugs called taxanes. Taxanes have a unique way of preventing the growth of cancer cells: they affect cell structures called microtubules, which play an important role in cell functions. In normal cell growth, microtubules are formed when a cell starts dividing. Microtubules are conveyer belts inside the cells. They move vesicles, granules, organelles like mitochondria, and chromosomes via special attachment proteins. They also serve a cytoskeletal role. Structurally, they are linear polymers of a globular protein called tubulin. Once the cell stops dividing, the microtubules are broken down or destroyed. Paclitaxel was found to stabilize microtubules and arrest the cells in the G_2 and M phases of the cell cycle (1).

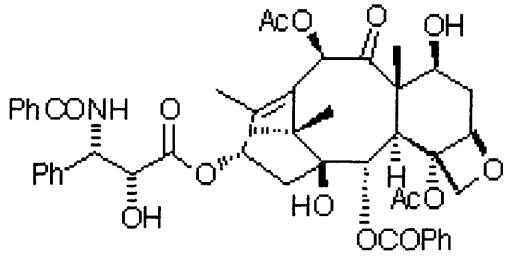

Figure 5-1. The molecular structure of paclitaxel

In 1984, National Cancer Institute (NCI) began clinical trials that looked at paclitaxel's safety and how well it worked to treat certain cancers. In 1989, researchers at The Johns Hopkins Oncology Center reported that tumors shrank or disappeared in 30 percent of patients who received paclitaxel for the treatment of advanced ovarian cancer. Although the responses to paclitaxel were not permanent (they lasted an average of 5

months, some up to 9 months), it was clear that advanced ovarian cancer patients could benefit from this treatment. In December 1992, the U.S. Food and Drug Administration (FDA) approved the use of paclitaxel for ovarian cancer that was resistant to treatment. Paclitaxel was later approved as an initial treatment for ovarian cancer in combination with a platinum-based anticancer drug like cisplatin. In 1994, the FDA also approved paclitaxel for the treatment of breast cancer that recurred within 6 months after adjuvant chemotherapy (chemotherapy that is given after the primary treatment to enhance the effectiveness of the primary treatment), or that spread (metastasized) to nearby lymph nodes or other parts of the body. Paclitaxel is also used for other cancers, including AIDS-related Kaposi's sarcoma and lung cancer. One study showed that paclitaxel can significantly suppress both primary orthotopic murine prostate tumor (RM-1) growth (up to 60%) and the formation of pseudometastatic tumor colony formation in the lungs (by up to 46%) in C57BL/6 mice *in vivo* (2).

Paclitaxel is a compound that was originally isolated from the bark of the Pacific yew tree (Taxus brevifolia). The natural source, the Pacific yew tree, is an environmentally protected species, which is also one of the slowest growing trees in the world. Isolation of the compound, which is contained in the bark, is a complicated and expensive process and involves killing the tree. The quantities available by this method are pitifully small. It would take six 100-year old trees to provide enough paclitaxel to treat just one patient.

As demand for paclitaxel grew, NCI, in collaboration with other Government agencies and the pharmaceutical company Bristol-Myers Squibb, worked to increase the availability and find other sources of paclitaxel besides the bark of the Pacific yew tree. This work led to the production of a semi-synthetic form of paclitaxel derived from the

needles and twigs of the Himalayan yew tree (Taxus bacatta), which is a renewable resource. The FDA approved the semi-synthetic form of paclitaxel in the spring of 1995. This form of paclitaxel has now replaced the drug derived from the bark of the Pacific yew tree.

The radiosensitizing properties of paclitaxel were discovered more than 10 years ago; it synchronized tumor cells in G2/M phase, the most radiosensitive portion of the cell cycle. Other radiosensitizing mechanisms of paclitaxel have been also discussed, such as reoxygenation, promotion of radio-apoptosis and antiangiogenic cooperation. Many phase I and II studies have been performed, essentially in bronchus and head and neck carcinomas. Many studies combined cisplatin or carboplatin with paclitaxel, demonstrating that this combination is feasible and efficient (3). *In vitro*, paclitaxel was reported to be a potent radiosensitizer in several ovarian cancer cell lines (BG-1, SKOV-3, and OVCAR-3) (4, 5), a human grade 3 astrocytoma cell line, G18 (6), and a human laryngeal squamous carcinoma cell line Hep-2 (7).

Paclitaxel is a radiosensitizer for some but not all human tumor cell lines. The effect of paclitaxel at concentrations ranging from 0 to 10000 nM on the radiation sensitivity of human breast (MCF-7), lung (A549), ovary (OVG-1), and pancreas (PC-Sh) adenocarcinoma cells was determined using clonogenic assays. The radiosensitizing effect was observed in MCF-7 and OVG-1 cells but not in A549 cells. PC-Sh cells demonstrated a complex and inconsistent radiosensitization response to paclitaxel: radiosensitization was observed at 10% survival and no radiosensitization at 1% survival (8). Using micronucleus formation as the endpoint, L5178Y, V79 and HeLa showed an additive effect of the single

treatments (paclitaxel or radiation only). And the human breast cancer cell line MCF-7 showed lower than additive micronucleus frequencies (9).

The radiosensitizing effect of paclitaxel is both drug-dose and radiation-dose dependent. Paclitaxel was reported to be able to reduce or enhance radiation cell killing, in HeLa and SQ20B human tumor cells *in vitro*, depending on the drug concentration. Reductions of radiosensitivity or antagonistic effects were observed at low drug concentrations (0.9 nM for SQ20B and 1.6 nM for HeLa). At higher drug concentrations, a drug dose-dependent, supra-additive radiation-drug interaction was observed (10). Similar results were observed in two squamous cell carcinomas of the head and neck, SCC-9 and HEP-2. In general there was slight synergism at low dose-low effect levels (e.g., at a paclitaxel concentration of 0.002 μg/ml or lower combined with radiation doses of 0.1-0.3 Gy), moderate antagonism at intermediate dose ranges and strong synergism at high dose ranges (e.g., at a paclitaxel concentration of 0.012-0.06 μg/ml and radiation doses of 3-10 Gy) (11).

The combination of taxoid derivatives (paclitaxel and docetaxel) with irradiation was evaluated in ovarian carcinoma cell lines (A2780 and CAVEOC-2) using a multicellular tumor spheroid (MTS) three-dimensional model and compared to the conventional monolayer model. In A2780 monolayer culture, the combination was synergistic for paclitaxel and additive for docetaxel. In spheroids, both compounds induced a decrease in RSV2 (the residual/control volume ratios at 2 Gy) and SCD50 (the dose inducing 50% decrease in MTS number) in the two cell lines, and their combination with radiation was additive (12).

The combination of radiation and paclitaxel was investigated in human prostate carcinoma lines *in vitro*, and in a Dunning rat prostate adenocarcinoma *in vivo*. Flow cytometry showed an enhancement of radiation toxicity associated with paclitaxel-induced cell cycle phase arrest at G2/M. Adverse side effects were minimal. The results implied that combination of these agents may have clinical potential in prostate cancer treatment (13).

5.1.2 Oxaliplatin

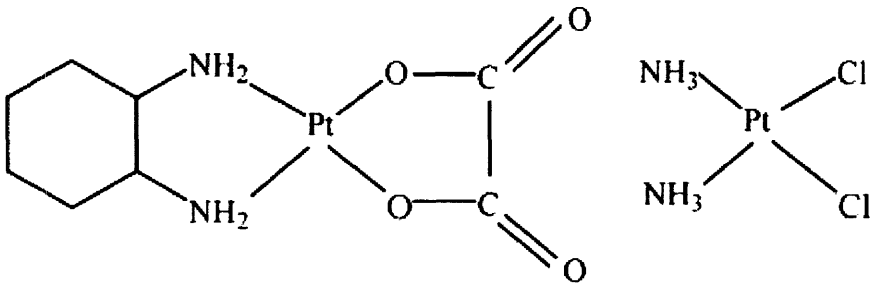

Oxaliplatin **Cisplatin**

Figure 5-2. Chemical structures of oxaliplatin and cisplatin.

Oxaliplatin (common trade name: Eloxatin) is a third-generation platinum compound containing a 1,2-diaminocyclohexane (DACH) moiety, which has a wide spectrum of anticancer activity in *in vitro* systems and has displayed preclinical and clinical activity in a wide variety of tumors (14, 15). Over the last 30 years, a large number of platinum analogues have been synthesized to enlarge the spectrum of activity, overcome cellular resistance, and/or reduce the toxicity of both first (*e.g.*, cisplatin) and second generation (*e.g.*, carboplatin) platinum drugs (16). Of these platinum analogues, compounds containing a DACH carrier ligand, such as oxaliplatin (figure 5-2), have consistently demonstrated anti-tumor activity in cell lines with acquired cisplatin resistance

and appear to be active in tumor types that are intrinsically resistant to cisplatin and carboplatin (17-19).

Like cisplatin, oxaliplatin reacts with DNA, forming primary lesions that block DNA replication and transcription. Cisplatin and oxaliplatin induce a cell cycle block in the G_2/M phase (20) and generate DNA lesions such as interstrand DNA crosslinks (ISC) and DNA-protein crosslinks (DPC) (21). Although the molecular mechanism(s) providing the difference in resistance remain largely unknown, some *in vitro* studies underline the importance of DNA repair. Oxaliplatin forms DACH-Pt DNA adducts with the same sites at the nucleotide level and with the same regional interactions as cisplatin, and both drugs show a preference for nuclear DNA over mitochondrial DNA. Compared with cisplatin, oxaliplatin formed significantly fewer Pt-DNA adducts. The adducts formed by both drugs are repaired with similar kinetics, but oxaliplatin is more efficient than cisplatin per equal number of DNA adducts in inhibiting DNA chain elongation (22). The differences in the structure of the adduct produced by cisplatin and oxaliplatin are consistent with the observation that they are differentially recognized by the DNA mismatch repair system. Studies have shown that the loss of DNA mismatch repair results in resistance to cisplatin but not to oxaliplatin (23).

Oxaliplatin was found to be a good radiosensitizer in two head and neck cancer cells lines, KB and Hep2, *in vitro* (24). Combined with low-LET radiation, oxaliplatin showed additive-antagonistic effects for the p53 mutated human colon cancer cell line (WiDr) but additive-synergistic effects for the p53 wild type human colon cancer cell line (SW403) (25). Oxaliplatin has been used as radiosensitizer for rectal cancer (26, 27) and esophageal cancer (28) in clinical trials.

The two drugs were chosen in our pilot synergy studies due to their reported radiosensitizing effects in human cancer cell lines.

5.2 Materials and Methods

5.2.1 Anti-cancer drugs on DU-145 cells

Taxol was obtained from Sigma (5 mg, product number: T-7191), freshly dissolved in 1 ml DMSO resulting in a stock concentration of 5 mg/ml. Oxaliplatin was obtained from Sigma (5 mg, product number: O-9512), freshly dissolved in 1 ml distilled water resulting in a stock concentration of 5 mg/ml. The stock solutions were stored at -20 °C and further diluted to required concentrations in the medium for the experiments.

In the drug only experiments, about 5 x 10^5 DU-145 cells were plated into the Mylar dishes and allowed to attach overnight. Medium containing various concentrations of Taxol or oxaliplatin was then used to replace the old medium in the Mylar dishes. The cells were incubated with drugs for 24 hr before they were trypsinized and processed for clonogenic assay, as described in the 3.2.3 section of Chapter 3. Data are shown as means ± SD from two independent experiments.

5.2.2 Anti-cancer drugs plus alpha-particle irradiation

Both Taxol and oxaliplatin have been reported to show synergistic effects with low LET radiation such as X-rays and gamma-rays (4-7, 13, 24-28). The study described here represents the first investigation of combined effects of these two drugs with high LET alpha-particle irradiation.

In the experiments, ~ 5 x 10^5 DU-145 cells were plated into the Mylar dishes and allowed to attach overnight. Medium containing various concentrations of Taxol (0.005,

0.01 or 0.05 μg/ml) or oxaliplatin (0.5 or 1 μg/ml) was then used to replace the old medium in the Mylar dishes. The cells were incubated with drugs for 24 hr or for 96 hr. The drug-containing medium was then replaced with fresh medium before the cells were irradiated with graded doses of alpha particles at room temperature. Finally, the cells were processed for clonogenic assay, as described in the 3.2.3 section of Chapter 3.

5.2.3 Anti-cancer drugs plus the bystander effect

A bystander effect was observed in the DU-145 cells in the co-culture system described in Chapter 4. The objective of the study described here was to study the combined effects of the two anti-cancer drugs with the bystander effect.

For the experiments, ~ 5×10^5 DU-145 cells were seeded in the Mylar dish and ~ 5×10^4 cells were seeded in the Snapwell insert (12 mm diameter; 1.13 cm^2 growth area). The cells were allowed to attach overnight. The cells in the insert were treated with Taxol or oxaliplatin for 24 hr. On the day of the irradiation experiment, 6 ml of fresh medium was added to each Mylar dish. The drug-containing medium in the insert was removed and fresh medium was used to wash the insert once. Then the insert was detached from the support rings with sterile tweezers and placed upside down in the medium above the cells in the Mylar dish. The Mylar dish was then placed on the alpha-particle irradiator and the bottom layer of cells was irradiated at room temperature for 1 min to deliver an alpha-particle dose of 1.2 Gy. After the irradiation, the Mylar dish, together with the insert, was put back into the incubator and co-incubated at 37 °C for 2 hrs (or for 24 hrs in some cases). After the co-incubation, the insert was taken out of the Mylar dishes and the cells in the insert were collected by trypsinization and processed for the micronucleus assay as described in Chapter 3.

5.2.4 Flow cytometry cell cycle study

Flow cytometry was used to study the effect of Taxol treatment on the cell cycle distribution of the DU-145 cells. The fluorescence activated cell sorter (FACS) available in the MIT Flow Cytometry Core Facility of the Center for Cancer Research was used for these studies. The following is the experimental procedure:

1. About 1×10^7 DU-145 cells were seeded in each T-75 flask for each treatment and control. The cells were allowed to attach overnight.
2. Fresh medium containing various concentrations of Taxol or oxaliplatin was used to replace the old medium, and the cells were incubated in the drug-containing medium for 24 hr.
3. Harvest the cells by trypsinization and transfer them to a 15 ml conical tube. Check for single-cell suspension. Centrifuge at 1000 rpm for five minutes and remove the supernatant.
4. Wash the cells twice in PBS without calcium or magnesium. At the last wash, count the total number of cells, and record the number on the tube.
5. Resuspend the pellet in approximately 500 μl of ice-cold PBS. Pipet up and down for about 20 times. It is important to make a good single-cell suspension at this point, or the cells will be fixed as clumps.
6. Add 5 ml of cold (-20° C) 75% ethanol, drop by drop, while vortexing at speed 7 to prevent clumping. Fix the cells at 4° C at least overnight.
7. Take 5×10^6 cells into a new 15 ml conical tube. Centrifuge at 1000 rpm and remove the ethanol.

8. Vortex pellet. Wash twice in 5 ml of PBS + 1% BSA (Albumin Bovine Serum) or calf serum. (Ethanol-fixed cells are difficult to pellet. Adding BSA or serum to the wash medium will overcome this.)
9. Resuspend the pelleted cells in 800 µl of PBS containing 1% BSA or 1% calf serum.
10. Add 100 µl of 10 × propidium iodide (PI) solution (500 µg/ml PI in 3.8×10^{-2} M sodium citrate, pH 7.0).
11. Add 100 µl of boiled RNase A (10 mg/ml prepared in 10 mM Tris-HCl, pH 7.5) and incubate at 37° C for 30 minutes. (If the samples will not be used immediately, they should be protected from light and stored at 4 °C.)
12. The cell samples wrapped in aluminum foil were carried in a foam box filled with ice to the MIT Flow Cytometry Core Facility to be analyzed on the flow cytometer.

5.3 Results

5.3.1 Anti-cancer drugs on DU-145 cells

Figure 5-3 shows the cell survival curve after the treatment with various concentrations of Taxol for 24 hr. Figure 5-4 shows the cell survival curve after the treatment with various concentrations of oxaliplation for 24 hr.

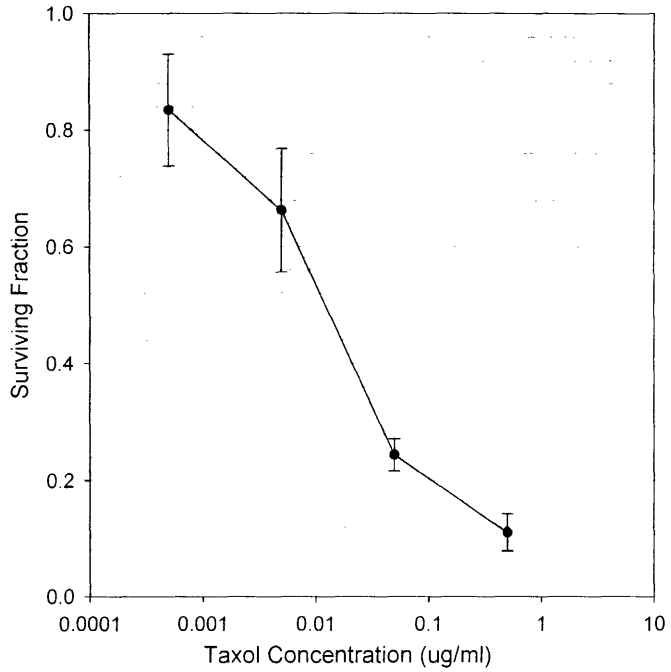

Figure 5-3. The survival curve of DU-145 cells after 24 hr treatment with various concentrations of Taxol. The data points represent the means ± standard deviation of five replicate dishes in each experiment from two independent experiments.

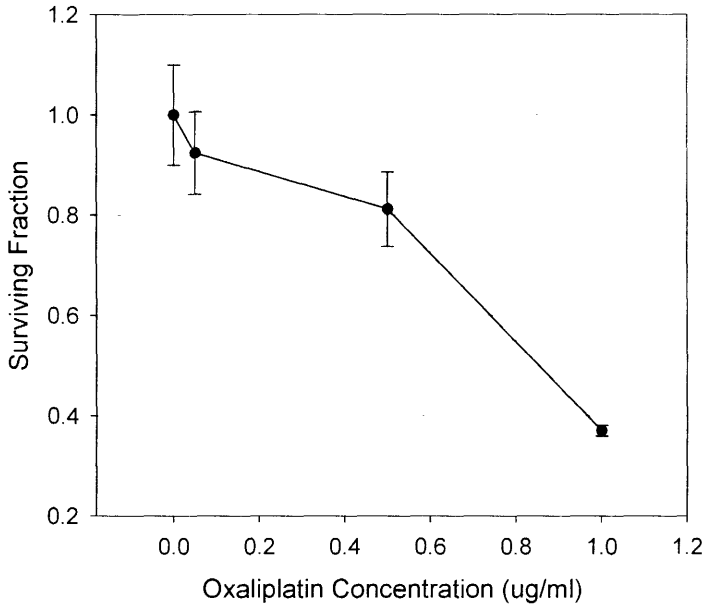

Figure 5-4. The survival curve of DU-145 cells after 24 hr treatment with various concentrations of oxaliplatin. The data points represent the means ± standard deviation of five replicate dishes in each experiment from two independent experiments.

5.3.2 Anti-cancer drugs plus alpha-particle irradiation

5.3.2.1 Cell survival results

Figure 5-5, Figure 5-6, Figure 5-7 show the DU-145 survival curves for alpha-particle irradiation combined with different concentration of Taxol or Oxaliplatin pre-treatment for 24 hr. The surviving fractions on the y-axis are on log-scale. All survival curves were normalized for plating efficiency (~46%) in absence of drug.

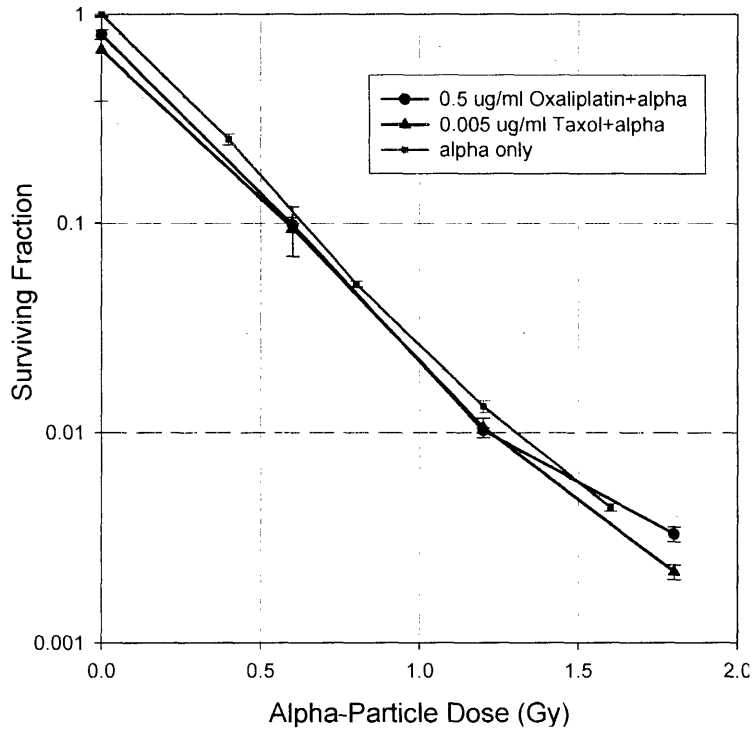

Figure 5-5. The DU-145 cell survival curves for alpha-particle irradiation only, alpha-particle irradiation following 0.005 μg/ml Taxol treatment for 24 hr and alpha-particle irradiation following 0.5 μg/ml oxaliplatin treatment for 24 hr. The data points represent the means ± standard deviation of five replicate dishes in each experiment from a total of five independent alpha-only experiments, two "0.005μg/ml Taxol plus alpha" experiments and two "0.5 μg/ml oxaliplatin plus alpha" experiments.

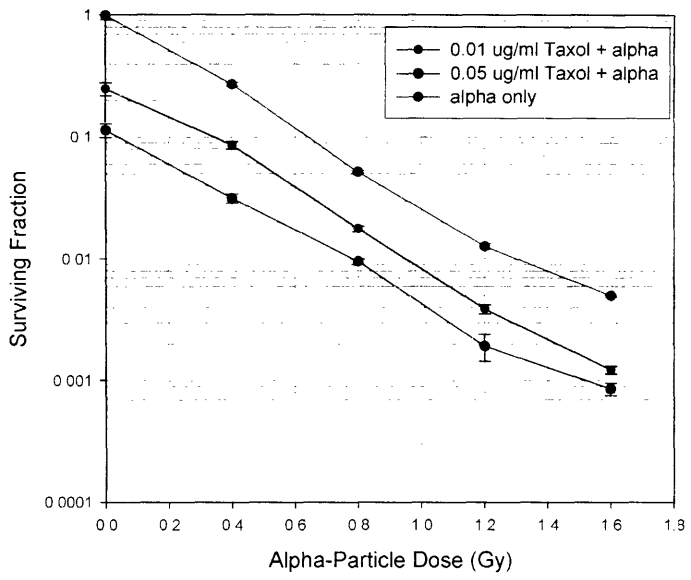

Figure 5-6. The DU-145 cell survival curves for alpha-particle irradiation only, alpha-particle irradiation following 0.01 μg/ml Taxol treatment for 24 hr and 0.05 μg/ml Taxol treatment for 24 hr. The data points for "Taxol plus alpha" represent the means ± standard deviation of five replicate dishes in one experiment.

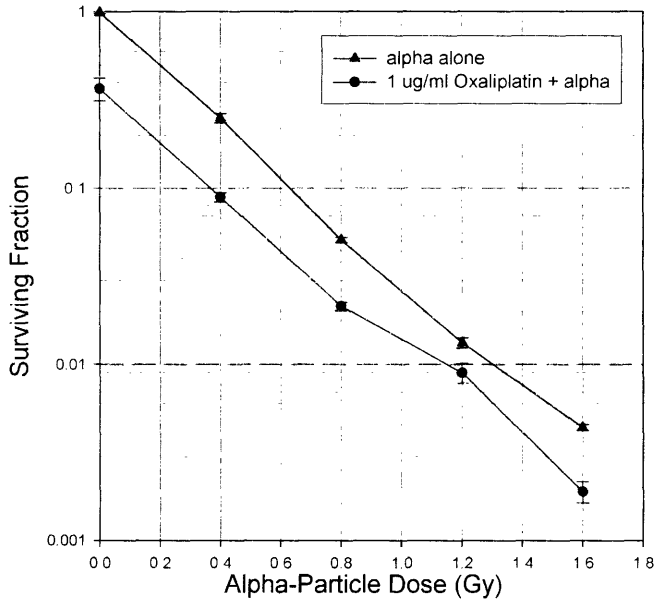

Figure 5-7. The DU-145 cell survival curves for alpha-particle irradiation only and alpha-particle irradiation following 1 μg/ml Oxaliplatin treatment for 24 hr. The data points represent the means ± standard deviation of five replicate dishes in one experiment.

5.3.2.2 Quantitative analysis

The combination index (CI) equation of Chou-Talalay (29) is used for the quantitative analysis of the combined effects.

Simply speaking, the combination index (CI) was calculated by the Chou-Talalay equation, which takes into account both the potency and the shape of the dose-effect curve. The general equation for the classic isobologram is given by:

$$CI = \frac{D_1}{(D_x)_1} + \frac{D_2}{(D_x)_2}$$

where $(D_x)_1$ is the concentration of the drug only that gives x% inhibition and $(D_x)_2$ is the alpha-particle irradiation dose only thats give x% inhibition, whereas D_1 and D_2 in the numerators are the concentration of drug and dose of radiation in combination that also inhibit x% (*i.e.* isoeffective). CI < 1, CI = 1 and CI > 1 indicate synergism, additive effect and antagonism, respectively (30).

A simple graphical method called isobologram can be used to tell whether a combination dose is additive, superadditive (synergistic) or subadditive (antagonistic). Specifically, a particular effect level is selected, such as 50% of the maximum, and doses of drug A and drug B (each alone) that give this effect are plotted as axial points in a Cartesian plot (figure 5-8) (the doses are denoted by italicized letters that correspond to the respective drugs). The straight line connecting *A* and *B* is the locus of points (dose pairs) that will produce this effect in a simply additive combination. This line of additivity allows a comparison with the actual dose pair that produces this effect level experimentally. An actual dose pair such as point Q attains this effect with lesser quantities and is superadditive (synergistic), while the dose pair denoted by point R means greater quantities

are required and is therefore subadditive. A point such as P that appears below the line would probably be simply additive (31).

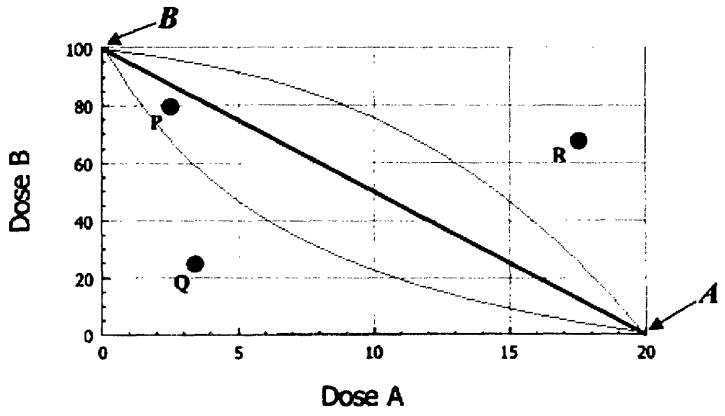

Figure 5-8. Illustrative isobologram for drug A and drug B. When the dose-response data for both drugs could be fitted by linear regressions, the diagonal line represents dose pairs producing additive effects; when non-linear curve fitting is desired or actually required for the dose-response data for one drug and both drugs, the area defined by the two fine curves near the diagonal represents additive effects. The shape of the additive area is decided by the dose response curves of the two drugs (31).

Choosing 50% survival as the particular effect level, table 5-1 gives all the single dose points and the paired dose points to achieve 50% SF.

50% surviving fraction							
alpha (Gy)	0.2	0	0.095	alpha (Gy)	0.2	0	0.135
Taxol (μg/ml)	0	0.01	0.005	Oxaliplatin (μg/ml)	0	0.86	0.5

Table 5-1. the dose information for 50% surviving fraction.

The isobologram at 50% SF for Taxol plus alpha-particle irradiation is shown in Figure 5-9 and the isobologram at 50% SF for oxaliplatin plus alpha-particle irradiation is shown in figure 5-10.

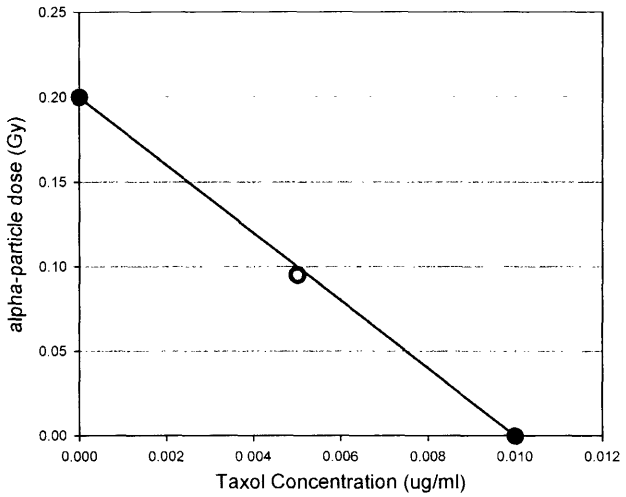

Figure 5-9. 50% SF isobologram for 24 hr Taxol treatment and alpha-particle irradiation. The 0.2 Gy alpha-particle dose on the y-axis and the 0.01 ug/ml Taxol concentration on the x-axis define the additivity line; the 0.005 ug/ml Taxol plus 0.095 Gy alpha-particle dose define the actual dose pair point (empty dot). The dose pair point falls right on the line, suggesting an additive effect.

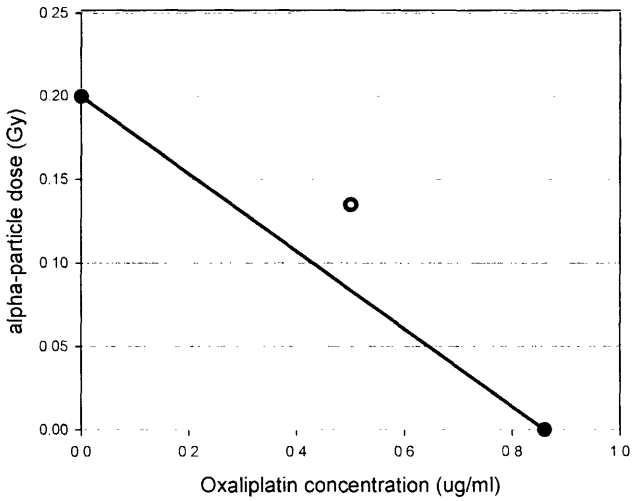

Figure 5-10. 50% SF isobologram for 24 hr Oxaliplatin treatment and alpha-particle irradiation. The 0.2 Gy alpha-particle dose on the y-axis and the 0.86 ug/ml Oxaliplatin concentration on the x-axis define the additivity line; the 0.5 ug/ml Oxaliplatin plus 0.135 Gy alpha-particle dose define the actual dose pair point (empty dot). The dose pair point falls above the line, suggesting a subadditive effect or probably just additive effect, as explained by Figure 5-8.

Using the classic isobologram equation described before, the CIs could be calculated as following:

For alpha + Taxol:

$$CI = \frac{(D)_1}{(D_x)_1} + \frac{(D)_2}{(D_x)_2} = \frac{0.095}{0.2} + \frac{0.005}{0.01} = 0.975$$

For alpha + oxaliplatin:

$$CI = \frac{(D)_1}{(D_x)_1} + \frac{(D)_2}{(D_x)_2} = \frac{0.135}{0.2} + \frac{0.5}{0.86} = 1.26$$

5.3.3 Anti-cancer drug plus the bystander effect

5.3.3.1 Micronucleus assay results

Treatment of DU-145 cells with 0.5 μg/ml oxaliplatin for 24 hr followed by the bystander treatment produced a very low number of bi-nucleated cells using the micronucleus assay. The reason for this is due to the interference between the drug oxaliplatin and cytochalasin-B. Treatment of DU-145 cells with 0.5 μg/ml oxaliplatin for 24 hr only produced a modest toxicity in clonogenic assay (see figure 5-4). This drug concentration was chosen for the combinational studies. But the mechanism of this interference needs further study. As a result, the following studies have focused on Taxol treatment plus the bystander effect.

Figure 5-11 shows the MN/BN results for Taxol plus the bystander effect. Two different concentrations of Taxol were used: 0.005 μg/ml and 0.01 μg/ml. Mathematical analysis of the results is presented below.

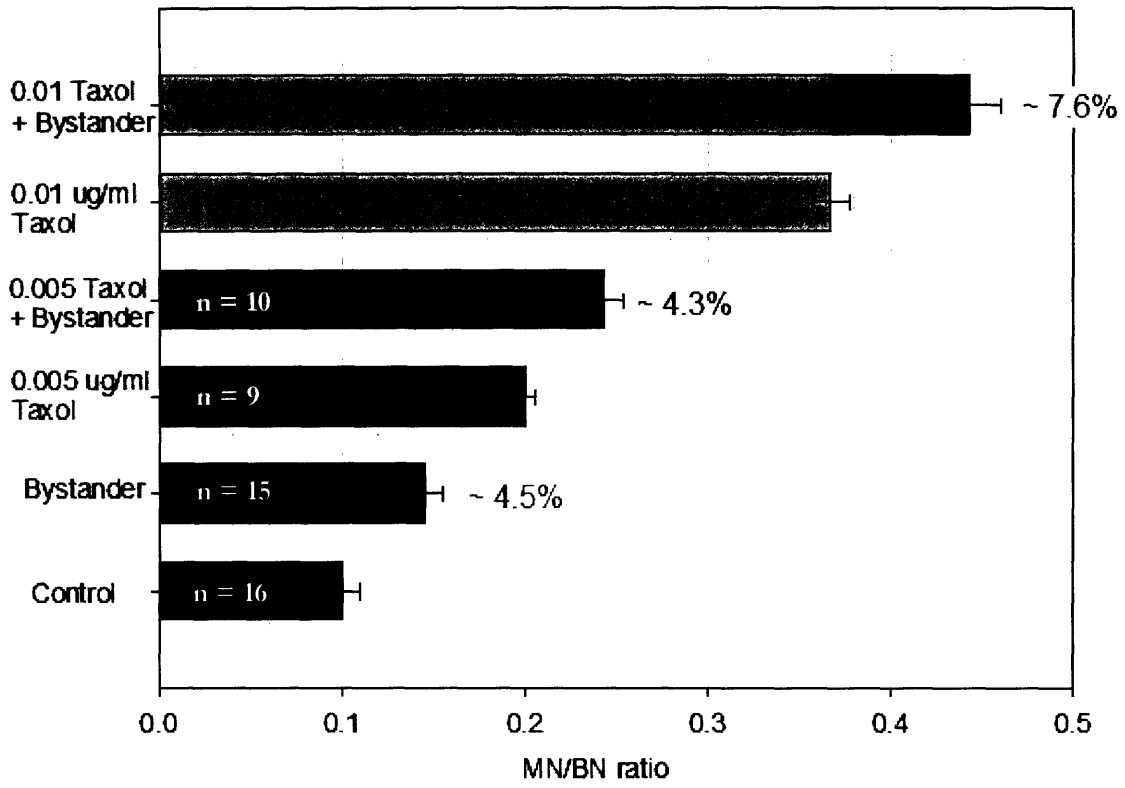

Figure 5-11. The horizontal histogram of MN/BN ratio for the combined effects of Taxol plus the bystander effect. Data are shown as means ± SD. The control produced 10.0 ± 1.0 % MN/BN; the bystander effect at 1.2 Gy direct dose produced 14.5 ± 1.0 % MN/BN; 0.005 μg/ml Taxol alone treatment for 24 hr produced 20.0 ± 0.6 % MN/BN; 0.005 μg/ml Taxol treatment plus the bystander effect produced 24.3 ± 1.1 % MN/BN; 0.01 μg/ml Taxol alone treatment for 24 hr produced 36.7 ± 1.0 % MN/BN; 0.01 μg/ml Taxol treatment plus the bystander effect produced 44.3 ± 1.7 % MN/BN. The right parts of the bars for the "Bystander" and "Taxol+Bystander" are the schematic increments from corresponding baselines (control or drug only). The numbers to the right of the bars represent the numerical values of the incremental means. The "n" within the bars indicates number of independent samples analyzed.

5.3.3.2 Cell cycle distribution

Figure 5-12 shows the cell cycle distribution results from the flow cytometer, for control, 0.005 μg/ml and 0.01 μg/ml Taxol treatments for 24 hr.

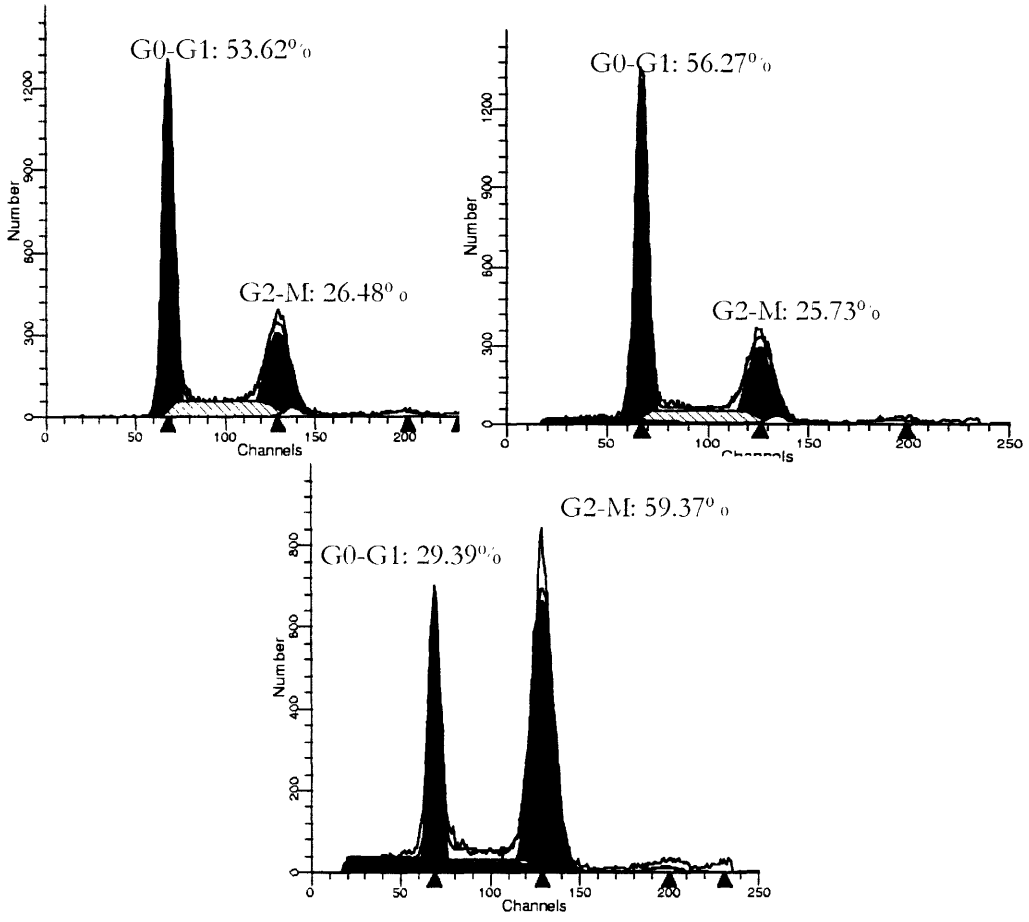

Figure 5-12. The cell cycle distributions of DU-145 cells for control (top left), 0.005 μg/ml Taxol treatment for 24 hr (top right) and 0.01 μg/ml Taxol treatment for 24 hr (bottom). The left peak is G0/G1 phase; the right peak is G2/M phase; the lower area with oblique lines between the two peaks is S phase; the solid lower area on the left and underneath the left peak is sub-G1 phase and indicates apoptosis. 0.005 μg/ml Taxol treatment for 24 hr did not change the cell cycle distribution significantly from the control, except that a small amount of apoptotic cells were present as the sub-G1 phase; 0.01 μg/ml Taxol treatment for 24 hr significantly shifted the cells from G0/G1 phase to G2/M phase and increased apoptosis in sub-G1 phase was observed.

5.3.3.3 Quantitative analysis

A simple quantitative analysis using an online statistical calculator provided by GraphPad Software, Inc., is given below under the assumptions that all variables follow a

Gaussian distribution and that the measurements of two groups are not paired or matched to each other. This analysis intends to provide quantitative data for the schematic increments in Figure 5-11 and compare them. A comprehensive analysis of the combined effects of the bystander effect and Taxol requires more experimental data and appropriate statistical tools and methods, which is part of the future work described in Chapter 6.

- The control group produced 10.0 ± 1.0 % MN/BN; the bystander group produced 14.5 ± 1.0 % MN/BN. The difference between the two groups is:

  $Mean_{(1-2)} = Mean_1 - Mean_2 = 14.5\% - 10.0\% = 4.5\%$

  $SD_{(1-2)} = \sqrt{(SD_1)^2 + (SD_2)^2} = \sqrt{(1.0\%)^2 + (1.0\%)^2} = 1.414\%$

  So the net increment is: **N1 = 4.5 ± 1.41 %**

- The 0.005 μg/ml Taxol group produced 20.0 ± 0.6 % MN/BN; the 0.005 μg/ml Taxol plus bystander group produced 24.3 ± 1.1 % MN/BN. The difference between the two groups is:

  $Mean_{(1-2)} = Mean_1 - Mean_2 = 24.3\% - 20.0\% = 4.3\%$

  $SD_{(1-2)} = \sqrt{(SD_1)^2 + (SD_2)^2} = \sqrt{(1.1\%)^2 + (0.6\%)^2} = 1.253\%$

  So the net increment is **N2 = 4.3 ± 1.25 %**

- The 0.01 μg/ml Taxol group produced 36.7 ± 1.0 % MN/BN; the 0.01 μg/ml Taxol plus bystander group produced 44.3 ± 1.7 % MN/BN. The difference between the two groups is:

  $Mean_{(1-2)} = Mean_1 - Mean_2 = 44.3\% - 36.7\% = 7.6\%$

  $SD_{(1-2)} = \sqrt{(SD_1)^2 + (SD_2)^2} = \sqrt{(1.7\%)^2 + (1.0\%)^2} = 1.972\%$

  So the net increment is **N3 = 7.6 ± 1.97 %**

By inputting the mean, the SD and the number of independent samples (n) of each N, the statistical differences between N1 and N2, N1 and N3 were obtained using an unpaired t-test (GraphPad Software, Inc.). Each N represents the difference between two groups of experiments with different n values (number of independent samples). So which "n" should be used as the input of unpaired t-test for comparison? In theory, the smaller "n" should give a stricter comparison, that is to say, n=15 for N1, n=9 for N2 and n=5 for N3. In the following analysis, an alternative n value is used just to see the difference in the results:

- **N2 (n=9) vs. N1 (n=15): The two-tailed P value equals 0.7301**
  By conventional criteria, this difference is not statistically significant.

- N2 (n=10) vs. N1 (n=16): The two-tailed P value equals 0.7176
  By conventional criteria, this difference is not statistically significant.

- **N3 (n=5) vs N1 (n=15): The two-tailed P value equals 0.0011**
  By conventional criteria, this difference is very statistically significant.

- N3 (n=6) vs N1 (n=15): The two-tailed P value equals 0.0007
  By conventional criteria, this difference is extremely statistically significant.

- N3 (n=7) vs N1 (n=15): The two-tailed P value equals 0.0004
  By conventional criteria, this difference is extremely statistically significant.

The quantitative analysis indicates that N2 is not statistically different from N1; N3 is significantly different from N1.

5.4 Discussion

In this Chapter, the effects of Taxol and oxaliplatin on the DU-145 cells were first studied. Then the combined effects of the two drugs with high-LET alpha-particle irradiation were studied. Finally the combined effects of Taxol with the bystander effect

described in chapter 4 were studied. Those experiments were intended as pilot studies to apply the established model system in new applications. The results were preliminary.

Taxol and oxaliplatin were reported to show radiosensitizing effects in several human cancer cell lines *in vitro* as well some cancers in clinical trials. They include human ovarian cancer cell lines (BG-1, SKOV-3, and OVCAR-3) (4, 5), a human grade 3 astrocytoma cell line, G18 (6), a human laryngeal squamous carcinoma cell line Hep-2 (7) and a human prostate carcinoma line (13) for Taxol; two head and neck cancer cells lines KB and Hep2 (24), a p53 wild type human colon cancer cell line (SW403) (25), rectal cancer (26, 27) and esophageal cancer (28) in clinical trials for oxaliplatin. The effects were dependent on both drug concentration and radiation dose. Although with different functional mechanisms, the radiosensitizer properties of both drugs are believed to be related to their abilities to arrest cells in the G2/M phase, which is believed to be the radiosensitive phase of cell cycle (3) (20). Our preliminary data (the survival curves) of the combined effects of the two drugs and the high-LET alpha-particle irradiation on the human prostate tumor cell line DU-145 qualitatively suggested additive to slightly antagonistic effects at various Taxol concentrations (0.005μg/ml, 0.01μg/ml and 0.05μg/ml) and oxaliplatin concentrations (0.5 μg/ml and 1.0 μg/ml) for 24 hr treatment (figure 5-5, 5-6, 5-7). The qualitative analysis was based on the shapes of the survival curves. The quantitative analysis using the isobologram at 50% SF and the combination index (CI) equation of Chou-Talalay indicated an additive effect between 0.005 μg/ml Taxol and the alpha-particle irradiation, and an antagonistic effect between 0.5 μg/ml oxaliplatin and the alpha-particle irradiation. Since looking for a synergistic situation was

the aim, when an additive or sub-additive effect was observed in a certain case, no more experiments were conducted.

In theory, the radiosensitizing effects of Taxol and oxaliplatin combined with low-LET radiation may not hold true for the high-LET alpha-particle irradiation. As discussed before, the synergism comes from the two drugs' abilities to arrest the cells in the G2/M phase (3) (20), which is believed to be the radiation sensitive phase of the cell cycle (32-34). This is generally true for low-LET radiations such as X-rays, where the radiosensitivity comes from inefficiency of DNA damage repair in the G2/M phase compared to G1 and S phases (more DNA content; less checkpoints before mitosis). Because DNA double strand breaks (DSBs) produced by high-LET radiations are more difficult to repair than single strand breaks (SSBs) produced by low-LET radiations, the radiosensitizer effects of the two drugs as a result of G2/M arrest may not work as well for high-LET alpha-particle irradiation.

The micronucleus induction results of the combined effects of Taxol and the bystander effect showed that the increment between "control" group and "bystander" group N1 is not statistically different from the increment between "0.005 μg/ml Taxol" group and "0.005 Taxol + bystander" group N2; N1 is statistically different from N3, the increment between "0.01 μg/ml Taxol" group and "0.01 Taxol + bystander" group. Flow cytometric analysis of the cell cycle indicated that 0.01 μg/ml Taxol treatment for 24 hr induced G2/M arrest and some apoptosis seen as cells with the sub-G1 DNA content, while 0.005 μg/ml Taxol treatment for 24 hr did not change the cell cycle distribution from the control. No conclusion is drawn on the combined effects of Taxol and the bystander effect at this point.

References:

1. Schiff, P. and Horwitz, S. Taxol stabilizes microtubules in mouse fibroblast cells. Proc Natl Acad Sci U S A, *77:* 1561-1565, 1980.
2. Zhang, A. and Russell, P. Paclitaxel suppresses the growth of primary prostate tumours (RM-1) and metastases in the lung in C57BL/6 mice. Cancer Lett, 2005.
3. Hennequin, C. Association of taxanes and radiotherapy: preclinical and clinical studies. Cancer Radiother, *8:* S95-105, 2004.
4. Steren, A., Sevin, B., Perras, J., Ramos, R., Angioli, R., Nguyen, H., Koechli, O., and Averette, H. Taxol as a radiation sensitizer: a flow cytometric study. Gynecol Oncol, *50:* 89-93, 1993.
5. Steren, A., Sevin, B., Perras, J., Angioli, R., Nguyen, H., Guerra, L., Koechli, O., and Averette, H. Taxol sensitizes human ovarian cancer cells to radiation. Gynecol Oncol, *48:* 252-258, 1993.
6. Tishler, R., Schiff, P., Geard, C., and Hall, E. Taxol: a novel radiation sensitizer. Int J Radiat Oncol Biol Phys, *22:* 613-617, 1992.
7. Liu, J. and Wang, J. Experimental study of taxol combining accelerated radiation on laryngeal carcinoma cells. Lin Chuang Er Bi Yan Hou Ke Za Zhi, *16:* 481-483, 2002.
8. Liebmann, J., Cook, J. A., Fisher, J., Teague, D., and Mitchell, J. B. In Vitro Studies of Taxol as a Radiation Sensitizer in Human Tumor Cells. J Natl Cancer Inst, *86:* 441-446, 1994.
9. Preisler, V., Wuck, D., and Stopper, H. Combination of paclitaxel and radiation: genotoxicity in vitro in four mammalian cell lines. Cancer Lett, *145:* 29-33, 1999.
10. Hennequin C, G. N., Favaudon V. Interaction of ionizing radiation with paclitaxel (Taxol) and docetaxel (Taxotere) in HeLa and SQ20B cells. Cancer Res., *56:* 1842-1850, 1996.
11. Leonard, C. E., Chan, D. C., Chou, T.-C., Rita Kumar, and Bunn, P. A. Paclitaxel Enhances in Vitro Radiosensitivity of Squamous Carcinoma Cell Lines of the Head and Neck. Cancer Research, *56:* 5198-5204, 1996.
12. Griffon-Etienne, G., Merlin, J., and Marchal, C. Association of docetaxel/paclitaxel with irradiation in ovarian carcinoma cell lines in bidimensional (sulforhodamine B assay) and tridimensional (spheroids) cultures. Anticancer Drugs, *7:* 660-670, 1996.
13. Lokeshwar, B., Ferrell, S., and Block, N. Enhancement of radiation response of prostatic carcinoma by taxol: therapeutic potential for late-stage malignancy. Anticancer Res, *15:* 93-98, 1995.
14. Espinosa, M., Martinez, M., Aguilar, J., Mota, A., De la Garza, J., Maldonado, V., and Melendez-Zajgla, J. Oxaliplatin activity in head and neck cancer cell lines. Cancer Chemother Pharmacol, *55:* 301-305, 2005.
15. Misset, J., Bleiberg, H., Sutherland, W., Bekradda, M., and Cvitkovic, E. Oxaliplatin clinical activity: a review. Crit Rev Oncol Hematol, *35:* 75-93, 2000.
16. Graham, M., Lockwood, G., Greenslade, D., Brienza, S., Bayssas, M., and Gamelin, E. Clinical pharmacokinetics of oxaliplatin: a critical review. Clin Cancer Res., *6:* 1205-1218, 2000.

17. Cvitkovic, E. A historical perspective on oxaliplatin: rethinking the role of platinum compounds and learning from near misses. Semin Oncol., *25:* 1-3, 1998.
18. Cvitkovic, E. Ongoing and unsaid on oxaliplatin: the hope. Br J Cancer, *Suppl 4:* 8-11, 1998.
19. Llory, J., Soulie, P., Cvitkovic, E., and Misset, J. Feasibility of high-dose platinum delivery with combined carboplatin and oxaliplatin. J Natl Cancer Inst., *86:* 1098-1099, 1994.
20. Raymond, E., Faivre, S., Chaney, S., Woynarowski, J., and Cvitkovic, E. Cellular and molecular pharmacology of oxaliplatin. Mol Cancer Ther., *1:* 227-235, 2002.
21. Riccardi, A., Ferlini, C., Meco, D., Mastrangelo, R., Scambia, G., and Riccardi, R. Antitumour activity of oxaliplatin in neuroblastoma cell lines. Eur J Cancer, *35:* 86-90, 1999.
22. Woynarowski, J., Faivre, S., Herzig, M., Arnett, B., Chapman, W., Trevino, A., Raymond, E., Chaney, S., Vaisman, A., Varchenko, M., and Juniewicz, P. Oxaliplatin-induced damage of cellular DNA. Mol Pharmacol, *58:* 920-927, 2000.
23. Scheeff, E., Briggs, J., and Howell, S. Molecular modeling of the intrastrand guanine-guanine DNA adducts produced by cisplatin and oxaliplatin. Mol Pharmacol, *56:* 633-643, 1999.
24. Espinosa, M., Martinez, M., Aguilar, J. L., Mota, A., Garza, J. G. D. l., Maldonado, V., and Meléndez-Zajgla, J. Oxaliplatin activity in head and neck cancer cell lines. Cancer Chemotherapy and Pharmacology, *55:* 301-305, 2004.
25. Magne, N., Fischel, J., Formento, P., Etienne, M., Dubreuil, A., Marcie, S., Lagrange, J., and Milano, G. Oxaliplatin-5-fluorouracil and ionizing radiation. Importance of the sequence and influence of p53 status. Oncology, *64:* 280-287, 2003.
26. Rodel, C., Grabenbauer, G., Papadopoulos, T., Hohenberger, W., Schmoll, H., and Sauer, R. Phase I/II trial of capecitabine, oxaliplatin, and radiation for rectal cancer. J Clin Oncol., *21:* 3098-3104, 2003.
27. Gerard, J., Chapet, O., Nemoz, C., Romestaing, P., Mornex, F., Coquard, R., Barbet, N., Atlan, D., Adeleine, P., and Freyer, G. Preoperative concurrent chemoradiotherapy in locally advanced rectal cancer with high-dose radiation and oxaliplatin-containing regimen: the Lyon R0-04 phase II trial. J Clin Oncol, *21:* 1119-1124, 2003.
28. Gergel, T., Leichman, L., Nava, H., Blumenson, L., Loewen, G., Gibbs, J., Khushalani, N., Leichman, C., Bodnar, L., Douglass, H., Smith, J., Kuettel, M., and Proulx, G. Effect of concurrent radiation therapy and chemotherapy on pulmonary function in patients with esophageal cancer: dose-volume histogram analysis. Cancer J., *8:* 451-460, 2002.
29. Chou, T. and Talalay, P. Quantitative analysis of dose-effect relationships: the combined effects of multiple drugs or enzyme inhibitors. Adv Enzyme Regul, *22:* 27-55, 1984.
30. Leonard, C., Chan, D., Chou, T., Kumar, R., and Bunn, P. Paclitaxel enhances in vitro radiosensitivity of squamous carcinoma cell lines of the head and neck. Cancer Res, *56:* 5198-5204, 1996.
31. Tallarida, R. Drug synergism: its detection and applications. J Pharmacol Exp Ther., *298:* 865-872, 2001.

32. Sinclair WK, M. R. X-ray sensitivity during the cell generation cycle of cultured Chinese hamster cells. Radiat Res, *29:* 450-474, 1966.
33. Sinclair, W. Cyclic x-ray responses in mammalian cells in vitro. Radiat Res., *33:* 620-643, 1968.
34. TERASIMA T, T. L. Variations in several responses of HeLa cells to x-irradiation during the division cycle. Biophys J., *3:* 11-33, 1963.

Chapter 6 Future Work

A bench-top alpha-particle irradiator was constructed and calibrated as described in Chapter 1. The small size and easy operation of the alpha-particle irradiator make it very convenient and flexible to use. The established alpha-particle irradiator can be used as a high-LET irradiation source in future work such as combinational studies between low-LET X-ray and high-LET alpha-particle irradiations, in which the irradiator could be placed inside the X-ray machine so that the cells in the Mylar dish are subject to both types of irradiations. There are five alpha foils with nominal activities ranging from 0.01 Ci/cm^2 to 100 Ci/cm^2. They can be used in applications ranging from low activity to high activity.

A bystander effect was observed in the co-culture system described in Chapter 4. The DMSO, PTIO and medium transfer studies suggested some properties of the bystander signal (involvement of a radical species other than nitric oxide; an effective life-time of less than 1 minute, etc.). More experiments are planed to investigate the mechanisms of the bystander effect. The experimental co-culture system can be improved by designing and making some insert-holders to fix the position of the insert inside the Mylar dish. By changing the distance between the two layers of cells, the effective migration distance of the bystander signal can be studied. In the described bystander studies, the bottom layer of cells was irradiated at room temperature. By placing the alpha-particle irradiator in a refrigerator or an incubator, the experiment can be carried out at different temperatures (4 °C or 37 °C) to study the chemical/biological properties and thermal stability of the bystander signal. If the effect is based on an enzyme activity, no effect will be observed at 4 °C.

Other than the micronucleus formation endpoint used in this study, other endpoints like cell clonogenic survivals, $p21^{Waf1}$ induction, apoptosis and γ-H_2AX foci formation can be used to study the co-cultured cells. Furthermore, DNA microarrays can be used to study the genetic information of the co-cultured cells. The bystander effect studied here is for the DU-145 human prostate tumor cell line with alpha-particle irradiation. It will be interesting to see whether the same cell line will produce and respond to a bystander effect with low-LET x-rays. In addition to DU-145, other mammalian cell lines, (tumor cell lines or normal tissue cell lines) can also be studied in the same experimental system for bystander effect detection.

The drug experiments in this project were intended as pilot studies. A complete combinational study between the alpha-particle irradiation and the anti-cancer drugs should include a range of radiation doses and drug concentrations in multiple independent experiments. Commercially available software CalcuSyn (Biosoft, Ferguson, MO) could be used to analyze the experimental data. The program provides a measure of whether the combined agents act in an additive, synergistic, or antagonistic manner.

The study of the combinational effects between the anti-cancer drugs and the bystander effect is a brand new topic in the field. The experimental data for the combinational studies between the bystander effect and 24 hr Taxol treatment described in Chapter 5 suggested an additive effect at a Taxol concentration of 0.005 μg/ml and a synergistic effect at a Taxol concentration of 0.01 μg/ml. Flow cytometry studies on cell cycle distribution indicated a G2/M arrest after 24 hr treatment with 0.01 μg/ml Taxol but no cell cycle change after 24 hr treatment with 0.005μg/ml Taxol. Those results suggested a correlation between the G2/M phase of the cell cycle and the sensitivity of the bystander

effect. Different Taxol concentrations and different Taxol treatment times other than 24 hr, together with cell cycle distribution, could be further studied to develop a clearer picture of interactions as well as the relationship between cell cycle and the bystander effect. The combinational study between the bystander effect and 24 hr oxaliplatin treatment did not produce an analyzable result. A different endpoint such as apoptosis can be used for the evaluation to avoid the involvement of cytochalasin-B.